Spatiotemporal lineage tracing reveals the dynamic spatial architecture of tumour growth and metastasis

Matthew G. Jones[1,24], Dawei Sun[2,3,24], Kyung Hoi (Joseph) Min[4,5,6], William N. Colgan[4,5], Haoyu Wang[7,8], Tivadar Török[2], Erik C. Cardoso[9,10], Luyi Tian[2,11], Jackson A. Weir[2,12], Victor Z. Chen[7,8], Luke W. Koblan[4,5], Kathryn E. Yost[4,5], Nicolas Mathey-Andrews[5,13,14], Edridge D'Souza[15,16], Andrew J.C. Russell[2,3], Robert R. Stickels[2], Karol S. Balderrama[2], William M. Rideout III[13], Min Dai[2], Giovanni Marrero[2], Vipin Kumar[2], Anjali Saqi[16,18], Benjamin Herzberg[15,16,18], Benjamin Izar[7,15-17], Howard Y. Chang[1,19-21], Joo-Hyeon Lee[9], Tyler Jacks[5,13], Fei Chen[2,3,#], Jonathan S. Weissman[4,5,13,22,#], Nir Yosef[23,#], Dian Yang[7,8,16,25,#]

[1] Center for Personal Dynamic Regulomes, Stanford University, Stanford, CA, USA.
[2] Broad Institute of MIT and Harvard, Cambridge, MA, USA
[3] Department of Stem Cell and Regenerative Biology, Harvard University, Cambridge, MA, USA
[4] Whitehead Institute for Biomedical Research, Cambridge, MA, USA
[5] Department of Biology, Massachusetts Institute of Technology, Cambridge, MA, USA
[6] Department of Electrical Engineering and Computer Science, Massachusetts Institute of Technology, Cambridge, MA, USA
[7] Department of Systems Biology, Columbia University, New York City, NY, USA
[8] Department of Molecular Pharmacology and Therapeutics, Columbia University, New York City, NY, USA
[9] Developmental Biology Program, Sloan Kettering Institute, Memorial Sloan Kettering Cancer Center, New York, NY 10065, USA
[10] Cambridge Stem Cell Institute, Jeffrey Cheah Biomedical Centre, University of Cambridge, Cambridge, CB2 0AW, UK
[11] Present address: Guangzhou National Laboratory, Guangzhou, China
[12] Biological and Biomedical Sciences Program, Harvard University, Cambridge, MA, USA
[13] David H. Koch Institute for Integrative Cancer Research, Massachusetts Institute of Technology, Cambridge, MA, USA
[14] Harvard Medical School, Boston, MA, USA
[15] Division of Hematology/Oncology, Department of Medicine, Columbia University Irving Medical Center, New York, NY, USA
[16] Vagelos College of Physicians and Surgeons, Herbert Irving Comprehensive Cancer Center, Columbia University, New York, NY, USA

[17] Columbia Center for Translational Immunology, Columbia University Irving Medical Center, New York, NY, USA
[18] Department of Pathology and Cell Biology, Columbia University Irving Medical Center, New York, NY, USA
[19] Department of Genetics, Stanford University, Stanford, CA, USA
[20] Howard Hughes Medical Institute, Stanford University School of Medicine, Stanford, CA, USA
[21] Present address: Amgen Research, South San Francisco, CA, 94080, USA
[22] Howard Hughes Medical Institute, Massachusetts Institute of Technology, Cambridge, MA, USA
[23] Department of Systems Immunology, Weizmann Institute of Science, 234 Herzl Street, Rehovot 7610001, Israel
[24] These authors contributed equally.
[25] Lead Contact
[#] Co-correspondence: : chenf@broadinstitute.org (F.C.), weissman@wi.mit.edu (J.S.W.), niryosef@berkeley.edu (N.Y.), dy2491@cumc.columbia.edu (D.Y.)

ABSTRACT

Tumour progression is driven by dynamic interactions between cancer cells and their surrounding microenvironment. Investigating the spatiotemporal evolution of tumours can provide crucial insights into how intrinsic changes within cancer cells and extrinsic alterations in the microenvironment cooperate to drive different stages of tumour progression. Here, we integrate high-resolution spatial transcriptomics and evolving lineage tracing technologies to elucidate how tumour expansion, plasticity, and metastasis co-evolve with microenvironmental remodelling in a *Kras;p53*-driven mouse model of lung adenocarcinoma. We find that rapid subclonal expansion contributes to a hypoxic, immunosuppressive, and fibrotic microenvironment that is associated with the emergence of pro-metastatic cancer cell states. Furthermore, metastases arise from spatially-confined subclones of primary tumours and remodel the distant metastatic niche into a fibrotic, collagen-rich microenvironment. Together, we present a comprehensive dataset integrating spatial assays and lineage tracing to elucidate how sequential changes in cancer cell state and microenvironmental structures cooperate to promote tumour progression.

MAIN

Tumour progression is driven by the dynamic interactions between cancer cells[1,2] and the their surrounding microenvironment[3,4]. In this process, as cancer cells accumulate genetic and epigenetic alterations, the microenvironment exerts selective pressures through factors such as spatial constraints[5,6], signalling molecules[7], nutrient and oxygen availability[8,9], and immune infiltration[3,10] among other phenomena. In turn, tumour growth remodels the surrounding microenvironment, for example, by restructuring the extracellular matrix and altering the composition and state of infiltrating stromal cells[11]. Systematically characterizing the cell intrinsic and extrinsic effects that drive tumour subclonal selection, cellular plasticity, and metastasis will not only provide insights into the principles of tumour evolution but also carry clinical implications. To accomplish this, one must study a tumour's evolutionary dynamics alongside its microenvironmental composition in the native spatial context.

Integrating tumour phylogenetic analysis, the study of lineage relationships of cancer cells within a tumour[12–17], with spatial information provides a comprehensive framework for understanding the interplay between tumour microenvironment and progression. Specifically, spatially resolved phylogenetic studies enable one to approach key questions in cancer evolution such as, what are the major spatial communities that exist in tumours, and how do these relate to tumour stage? From which spatial niches do subclonal expansions arise during tumour progression, and how does this relate to tumour plasticity and the capacity to seed metastases? And, how does the spatial growth pattern of tumour progression shape the surrounding microenvironment? Early studies reconstructing tumour phylogenies from multi-region sampling of patient tumours uncovered the spatial heterogeneity of genetic changes within tumours and have demonstrated the dynamics of tumour growth and spatially-constrained origins of metastatic dissemination[18–24]. More recently, spatial genomics approaches have further elucidated how the spatial distribution of genome alterations leads to clonal outgrowth, dispersion of subclones with distinct driver mutations, interactions with the immune system, and metastasis[25–29]. While these studies have greatly enhanced our understanding of how tumours grow in space and time, they can be limited in their ability to either resolve high-resolution spatial organisation, infer deeper phylogenetic relationships of cancer cells, or simultaneously measure the microenvironmental composition and gene expression.

The development of molecular recording technologies that install evolving lineage-tracing barcodes[30–40] and associated computational tools[41–46] enable the reconstruction of high-resolution phylogenies for studying tumour evolution[13]. Typically, these lineage-tracing technologies employ genome-editing tools, such as CRISPR/Cas9, to introduce heritable and irreversible mutations

102 progressively at defined genomic loci, which can be transcribed and thus profiled with single-cell
103 RNA-seq. In cancer, initial studies applied this technology to track the metastatic dynamics of
104 cancer cell lines transplanted into mice[47–49]. Previously, we described a lineage-tracing enabled
105 genetically-engineered mouse model of *Kras*$^{LSL\text{-}G12D/+}$*;Trp53*$^{fl/fl}$-driven lung adenocarcinoma (KP-
106 Tracer) to continuously track tumour evolution from nascent transformation of single cells to
107 aggressive metastasis[50]. In this system, intratracheal delivery of *Cre* recombinase using viral
108 vectors simultaneously induces Cas9-based lineage tracing and tumour initiation. This model
109 recapitulates the major steps of the evolution of human lung adenocarcinoma, both molecularly
110 and histopathologically[51–55]. Using this system, we recently identified subclonal expansions,
111 quantified tumour plasticity, traced metastatic origins and routes, and disentangled the effect of
112 genetic drivers on tumour evolution. However, as our previous applications have relied on
113 studying dissociated single cells, it has remained unclear how key tumour evolutionary properties
114 are associated with microenvironmental changes.

115 Here, we present an integrated lineage and spatial platform for tracking tumour evolution
116 *in situ* by applying high-resolution spatial transcriptomics to our lineage tracing-enabled KP-Tracer
117 model. Using two complementary spatial transcriptomics assays – Slide-seq[56,57] with spot-based
118 coverage at 10μm near-cell resolution of large tissue fields-of-view, and Slide-tags[58] with higher
119 molecular sensitivity and spatial profiling of individual nuclei – we produce a comprehensive
120 spatial transcriptomics dataset of *Kras;p53*-driven lung adenocarcinoma evolution. Integrating
121 these spatial transcriptomics data with inferred cancer cell lineages uncovered robust spatial
122 communities associated with tumour progression, including the formation of a hypoxic tumour
123 interior during rapid tumour subclonal expansion. Our analysis additionally reveals that this
124 hypoxic environment is associated with pervasive tissue remodelling characterised by fibrosis,
125 priming of immunosuppressive immune cells and rewiring of cellular interactions, and the
126 emergence of a pro-metastatic epithelial-to-mesenchymal transition (EMT). Together, this study
127 provides a scalable platform for studying the relationship between tissue architecture and tumour
128 progression, revealing key insights into the ecological and evolutionary dynamics underpinning
129 tumour evolution at unprecedented resolution.
130

131 **RESULTS**

132 **An integrated lineage and spatial platform for studying tumour evolution**

133 To study tumour evolution while preserving the native spatial context of cancerous and
134 stromal tissue, we integrated spatial transcriptomics methods with Cas9-based lineage-tracing
135 technology in our previously described KP-Tracer model of lung adenocarcinoma[50]. This model

136 is built upon the well-characterised model of *Kras;Trp53*-driven lung adenocarcinoma[51,52,54,55] and
137 is equipped with a *Cre*-inducible Cas9-based evolving lineage tracer that is able to continuously
138 record high-resolution cell lineages over months-long timescales[32,41]. Introduction of *Cre* into
139 individual lung cells in the adult animal both induces the oncogene mutations (i.e., expression of
140 $Kras^{G12D}$ and homozygous loss of *p53*) and initiates Cas9 expression. Cas9 then introduces
141 irreversible and heritable insertions and deletions ("indels") at defined genomic "target sites", each
142 discernable by a random 14bp integration barcode ("intBC") and expressed as a polyadenylated
143 transcript. As most sequencing-based spatial transcriptomics assays capture polyadenylated
144 transcripts from tissue sections[56–60], applying these assays to the KP-Tracer model yields
145 simultaneous measurement of spatially-resolved cell transcriptional states and lineage
146 relationships.

147 We initiated lung tumours and lineage-tracing in alveolar type II (AT2) cells (a major cell
148 of origin for lung adenocarcinoma) by intratracheally delivering adenovirus expressing *Cre*
149 recombinase under the control of an AT2 cell-specific, surfactant Protein C (SPC) gene
150 promoter[61]. Twelve to sixteen weeks post tumour initiation, tumour bearing lungs were harvested
151 for cryopreservation, and then sectioned and applied to spatial transcriptomics arrays (**Fig. 1a;**
152 **Methods**). To comprehensively profile the spatiotemporal evolution of tumour progression, we
153 utilised two complementary spatial transcriptomics technologies: Slide-seq[56,57] that captures
154 transcriptomic states of "spots" at near-cellular 10μm resolution in continuous, large fields-of-view
155 (up to 1cm x 1cm); and Slide-tags[58] that sparsely samples individual nuclei for transcriptomic
156 profiling and provides accurate spatial localisation for a subset of these nuclei (typically ~50-70%).
157 Together, this combination marries the scale of Slide-seq and true single-nucleus resolution of
158 Slide-tags to jointly measure spatially resolved cell lineage and unbiased transcriptomic states in
159 the native tumour microenvironment.

160 With these two technologies, we comprehensively profiled tumour-bearing lungs across
161 various stages of progression with 44 Slide-seq arrays and 5 Slide-tags arrays (**Extended Data**
162 **Fig. 1a-c**; **Methods**; **Supplementary Table 1**). The resulting datasets provided spatial profiling
163 of distinct domains in tumour-bearing tissues characterised by the expression of canonical marker
164 genes and corroborated by paired H&E: for example, in the tumour-bearing lung we found that
165 *Cxcl15* and *Scgb1a1* marked epithelial-like domains, representing alveolar and club cells,
166 respectively. Moreover, histologically aggressive regions were marked by *Vim* (characteristic of
167 mesenchymal-like cancer cells) and *Arg1* (characteristic of immunosuppressive myeloid cells[62])
168 **(Fig. 1b**). Altogether, these datasets provide high-resolution views into the microenvironmental
169 context and organisation of tumours.

Computational tools enable the inference of spatially resolved cancer cell phylogenies

As the KP-Tracer system expresses lineage tracing target-sites as poly-adenylated transcripts, we next turned to evaluating the recovery of these target sites from the complementary spatial transcriptomics platforms. Reassuringly, we detected target-site transcripts robustly across tens-of-thousands of spots or nuclei in these spatial datasets, with Slide-tags data having more consistent detection of target-sites as expected (**Fig. 1c; Extended Data Fig. 1d-e**).

While Slide-tags provided true single-cell measurements and thus were amenable to previously-described lineage reconstruction approaches[41,44], there were two predominant analytical challenges in reconstructing tumour phylogenies of tens-of-thousands of spots observed in Slide-seq data. First, Slide-seq captures RNA molecules with near-cellular resolution, meaning that each spot may contain RNAs originating from multiple cells[57]; similarly, cells with distinct lineage states can be captured in a single spot, which we term “conflicting states”. As prior phylogenetic reconstruction algorithms for Cas9-lineage tracing data presume mapping of cells to single states, we first implemented new Cassiopeia-Greedy[41] and Neighbour-Joining[63] variants that could use many conflicting states during reconstruction (**Methods**). We also tested the effects of three strategies for preprocessing conflicting states via simulation: (1) a strategy that used all conflicting states observed in a spot along with the abundance of each state in that spot (“all states”); (2) all conflicting states observed in a spot, but without considering their abundance (“collapse duplicates”); or (3) a strategy that used only the most abundant state (“most abundant”). We found that the second strategy (“collapse duplicates”) performed most robustly (**Extended Data Fig. 2a**; **Methods**).

A second challenge is that Slide-seq assays (and to a lesser extent Slide-tags) have an increased missing data rate relative to droplet-based single-cell assays[64]. As expected, we observed overall lower target-site transcript capture (and thus higher missing data) in Slide-seq datasets (**Extended Data Fig. 1d** and **Extended Data Fig. 2b**). We hypothesised that spatial relationships could be used to overcome this sparsity, which was supported by our observations that indel states were coherent within small spatial neighbourhoods (**Extended Data Fig. 2c-d**). We therefore developed an inferential approach that predicted missing lineage-tracing states from spatial neighbours (within 30μm of a target node) with sufficient recovery (at least 3 UMI supporting a target site intBC-indel combination; **Fig. 1d**). We first tested the feasibility of this approach using simulations of lineage tracing data on spatial arrays using Cassiopeia (**Methods)**. We found that missing lineage-tracing barcodes could consistently be recovered at high accuracy (**Extended Data Fig. 2e**), and that spatial imputation followed by tree inference by a hybrid

algorithm consisting of the Cassiopeia-Greedy and Neighbour-Joining algorithms resulted in the best reconstructions, especially in high-dropout regimes (**Extended Data Fig. 2f-g**; **Methods**). Next, we tested our ability to recover held-out target site data from real Slide-seq data and similarly found that missing data could be robustly recovered by spatial predictions, resulting in a median accuracy of 90% on imputing held-out data across all experiments, matching our simulation results (random predictions had a median accuracy of 67% and yielded 29% fewer imputations; **Extended Data Fig. 2h**). As expected, more frequent alleles had higher imputation accuracy (**Extended Data Fig. 2i**; **Methods**). Over multiple iterations of this imputation algorithm, we found that we could recover up to 58% of missing data (4-58%, on average 31% across datasets), resulting in comparable missing data rates to previous reports using single-cell approaches that have enabled robust tree reconstruction and biological insights (**Fig. 1d, Extended Data Fig. 2j**). Though we only retain high-confidence imputations, and our benchmarks point to the promise of this spatial imputation in this context, there are notable caveats especially in the case of cell migration (see **Discussion**). Combining Slide-seq data and validation from orthogonal trees provided by Slide-tags establish a foundation for studying the spatial lineages of cancer cells.

Together, these computational improvements enabled us to build lineages of cancer cells in the native context of a tumour's microenvironment at unprecedented resolution (**Fig. 1e**). Our lineages revealed phylogenetic relationships in structured spatial environments and enabled us to explore the spatial localisation of increasingly related subclones within the same tumour (**Fig. 1e**, **Extended Data Fig. 2k)**. Furthermore, in comparing trees built from Slide-tags data, we observed copy-number variation (CNVs) largely corroborated lineages (as previously shown[50]), though there were far fewer CNVs per cell than lineage states generated by the lineage tracer (**Extended Data Fig. 3**). With these data and approaches, we turned to investigating the relationship between changes to the microenvironmental architecture and tumour progression.

Spatial transcriptomics reveal the ecosystems of lung adenocarcinoma

While recent efforts have studied the composition of tumours in this model using single-cell approaches[50,54,55], it has remained challenging to profile the spatial organisation of these cell types. To address this, we leveraged the complementary insights gained from the high sensitivity, true single-nucleus measurements of Slide-tags and the broad field-of-view of Slide-seq to perform a systematic analysis of tumour spatial organisation across stages of progression observed in our 49 spatial transcriptomics arrays representing more than 100 tumours.

237 Focusing first on the true single nuclei profiled with Slide-tags, we performed fine-grained
238 annotation of clusters consisting of normal epithelial, stromal, immune, and tumour cells
239 (determined by canonical marker genes and the presence of active lineage-tracing edits) (**Fig.**
240 **2a-b**; **Extended Data Fig. 4a**; **Methods**). In addition to annotating previously described tumour
241 and normal epithelial cells in this model[50,55], we identified a previously undescribed tumour cell
242 state characterised by the expression of neuronal genes such *Piezo2* and *Robo1,* the endothelial
243 marker *Pecam1,* maintenance of the lung-lineage transcription factor *Nkx2-1*, and absence of *Vim*
244 (**Extended Data Fig. 4b-c**). Although this cell type expressed active lineage tracing marks in our
245 system, it is likely that this cell type was excluded in previous studies[50,55,65] by purifying cancer
246 cells against CD31 expression (also known as *Pecam1*, expressed in this population) prior to
247 transcriptomic profiling; this highlights the advantage of spatial transcriptomics in profiling all cells
248 and communities, eliminating potential biases arising from tissue dissociation and preparation. In
249 the immune and stromal compartment, we observed large macrophage, fibroblast, and
250 endothelial populations with lower representation of B cells and dendritic cells (**Fig. 2a**; **Extended**
251 **Data Fig. 4a**). Among macrophages, we detected *SiglecF*+ tissue-resident alveolar macrophages
252 and three distinct tumour-associated macrophage (TAM) populations: *Vegfa*+ TAMs,
253 immunosuppressive *Arg1*+ TAMs, and proangiogenic *Pecam1*+ TAMs (**Fig. 2a)**. We additionally
254 detected a diverse set of cancer-associated fibroblasts (CAFs): a mesothelial-like *Wt1*+
255 population, an inflammatory-like CAF ("iCAF") population expressing the complement gene *C7*
256 and *Abca8a*, and a myofibroblast-like CAF ("myCAF") population expressing *Postn* (**Fig. 2a,**
257 **Extended Data Fig. 4a**).

258 To explore the spatial localisation of these diverse cell states, we assigned spatial
259 locations to Slide-tags nuclei and spatially projected cell identities (**Methods**). Consistent with
260 previous characterisations of Slide-tags spatial mapping rates[14], we found that approximately 50%
261 of nuclei could be confidently assigned to a spatial location (**Extended Data Fig. 4d**). Across the
262 five Slide-tags arrays, we observed a distinct pattern where less aggressive, "early-stage" tumour
263 cell states (i.e., AT2- and AT1-like cancer cells, indicated by expression of active lineage marks
264 and distinct gene expression from normal AT2 and AT1 cells) co-localized on the periphery of
265 tumour sections consisting of more aggressive "late stage" tumour cells (**Fig. 2c, Extended Data**
266 **Fig. 4e**). Similar to previous work in this model[66], we also found that distinct immune and stromal
267 cell types exhibited differential infiltration – for example, Alveolar Macrophages and iCAFs were
268 typically found outside tumours, whereas *Arg1*+ TAMs and myCAFs were more likely to be found
269 within tumours (**Fig. 2c, Extended Data Fig. 4e)**.

The spatially-localised transcriptional signatures observed with Slide-tags motivated us to pair this approach with Slide-seq assays to survey the spatial gene expression communities across large tissue areas in tumours. We thus turned to the 44 tissue sections assayed with Slide-seq that collectively represent more than 100 tumours at various tumour stages. To identify modules of genes that were recurrently spatially co-expressed across multiple samples, we employed the Hotspot[33] algorithm (**Methods**). Our analysis revealed 11 recurrent spatial gene modules, hereafter referred to as "communities" (**Fig. 2d-e; Supplementary Table 2**), that we annotated by inspecting the genes contained within communities and evaluating the expression level of community genes (captured in a "community score") in cell types identified by Slide-tags data (**Extended Data Fig. 4f; Extended Data Fig. 5a)**.

The genes contained within these transcriptional communities represent a variety of co-localised gene expression states: for example, an early-stage alveolar-like community contained genes marking epithelial cells such as *Sftpc* and *Cxcl15* ("C1: Alveolar"), a hypoxic community contained canonical marker genes of hypoxia such as *Slc2a1* (also known as *Glut1*) ("C10: Hypoxia"), and an epithelial-to-mesenchymal (EMT) community contained genes such as *Vim*, up-regulation of *Myc* signalling, and metastasis-related genes such as *Hmga2* ("C3: EMT"; **Fig. 2d-e, Extended Data Fig. 5a**). In addition to fibroblast (C5), B cell (C6), and endothelial (C7) communities, we identified two distinct immunoregulatory-related communities. The first community contained genes associated with scavenger-like macrophages like *Marco* and *Mrc1* ("C8: Scavenger Mac"); a second community contained genes characteristic of inflammation such as *B2m*, *Stat1*, and *Ifit1* ("C9: Inflammatory"). As these communities describe genes co-expressed in spatial proximity, they provide insights into possible intercellular interactions. For example, the EMT and hypoxic communities (C3 and C10) contained genes associated with macrophage recruitment (e.g. *Csf1)* and polarisation to immunosuppressive states that have been previously reported to promote aggressive cancer phenotypes (e.g., *Arg1*[62] and *Spp1*[67]*)*, while the Inflammatory community (C9) contained *Cxcl9* that has been previously reported in anti-tumour macrophage polarisation[67] (**Extended Data Fig. 5a**).

To inspect the distribution of these communities across large tissue sections profiled with Slide-seq, we quantified community scores for each spot and assigned spots to the community with the highest score (**Fig. 2e-f, Extended Data Fig. 5b-c**). In comparing histology from an adjacent layer to the community scores, we found co-localisation between areas indicating high tumour grade (as indicated by histology) and high scores for EMT, hypoxic, and fibrotic communities (C3, C10, C5; **Extended Data Fig. 5b**). We next asked how the distribution of community assignments varied over tumour stages using a gene set signature we previously

identified to robustly associate with tumour progression (termed a "fitness signature")[50] (**Fig. 2f; Extended Data Fig. 5c**; **Methods**). Specifically, this fitness signature contains genes that are associated with subclonal expansions in this model, and their collective activity (i.e., "score") reflects tumour progression towards an aggressive, pro-metastatic state. Consistent with the definition of this signature, after ranking tumours by their fitness signature score and inspecting the proportion of community assignments, we observed that early-stage tumours were dominated by epithelial, endothelial, and inflammatory communities (C1, C7, and C8, respectively) but that late-stage tumours had larger fractions of EMT, hypoxic, and fibroblast communities (C3, C10, and C5, respectively; **Fig. 2f, Extended Data Fig. 5c**). Moreover, we found that overall abundances of EMT, hypoxic, and fibroblast community assignments (C3, C10, and C5, respectively) were correlated across all tumours; conversely, they were anticorrelated with the abundances of alveolar and inflammatory communities (C1 and C8, respectively) (**Fig. 2g**).

Together, these analyses unite the unique advantages of Slide-tags and Slide-seq assays to provide a consensus set of spatial communities that highlight differential immune and stromal activation and localization patterns across tumour progression in KP tumours. These observations motivated us to next integrate our phylogenies to understand how the spatiotemporal dynamics of these communities are associated with tumour plasticity and subclonal expansion.

Rapid tumour subclonal expansion contributes to a hypoxic niche with decreased cancer cell plasticity

Integrating cell state information with high-resolution phylogenies can offer new insights into various aspects of tumour evolution. In our previous work, we introduced frameworks to quantify the historical record of subclonal growth rates ("phylogenetic fitness") and the number of cell-state transitions in each cell's lineage ("single-cell clonal plasticity") directly from phylogenies[50,68]. We described a model whereby KP-Tracer tumour progression is driven by the loss of an initial AT2-like cell state and accompanying increases in single-cell clonal plasticity and transcriptional heterogeneity; in turn, these high-plasticity cells provide a diverse pool of transcriptional states from which high-fitness, low-plasticity subclones with increased metastatic ability and expression for EMT markers like *Vim* and *Hmga2* are selected[50]. Consistent with this previous work, the tumours studied with this spatial-lineage platform showed an overall distribution where transient increases in plasticity are followed by the selection of low-plasticity, high fitness subclones (**Extended Data Fig. 6a**). Since these measures of fitness and clonal plasticity are computed from phylogenies (and not cell-intrinsic features), we reasoned that we could extend our previously reported model by relating these phylodynamic changes to the

surrounding microenvironment, thereby identifying cancer cell extrinsic factors associated with tumour fitness and plasticity.

As the measurement of phylogenetic fitness reports on the history of subclonal growth, spatially-resolved phylogenies are well suited to understanding the relationship between tumour growth patterns and microenvironmental properties[22,69]. In one representative Slide-seq example (S-seq 40), we found an expanding subclone with high phylogenetic fitness localised to a tumour interior characterised by late-stage Hypoxic and EMT communities (C10 & C3) while the tumour periphery had lower phylogenetic fitness and was marked by the Alveolar community (C1) (**Fig. 3a**). This co-localisation of high phylogenetic fitness with hypoxic regions was supported by four lines of evidence: first, we found that phylogenetic fitness was correlated with the orthogonal, previously-described fitness signature[50] (Pearson's $r = 0.4$; **Extended Data Fig. 6b**). Second, the emergence of a large CNV-defined subclone (containing an amplification of the *Kras* locus on chromosome 6) co-localized with the hypoxic regions (**Extended Data Fig. 6c**). Third, in a systematic analysis of all Slide-seq tumours, we found that the EMT and Hypoxic communities were most strongly correlated with phylogenetic fitness (**Extended Data Fig. 6d**). Finally, across all high-resolution Slide-tags arrays, we similarly found that the late-stage states (e.g., EMT) were most likely to be found in regions that had previously undergone subclonal expansion (**Extended Data Fig. 6e**). These orthogonal data collectively support the observation that the co-localisation of expansion and hypoxia is consistent across tumours and is not an artifact of tree reconstruction or the near-cell resolution of Slide-seq.

The localisation of expanding subclones characterised by aggressive gene expression states in a representative Slide-seq example (S-seq 40) prompted us to hypothesise that rapid subclonal expansions may create a layered architecture whereby expanding subclones dominate a central region surrounded by non-expanding cells (**Fig. 3a-b**). Focusing first on this representative Slide-seq example, we observed that multiple low-fitness areas of Tumour 1 could be grouped together in a phylogenetic subclade despite being geographically distant (though many indels were shared across the tree, these low-fitness, distant cells were marked by the shared absence of indels marking the expanding region) (**Fig. 3a-b**; **Extended Data Fig. 6f**). Though this pattern could be generated many ways (e.g., independent migration of several subclones), the most parsimonious interpretation suggests that these scattered low-fitness cells were in close spatial proximity during the early stage of tumour growth but were later pushed to the tumour periphery because of a subclonal expansion event. To investigate the consistency of this phenomenon, we next quantified the phylogenetic fitness of individual cancer cells derived from high-resolution Slide-tags arrays on multiple tumours and inspected the spatial distribution

372 of subclonal expansion. In this analysis, we also found that the tumour interior in Slide-tags data
373 was more likely to contain cells with more aggressive gene expression states (e.g., Endoderm-
374 like and EMT states) and higher phylogenetic fitness as inferred from reconstructed trees (**Fig.**
375 **3c-d** $p < 1e\text{-}5$, wilcoxon rank-sums test**; Fig. 2c**; **Extended Data Fig. 4e**).
376 Recent work in this model has underscored the importance of epigenetic remodelling
377 during tumour progression, often manifesting as rapid cell-type transitions that can be quantified
378 using a phylogeny-based single-cell clonal plasticity measure[50,54]. Motivated by the observed
379 interplay between expansion and microenvironmental remodelling, we next turned to investigating
380 the association between spatial features and changes in single-cell clonal plasticity. Starting in
381 the representative Slide-seq example (S-seq 40), we observed that low-plasticity clones in
382 Tumour 1 co-localised with high-fitness regions in the tumour interior whereas the high-plasticity
383 regions of Tumour 2 (which lacked a subclonal expansion) appeared to lack spatial organisation
384 (**Fig. 3a**). Consistent with this, we found that the high-fitness Hypoxic and EMT communities, and
385 related states, were associated with lower plasticity across all Slide-seq and Slide-tags datasets
386 (**Extended Data Fig. 6g-h**). To better understand how transient increases in plasticity associated
387 with the subclonal expansions observed across Slide-seq datasets (**Extended Data Fig. 6a**), we
388 further examined the transition to subclonal expansion in arrays profiled with Slide-tags
389 (**Extended Data Fig. 6i-k**). Across our Slide-tags data, we found there was little spatial
390 organisation of high-plasticity cells in tumours without detectable subclonal expansion (as
391 measured by Moran's *I* autocorrelation statistic[70]), whereas low-plasticity cells were spatially
392 localized to the tumour centre in tumours after expansion (**Extended Data Fig. 6j-k**; **Methods**).
393 Collectively, these data support a model whereby the tumour microenvironment is
394 sequentially remodelled by subclonal expansion, culminating in an interior hypoxic region and
395 eventually the emergence of a late-stage, pro-metastatic EMT state. Moreover, our analysis of
396 clonal transcriptional plasticity refines our previous model of tumour progression: after loss of the
397 initial AT2-like identity and an increase in clonal plasticity, rapid subclonal expansion drives spatial
398 reorganization of the tumour and leads to the formation of a hypoxic region, which may in turn
399 induce and stabilize the EMT of cancer cells. As evidenced by examples of tumours across
400 various stages, this model is characterised by the exclusion of early-stage communities (e.g., C1:
401 Alveolar) to the tumour periphery while subclonal expansions contribute to the acquisition of a
402 low-plasticity, high-fitness Hypoxic community (C10) and eventual transition to an EMT
403 community (C3) (**Fig. 3e; Fig. 2f**; **Extended Data Fig. 6i**).
404

405 **Subclonal expansion is accompanied by immunosuppressive and fibrotic**
406 **microenvironmental remodelling**

407 As our Slide-seq data suggest that the microenvironment is remodelled during subclonal
408 expansion, we next leveraged Slide-tags data to dissect the expansion-associated cell state
409 transitions at single-nucleus resolution. After quantifying phylogenetic fitness on trees inferred
410 from Slide-tags data, we stratified nuclei into high- and low-fitness groups and inspected the cell
411 type abundances in their spatial neighbourhoods (**Fig. 3f**; **Extended Data Fig. 7a**; **Methods**). As
412 expected, we found that the EMT cancer cell state was most consistently enriched in
413 neighbourhoods surrounding high-fitness nuclei (**Fig. 3f**). With respect to differential enrichment
414 of specific immune and stromal populations, we found that *Arg1*+ TAM and myCAF populations
415 were consistently enriched in spatial neighbourhoods of high-fitness cells whereas iCAFs and
416 other TAMs were not (**Fig. 3f**).

417 Prompted by differential enrichment of TAM and CAF populations, we turned to
418 systematically probing the cell state changes associated with subclonal expansions. Focusing on
419 TAM and CAF populations, we performed differential expression of these cell types based on their
420 spatial proximity to expanding cancer cells (**Extended Data Fig. 7b-c**). In addition to high *Arg1*
421 expression, we found that TAMs in expanding tumour regions were characterized by the presence
422 of the hypoxia-induced factor *Egnl3*, the immunosuppressive marker *Spp1*[67], and programs
423 indicating endocytosis and complement activity (**Extended Data Fig. 7b**; **Supplementary Table**
424 **3**). CAFs in expanding neighbourhoods were characterised by increased expression of genes
425 implicated in hypoxia sensing, collagen synthesis, and fibrosis (**Extended Data Fig. 7c**;
426 **Supplementary Table 3**). Likewise, in a more comprehensive analysis of the 44 Slide-seq arrays,
427 we found that spatial neighbourhoods surrounding high-fitness, low-plasticity spots were most
428 enriched for EMT, Hypoxic, and Fibrotic communities (C3, C10, and C5, respectively) and
429 depleted for Alveolar, Endothelial, and Inflammatory communities (C1, C7, and C9, respectively)
430 (**Extended Data Fig. 7d-e**; **Methods**).

431 These data suggest a model by which subclonal expansions towards a hypoxic tumour
432 interior that, in turn, polarises non-tumour cells into pro-tumour, immunosuppressive states.
433 Indeed, in returning to our previous Slide-seq analysis of community program assignments across
434 tumour progression, we observed that the Hypoxic community (C10) appears prior to EMT (C3)
435 when ranked by the transcriptional fitness signature (**Fig. 2f; Extended Data Fig. 5c**). In further
436 support of this, immunofluorescence staining of KP-Tracer tumours revealed that hypoxia (as
437 evidenced by the canonical hypoxia marker GLUT1 [*Slc2a1]* protein levels[71,72]) preceded the
438 emergence of immunosuppressive ARG1+ immune cells (**Fig. 3g**). Importantly, we also found

439 these same patterns in large surgical resections of human lung adenocarcinoma (**Methods**).
440 Using immunofluorescence, we found significant co-localisation of hypoxia signalling and
441 immunosuppressive SPP1+ protein levels ($p < 1e\text{-}5$, Fisher's Exact Test); we also find that SPP1
442 and macrophage-marker CD68 overlap suggests that the majority of SPP1+ cells are
443 macrophages (**Extended Data Fig. 7f; Methods**). These hypoxic, immunosuppressive tumour
444 regions were also enriched with increased VIM expression, a marker of cancer cell EMT ($p < 1e\text{-}$
445 5, Fisher's Exact Test; **Extended Data Fig. 7g; Methods**). Consistent with these data, a
446 reanalysis of published spatial transcriptomics data of human NSCLC tumours[40] revealed that
447 expression of the hypoxia-reporter *SLC2A1* (also known as *GLUT1*) was spatially associated with
448 cell proliferation (as measured by *MKI67*), *TGF β* signalling, EMT (*SNAI2*), and
449 immunosuppressive macrophage polarisation (*SPP1, C1QB,* and *FCGR2B)* (**Extended Data Fig.**
450 **7h-i**).
451

452 **Differential intercellular interactions and hypoxia in the expanding niche drive cancer cell**
453 **state changes**

454 Our analyses thus far have revealed that expansion is characterized by a hypoxic,
455 immunosuppressive niche that is accompanied by marked changes in cell type abundance and
456 gene expression states. To gain additional molecular insight into these changes, we first
457 investigated how cell-cell interactions differed between the expanding and non-expanding tumour
458 niches. Applying a computational approach that identifies spatially localized cell-cell interactions
459 to all our Slide-tags data, we found substantial reprogramming of interactions in expanding niches
460 (**Fig. 3h; Extended Data Fig. 8**; **Supplementary Table 4; Methods**). This systematic analysis
461 provided insight into the multitude of intercellular signalling pathways that integrate to establish
462 and maintain the expanding niche: for example, from cancer cells, we find signals to macrophages
463 that promote their recruitment (e.g., *Mif::Cd74*, *Mif::Cd44,* and *Il34::Csf1r*) and polarization to
464 immunosuppressive states (e.g., *Bmp7*::*Acvr1*, *Mertk::Pros1*, and *Angptl2::Pirb*); in addition we
465 find cancer cell-derived signals to fibroblasts that promote extracellular matrix remodelling and
466 fibrosis (e.g., *Sdc1::Tnc, Fgf1::Fgfr1, Pdgfa::Pdgfrb*, and *Spp1::Itga8*). Reciprocally, cancer cells
467 receive signals from this remodelled environment that promote the transition to proliferative and
468 invasive phenotypes: in addition to pervasive TGFβ signaling[73] (a well-known inducer of EMT),
469 cancer cells also received cell-type-specific signals from TAMs (e.g., *Fn1::Cd44*, *Il18::Il18r1,* and
470 *Jag2::Notch2*) and CAFs (including several collagen and laminin genes signalling through *Cd44*
471 and integrins on cancer cells). As orthogonal evidence of these interactions, we find that several
472 are co-contained within the communities identified from the 44 Slide-seq arrays (e.g., *Fn1*, *Cd44*,

473 *Spp1*, *Itga5* and *Bmp7* are all found in the EMT module, C3; **Supplementary Table 2**; **Extended**
474 **Data Fig. 5a**). Together, this integrated spatial-lineage analysis provides a comprehensive
475 catalogue of the multitudinous, and complementary, intercellular signals that synergize to
476 establish a remodelled microenvironmental niche that promotes and stabilizes aggressive cancer
477 cell states.

478 These differential intercellular signals in the hypoxic expanding niche led us to ask how
479 various extrinsic signals drive cancer cell state changes and tumour progression. Because
480 hypoxia has been shown to induce cell-state changes (including to EMT[74–76]), we tested the
481 relative contributions of intercellular interactions with lung resident cells and hypoxia on major
482 cancer cell states reported in this model[50,54,55] (including AT2-like, gastric-like, high-plasticity, and
483 EMT states). To model the complexity of the tumour microenvironment, we utilized a procedure
484 to derive primary organoids from fresh KP tumours[77] and co-cultured them in normal and hypoxic
485 conditions with primary lung mesenchymal cells and alveolar macrophages isolated from wild type
486 mice (**Fig. 3i**). In cancer cells, hypoxia alone induced a mild decrease in alveolar cell markers
487 (*Sftpc* and *Cebpa*) and gastric-like markers (*Gkn2* and *Hnf4a*), a slight increase of the early
488 mesenchymal marker (*Vim*), and no change in the key EMT transcription factor *Twist1*; on the
489 other hand, co-culture of cancer cells with alveolar macrophages and lung mesenchymal cells
490 under normal oxygen condition enhanced the epithelial identity of cancer cells (marked by
491 upregulation of *Epcam* and lineage markers *Sftpc* and *Cebpa*) and the high-plasticity cell state
492 marker *Slc4a11*[55]. Remarkably, when co-culturing cancer organoids, lung mesenchymal cells, and
493 alveolar macrophages under hypoxia we observed a robust induction of EMT in cancer cells, with
494 more than 2.5-fold increase of classical EMT markers (*Vim* and *Twist1*) compared to what is
495 expected from hypoxia alone (**Fig. 3j; Supplementary Table 5**). Together, these data provide
496 critical insights into the synergistic role between hypoxia and differential intercellular interactions
497 in driving cancer cell state changes, highlighting that cancer cells must receive both external
498 stimuli to enter and maintain an aggressive EMT-like state.
499

500 **Spatially resolved lineages reveal the evolution of metastasis-initiating niches in the**
501 **primary tumour**

502 Metastasis, the ultimate stage of tumour progression, accounts for approximately 90% of
503 cancer-related mortality and is associated with pervasive microenvironmental remodelling[78–82].
504 However, it has remained challenging to delineate the specific microenvironmental features
505 associated with tumour evolutionary dynamics during metastasis progression. Outstanding
506 questions include: do the niches surrounding subclones giving rise to metastases differ from those

surrounding other subclones? How do these gene expression programs change during metastatic spread? Our spatial-lineage platform is well-suited to identify the spatial localisation of metastasis-initiating subclones and characterize the microenvironmental remodelling associated with each step of the metastatic cascade.

We began by performing spatial transcriptomics on a KP-Tracer mouse with multiple primary lung tumours and widespread metastases in the mediastinal lymph node, rib cage, and diaphragm (**Fig. 4a, Extended Data Fig. 9a**). To maximise the probability of detecting metastasis-initiating subclones in primary tumours, we sampled multiple representative layers of the tumour-bearing lung at approximately 200-500um intervals, enabling us to study multiple large primary tumours from top-to-bottom and better track the clonal dynamics beyond a two-dimensional analysis. Tumour segmentation of Slide-seq data from these sections and coarse-grained spatial alignment determined by shared lineage states revealed four major tumours that could be tracked across layers (**Fig. 4b**).

Our spatial-lineages in the large Slide-seq assays provide an opportunity to both compare the trajectory of multiple tumours and understand the transcriptional evolution of the niche surrounding the metastasis-initiating subclone in a single primary tumour. To do so, we first identified the spatial localisation of subclones giving rise to metastasis by inspecting the allelic similarities between primary tumours and metastases (**Fig. 4c; Extended Data Fig. 9b-c**). This analysis revealed that metastases from all 3 locations were phylogenetically related to a spatially coherent subclone in primary Tumour 2 (“T2”). Though distinct indels support this relationship between T2 and its related metastases (**Extended Data Fig. 9d**), the sparsity of spatial data and low lineage resolution within the expansion precluded an accurate estimation of the number of metastatic seeding events; however, because all metastases shared a common indel state, and metastasis is rare in this model[50,65], a parsimonious explanation is that metastasis was initiated via a monoclonal seeding from T2 and subsequent secondary seeding events to different metastatic sites. Nevertheless, T2 could be identified in each layer independently and could be thus tracked across all sampled layers of this primary tumour (**Extended Data Fig. 9b-c**). This pattern was consistent in matched Slide-tags data (**Extended Data Figure 9c**), overlapped with subclonal expansions identified from our phylogenies, and was associated with regions exhibiting poorly differentiated histological features (**Fig. 4c-e; Extended Data Fig. 9e-f**). Leveraging the three-dimensional (3D) sampling of this tissue, and because all metastases shared indels with an expanding subclone that could be found across layers, we infer that it is likely that all metastases arose after subclonal expansion.

540 To understand the phylogenetic and gene expression programs underlying metastatic
541 potential in this region of T2, we segmented this tumour into a niche surrounding the cells giving
542 rise to metastases ("T2-Met") or otherwise ("T2-NonMet") and compared their gene expression
543 patterns (**Fig. 4c-e**; **Methods**). The T2-Met niche had higher proportions of the EMT and Hypoxic
544 communities (C3 & C10, respectively) and lower proportions of the Gastric/Endoderm and
545 Alveolar communities (C11 & C1, respectively) (**Fig. 4f**). The T2-Met niche additionally down-
546 regulated genes associated with Gastric and Endoderm states (e.g., *Gkn2* and *Meg3*), and had
547 higher expression of genes marking cancer cell EMT (e.g., *Vim*), scavenger macrophages (e.g.,
548 *Mrc1* and *Msr1*), immunosuppressive macrophages (e.g., *Arg1* and *Fcgr2b*), TGFβ signalling
549 (e.g., *Tgfb1* and *Smad4*), and fibrosis (e.g., *Cthrc1* and *Postn*) (**Fig. 4g**). Orthogonal analysis with
550 Slide-tags data corroborated these findings, as *Arg1*+ TAMs and myCAFs were most enriched in
551 spatial neighbourhoods of cells in the primary tumour related to metastases (**Extended Data Fig.
552 9g**). Moreover, immunofluorescence staining confirmed that ARG1+ cells co-localized with the
553 metastasis-initiating VIM+ region of the T2 primary tumour (**Extended Data Fig. 9h**). Together,
554 these results nominate several key molecular processes as potential drivers of the pro-metastatic
555 niche, including fibrosis, TGFβ signalling, and intercellular interactions between cancer cells,
556 activated fibroblasts, and *Arg1*+ immunosuppressive macrophages.
557

558 **Metastatic colonisation is accompanied by sustained EMT and enhanced fibrosis**

559 Beyond the evolution within the primary tumours, we next investigated whether the
560 microenvironments at distant metastatic sites are remodelled to resemble, or diverge from, the
561 metastasis-initiating niche within the primary tumour. Comparing the niches surrounding
562 metastases and the T2-Met subclone in the primary tumour, we found that metastases contained
563 proportionally more regions annotated by stromal or immune communities and showed
564 specifically higher representation of the Fibrotic community (C5) (**Fig. 4f**). As these communities
565 represent several gene programs and may mask fine-scaled cell type changes, we further
566 characterised the differential gene expression changes distinguishing niches of the primary
567 tumour and metastases (**Fig. 4g**). While metastases up-regulated genes also found to distinguish
568 the T2-Met niche – such as the EMT markers *Vim* and *Hmga2* and TGFβ-related genes –
569 metastases displayed up-regulation of genes associated with collagen deposition (e.g., *Col1a1*
570 and *Col12a1*) and myogenesis (*Tnnt3* and *Ncam1*) (**Fig. 4g**). After quantifying the activity of these
571 gene expression programs in Slide-seq spots, we confirmed that these aggregated gene
572 expression signals were spatially localised to tumour regions: metastatic tumours generally
573 resembled the metastasis-initiating subclone in the primary tumour (for example with respect to

574 TGFβ signalling: log2FC = -0.14, t-test p=1.0; **Fig. 4h**) but substantially up-regulated collagen-
575 related genes as compared to the primary tumour (log2FC = 3.81, t-test $p<1e-5$) (**Fig. 4i**). In a
576 re-analysis of previously published datasets of metastatic KP tumours[50,65], we also found that if
577 EMT and TGFβ signaling was present in the metastasis-initiating primary tumour, these programs
578 were maintained (or enhanced) during metastasis across a range of distal sites (**Extended Data**
579 **Fig. 10a**). Immunofluorescence staining further corroborated a marked increase in COL3A1
580 protein in metastases as compared to primary tumours **(Extended Data Fig. 10b**). Using our
581 Slide-seq data, we found that TGFβ signalling was significantly higher in metastases compared
582 to surrounding normal tissue; however, collagen deposition was increased in half of our samples,
583 indicating that metastases may co-opt the structure of the distal site to promote colonization
584 (**Extended Data Fig. 10c**).
585 Extending our results beyond our mouse model, we additionally analysed single-cell RNA-
586 seq data from a cohort of 56 human lung adenocarcinoma patients[83] (including 34 brain
587 metastases; **Extended Data Fig. 10d**). Our analysis revealed that distant metastases maintained
588 high activity of the key gene expression programs we observed in our mouse data, including
589 collagen deposition, TGF β signalling, hypoxia sensing, immunosuppressive myeloid cell
590 recruitment, and EMT (**Extended Data Fig. 10e-h**). Collectively, these results complement recent
591 findings that TGFβ signalling is critical for EMT and metastatic seeding[79], and highlight that key
592 properties of the metastasis-initiating tumour (e.g, EMT and fibrosis) are consistently preserved
593 in remodelling of the distant site.
594
595 **DISCUSSION**
596 In this study, we integrated high-resolution spatial transcriptomics with Cas9-based
597 lineage tracing in a genetically engineered mouse model of lung adenocarcinoma to dissect the
598 dynamic interplay between tumour evolution and microenvironmental remodelling in a spatially
599 resolved fashion. Our analysis uncovered spatial communities associated with different stages of
600 tumour progression; revealed relationships between tumour growth, plasticity and
601 microenvironmental remodelling; and identified metastasis-initiating subclones that informed on
602 the spatiotemporal evolution of gene expression along the metastatic cascade. These results
603 present an unprecedented spatial map of lung adenocarcinoma evolution and the temporal
604 ordering of key tumour evolutionary events, showcasing the power of integrating spatially resolved
605 transcriptomics and single-cell lineage tracing to dissect the complex tumour dynamics underlying
606 cancer progression.

607 This spatial-lineage platform provides new insights into our understanding of lung
608 adenocarcinoma evolution in the KP model by revealing how key processes – such as subclonal
609 expansion, hypoxia, and EMT – emerge and interrelate over time and space in the native
610 microenvironment (**Fig. 4j)**. Our previous results provided several lines of evidence that tumours,
611 following the initial loss of an AT2-like state, are characterised by a cancer-cell-intrinsic increase
612 in clonal plasticity, leading to gains in transcriptional heterogeneity and subsequent subclonal
613 expansion[50]. In the present study, we find that rapid subclonal expansion pushes early-stage
614 cancer cells to the tumour periphery and contributes to the formation of a hypoxic
615 microenvironmental niche. This hypoxic niche promotes additional microenvironmental
616 remodelling characterised by *Arg1+* immunosuppressive myeloid subsets and myCAF-like
617 fibroblasts; for example, by recruiting myeloid cells through hypoxia-induced chemokine secretion
618 (e.g., *Ccl2, Ccl6,* and *Csf1*) and polarising immune and stromal cells through hypoxia-induced
619 signalling cascades (e.g., *Hif1a* and *Vegfa*) as previously suggested[84–88] (**Extended Data Fig. 4a;**
620 **Extended Data Fig. 5a; Extended Data Fig. 7b-c; Supplementary Table 2-3**). In turn, our
621 organoid experiments suggest that these reprogrammed immunosuppressive and pro-fibrotic
622 cells integrate with hypoxia to drive cancer cell state transitions, leading to the emergence of a
623 stable and pro-metastatic EMT state, for example through *TGFβ* signalling as shown in our
624 analysis (**Fig. 3h-j; Fig. 4g-h; Extended Data Fig. 9h**) and detailed in a recent study[79]. Upon
625 dissemination, metastatic cells retain a mesenchymal phenotype (e.g., through sustained TGFβ
626 signalling) and can further remodel the microenvironment into an enhanced fibrotic niche marked
627 by increased collagen deposition (**Extended Data Fig. 10**).

628 Our proposed model of tumour progression in the KP lung cancer model has key
629 implications into the temporal ordering of how cancer-intrinsic alterations and external signals
630 integrate to regulate cancer cell states. Specifically, in the first stage of tumour progression,
631 cancer cells enter a permissive epigenetic state characterized by increased plasticity and
632 transcriptional heterogeneity but maintain their epithelial identity[50,54,55]. Our analysis of cell-cell
633 interactions and 3D organoid co-culture experiments suggest that this epigenetic state is
634 stabilized by normal, tissue-resident cells in the microenvironment (**Fig. 3h-k**; **Extended Data**
635 **Fig. 8**). As high-plasticity regions of these tumours do not appear to be spatially coherent (**Fig.**
636 **3a**; **Extended Data Fig. 6i-k**), we propose that this first stage of tumour progression is mostly
637 driven by cell-intrinsic epigenetic changes accompanying the loss of the AT2-like state.

638 In contrast, we find that after subclonal expansion, the tumour is substantially remodelled
639 towards a hypoxic state characterized by immunosuppressive and fibrotic communities. Hypoxia
640 has been shown to play critical roles in lung adenocarcinoma[89] and other cancers (e.g., glioma[90]

641 and clear cell renal cell carcinoma[22]) where it is associated with genomic instability and EMT[22,74–
642 [76,91]. However, our understanding of how and when hypoxic conditions arise, and how hypoxia
643 coordinates both further tumour microenvironmental remodelling and cancer cell state changes,
644 have remained limited. Our model provides new insights into these questions, as we provide
645 several lines of evidence that subclonal expansion actively contributes to the formation of a
646 hypoxic niche within the tumour, which in turn drives the polarisation of immunosuppressive and
647 fibrotic cell types that trigger distinct cancer cell state changes and induce the EMT state (**Fig. 2f**;
648 **Extended Data Fig. 5c**; **Fig. 3e-j**). To note, our proposed model that multiple external stimuli
649 (here, hypoxia and differential intercellular interactions from the remodelled tumour
650 microenvironment) cooperate with cell-intrinsic changes in plasticity aligns well with data from
651 other models, such as pancreatic adenocarcinoma[92]. Moreover, consistent with work
652 demonstrating that EMT and metastasis are initiated in the perinecrotic tumour core[93], we find
653 that metastatic initiation occurs from spatially-confined subclones that have undergone EMT
654 around the hypoxic niche (**Fig. 3a**; **Fig 4c-f**). With supporting evidence from our analysis of lung
655 adenocarcinoma patient cohorts (**Extended Data Fig. 7f-h**; **Extended Data Fig. 10d-h**), we
656 believe our model provides fundamental insights into the drivers and consequences of hypoxia,
657 and more generally how feedback between intrinsic and extrinsic forces shape cancer cell states.
658 In addition to elucidating new aspects of how tumour evolution unfolds spatially, our study
659 also sets the foundation for further studies. First, mechanistic studies will be needed to dissect
660 how the hypoxic niche polarises immune and stromal subsets, and how this might lead to an
661 aggressive, mesenchymal tumour state. As we have previously reported that plasticity plays an
662 important role in tumour progression[28,50,55,94], one area of research will be how hypoxia affects the
663 high-plasticity cell states in lung cancer. Second, the platform we developed here can be adapted
664 to study the spatiotemporal dynamics of tumour evolution in other models or under different
665 perturbations. Notably, our platform is also amenable to modelling the effect of additional genetic
666 perturbations as Cas9 is continuously expressed for tracing[50]. Third, while we introduced new
667 computational approaches for phylogenetic reconstruction approaches that address the sparsity,
668 resolution, and scale of these data, there remain opportunities to build new algorithms specifically
669 tailored to the spatial aspect of data and statistically infer how spatial organisation affects
670 phylogenetic patterns.
671 While our study reveals new aspects of tumour progression, there are limitations in the
672 interpretation and extensibility of the approaches applied here. First, a single slide section may
673 not represent the entirety of clonal dynamics in a tumour. To minimize this potential bias, we
674 corroborated phylogenetic patterns with histology, orthogonal gene expression signatures derived

675 from our previous single-cell lineage-tracing data (derived from unbiased sampling of whole
676 tumours) and analysing representative sections at different depths of tumours from a tumour-
677 bearing lung in **Fig. 4**. As scaling spatial transcriptomics experiments becomes more affordable,
678 future studies can more densely sample three-dimensional structure to entirely account for this
679 bias. Second, as a consequence of profiling tumour sections and the sparsity of spatial
680 transcriptomics assays, we observe less indel diversity in spatial lineage tracing data than in
681 previous applications with unbiased sampling, leading to lower resolution phylogenetic
682 relationships. This may be ameliorated by optimizing the lineage-tracing kinetics and adapting
683 tools for recording past molecular signalling events[95,96]. Third, the molecular sparsity and
684 resolution of Slide-seq data pose a challenge in reconstructing phylogenies and detecting smaller
685 spatial neighbourhoods (**Extended Data Fig. 2**). While we provide a spatial imputation algorithm
686 to account for these technical issues, and benchmark its effectiveness in a variety of experiments
687 from simulated and held-out real data, we anticipate that this imputation approach may have
688 limitations in cases where lineage data is not spatially coherent, for example in systems with
689 higher degrees of cell migration. In these scenarios, either alternative technologies with improved
690 capture and resolution or new algorithms for performing spatial imputation and detecting robust
691 spatial communities will be necessary. Finally, the trees presented in this study are only estimates
692 of true phylogenetic relationships and may not truly reflect cell division histories; moreover, our
693 quantifications of phylodynamic properties – expansion and plasticity – may be masked by non-
694 uniform death rates and unobserved intermediate states. When possible, our study uses
695 orthogonal data and approaches to substantiate all claims.

696 In summary, our study unites the insights provided by spatially resolved lineages and
697 transcriptomics to investigate the fundamental patterns of tumour growth and its interactions with
698 the microenvironment. Our analyses lead to a comprehensive model of how a tumour grows from
699 a single, transformed cell into a large and complex ecosystem and provided new evidence for
700 how tumour expansion-associated microenvironmental remodelling contributes to a distinct wave
701 of cell state reprogramming towards pro-metastatic states. As one of the most comprehensive
702 datasets of spatial tumour evolution to date, we anticipate that this resource will help pioneer new
703 computational methods and quantitative and predictive models of tumour evolution.
704

705 **ACKNOWLEDGEMENTS**

706 We thank Jack Rose, Can Ergen, Chen Weng, Pu Zheng, Sean-Luc Shanahan, Yun
707 Zhang, Meaghan McGery, Santiago Naranjo, Theodore Esantsi, Raymond Ho, Michelle Chan,
708 Romain Lopez, Adam Gayoso, and all members of the Weissman, Yang, Yosef, Chen, and Chang

709 labs for helpful discussions. We thank Cristen Muresan, Anne Odera, Maria Gould, Daniel
710 Braslavsky, Maxim Litvinov, and Nicole Dow for administrative support. We thank the Whitehead
711 Institute and Broad Institute Sequencing Facility for sequencing support.
712 M.G.J. is supported by an NCI Pathway to Independence Award (NIH K99CA286968).
713 N.M.A. was supported by a NIH F30 fellowship (1F30CA278495). K.E.Y. was supported by the
714 National Cancer Institute of the National Institutes of Health under Award Number K00CA253729.
715 L.W.K. is supported by a Helen Hay Whitney Postdoctoral Fellowship. T.J. laboratory currently
716 also receives funding from The Lustgarten Foundation for Pancreatic Cancer Research, but this
717 funding did not support the research described in this manuscript. This work was supported in
718 part by the Cancer Center Support (core) grant P30-CA14051 from the National Cancer Institute
719 and by the NIH grant R35CA274464. T.J. is the David H. Koch Professor of Biology and a Daniel
720 K. Ludwig Scholar. J.S.W. is supported by the Howard Hughes Medical Institute, NCI Cancer
721 Target Discovery and Development (CTD^2) and NIH Centers of Excellence in Genomic Science
722 (CEGS). Both J.S.W. and T.J. received fundings from Ludwig Center at MIT. D.Y. is supported
723 by a Damon Runyon Dale Frey Award, an NCI Transition Career Development Award
724 1K22CA289207, an NIH Director's New Innovator Award 1DP2OD037078, and a Lung Cancer
725 Research Foundation Leading Edge Award. N.Y. is supported in part by an NIH grant R56-
726 HG013117 and by the European Union Council (ERC, Tx-phylogeography, 101089213). Views
727 and opinions expressed are however those of the authors only and do not necessarily
728 reflect those of the European Union or the European Research Council Executive Agency.
729 Neither the European Union nor the granting authority can be held responsible for them. F.C.
730 acknowledges support from NIH Early Independence Award (DP5, 1DP5OD024583), the NHGRI
731 (R01, R01HG010647), the Burroughs Wellcome Fund CASI award, the Searle Scholars
732 Foundation, the Harvard Stem Cell Institute, and the Merkin Institute. This research was
733 supported by the NYSCF. FC is a New York Stem Cell Foundation – Robertson Investigator. B.I.
734 was supported by the National Institutes of Health (NIH) through National Cancer Institute (NCI)
735 grants R01CA266446, R01CA280414, R37CA258829, and U54CA274506; B.I. was additionally
736 supported by a Velocity Fellows Award, the Louis V. Gerstner, Jr. Scholars Program, a Tara Miller
737 Team Science Award Metastasis Research by the Melanoma Research Alliance, the Pershing
738 Square Sohn Cancer Research Alliance Award, and the Herbert Irving Comprehensive Cancer
739 Center (HICCC) Human Tissue Immunology and Immunotherapy Initiative. B.I. is a Cancer
740 Research Institute Lloyd J. Old STAR (CRI5579). E.D. was supported by an NIH F30 award
741 (1F30CA301910-01).
742

AUTHOR CONTRIBUTIONS

D.Y., J.S.W., N.Y., F.C. and K.H.(J.)M. conceived of the project. D.Y., L.T, and D.S. transduced mice, sacrificed mice, harvested tumours, and constructed spatial transcriptomics sequencing libraries. W.M.R III generated the KP-Tracer chimeric mice. M.G.J. analysed the lineage-tracing and gene expression spatial transcriptomics data with help from K.H.(J.)M., W.N.C, and V.Z.C. M.G.J. and K.H.(J.) M. performed simulation benchmarks for Slide-seq data with input from W.N.C., L.W.K., and K.E.Y. J.W. performed spatial-mapping of Slide-tags data. D.S. and N.M.A. performed staining and imaging of H&E and immunofluorescence and histology analysis. T.T and M.D. developed the ligand-receptor detection algorithm and T.T. performed ligand-receptor analysis with help from M.G.J. and D.S. H.W., and E.C performed organoid coculture experiments and gene expression analysis with supervision from D.Y. and J.L. E.D. and B.I. provided access to PBMA data and performed analysis on LUAD brain metastases. B.H, and A.S. collected and identified human LUAD surgical resections. G.M. and V.K. aided with synthesizing pucks for spatial transcriptomics experiments. D.Y., M.G.J., D.S., T.J., J.S.W., N.Y., and F.C. interpreted the results. M.G.J., D.Y., and D.S. wrote the manuscript with input from all authors.

DECLARATION OF INTERESTS

M.G.J. consults for and has equity in Tahoe Therapeutics. K.E.Y. is a consultant for Cartography Biosciences and Curie Bio. T.J. is a member of the Board of Directors of Amgen and Thermo Fisher Scientific, and a co-Founder of Dragonfly Therapeutics and T2 Biosystems. T.J. serves on the Scientific Advisory Board of Dragonfly Therapeutics, SQZ Biotech, and Skyhawk Therapeutics. T.J. is the President of Break Through Cancer. None of these affiliations represent a conflict of interest with respect to the design or execution of this study or interpretation of data presented in this manuscript. J.S.W. declares outside interest in 5 AM Venture, Amgen, Chroma Medicine, KSQ Therapeutics, Maze Therapeutics, Tenaya Therapeutics, Tessera Therapeutics, Ziada Therapeutics, DEM Biopharma, and Third Rock Ventures. D.Y. declares outside interest in DEM Biopharma. B.I. has received consulting fees/honoraria from Volastra Therapeutics Inc, Merck, AstraZeneca, Novartis, Eisai, and Janssen Pharmaceuticals and has received research funding to Columbia University from Alkermes, Arcus Biosciences, Checkmate Pharmaceuticals, Compugen, Immunocore, Merck, Regeneron, and Synthekine. B.I. is the scientific founder of Basima Therapeutics, Inc.

DATA AND CODE AVAILABILITY

776 Custom code and tutorials for the analysis of spatially-resolved lineage-tracing data is available
777 on Github through Cassiopeia (https://github.com/YosefLab/Cassiopeia). Notebooks and code for
778 reproducing analyses are available at https://github.com/mattjones315/KPSpatial-release. All raw
779 and processed data will be made available on GEO and other public repositories.
780

781 **SUPPLEMENTARY TABLES**

782 **Supplementary Table 1**: Meta data for samples
783 **Supplementary Table 2**: Genes in spatial communities.
784 **Supplementary Table 3**: Fitness-neighbourhood differential expression and GO Term analyses.
785 **Supplementary Table 4**: LARIS ranked cell-cell communication list.
786 **Supplementary Table 5**: Quantitative PCR measurements for organoid experiments.
787

788 **METHODS**

789 **EXPERIMENTAL MODELS AND SUBJECT DETAILS**

790 **KP-Tracer mice**

791 KP-Tracer mouse was generated by generating chimeric mice from blastocyst injection of
792 engineered, lineage tracer enabled mouse embryonic stem cells harbouring conditional alleles
793 *Kras*$^{LSL\text{-}G12D/+}$;*Trp53*$^{fl/fl}$; *Rosa26*$^{LSL\text{-}Cas9\text{-}P2A\text{-}mNeonGreen}$ as previously described[50]. Eight-to-twelve-
794 week-old KP-Tracer mice were infected intratracheally with ad5-SPC-Cre virus (1x10^8 Pfu)
795 purchased from University of Iowa viral vector core for tumour initiation. This enables specific
796 tumour initiation and lineage-tracing in Alveolar Type II (AT2) cells, the major cell-type of origin of
797 lung adenocarcinoma. All studies were performed under an animal protocol approved by the
798 Massachusetts Institute of Technology (MIT) and Columbia University Committee on Animal Care.
799 Mice were assessed for morbidity according to MIT and Columbia Division of Comparative
800 Medicine guidelines and humanely sacrificed prior to natural expiration.

801 **Surgical resection of human lung adenocarcinoma**

802 Formalin fixed paraffine embedded tissue specimens of human lung adenocarcinoma surgical
803 resections were acquired from the Columbia University Molecular Pathology Core Facility. These
804 samples were initially collected under Institutional Review Board (IRB)-approved protocol
805 AAAA3987 at New York Presbyterian Hospital/Columbia University Medical Center (CUMC), and
806 all processing procedures performed on patient samples were in accordance with the ethical
807 standards of the IRB. Twelve surgical resections of KRAS-mutant lung adenocarcinoma were
808 used for immunostaining analysis.

809 **METHODS DETAILS**

810 **Sample processing**

811 Tumour-bearing lungs were harvested and re-inflated with ~2ml of 50% OCT (1:1 mix with
812 PBS) and 1:100 of RNase inhibitor (NEB M0314L). After cleaning up excess blood and liquid, the
813 whole tissue was embedded in 100% OCT and frozen using dry ice-methanol bath. Frozen
814 samples were kept at -80C until sectioning for further analysis.

815 **Spatial transcriptomics with Slide-seqV2**

816 ***For 3 mm and 5.5 mm arrays*.** Fresh frozen tissues were cryo-sectioned at a thickness
817 of 10 μm using a Cryostat (CM1950, Leica) set at −17 to −18 °C. The tissue sections were
818 carefully transferred onto precooled arrays, which were placed on top of a glass slide inside the
819 cryostat. A finger was briefly placed underneath the slide to melt the tissue and adhere it to the
820 array. Immediately after, the tissue and array were transferred together into a 1.5 ml or 2 ml
821 Eppendorf tube containing 200 μl (for 3 mm arrays) or 500 μl (for 5.5 mm arrays) of hybridisation
822 buffer (6x SSC with 2 U μl^{-1} Lucigen NxGen RNase inhibitor, Lucigen, 30281). The samples were
823 incubated in the hybridisation buffer for 15 minutes to 1 hour at room temperature, allowing the
824 RNA to bind to the oligonucleotides on the beads. After incubation, the tissue and array were
825 briefly dipped into 1x Maxima RT buffer to wash off the hybridisation buffer and then transferred
826 to the reverse transcription (RT) reaction mixture (1x Maxima RT buffer, 1 mM dNTPs (NEB,
827 N0477L), 2 U μl^{-1} Lucigen NxGen RNase inhibitor, 2.5 μM template switch oligonucleotide, 10
828 U/μL Maxima H Minus reverse transcriptase (Thermofisher Scientific, EP0753)). The tissue and
829 array were incubated in 200 μl (for 3 mm arrays) and 500 μl (for 5.5 mm arrays) of the RT reaction
830 mixture for 30 minutes at room temperature, followed by 1.5 hours at 52 °C. To digest the tissue,
831 200 μl (for 3 mm arrays) or 500 μl (for 5.5 mm arrays) of tissue digestion buffer (100 mM Tris-Cl
832 pH 7.5, 200 mM NaCl, 2% (w/v) SDS, 5 mM EDTA and 16 U ml^{-1} proteinase K (NEB, P8107S))
833 was added to the reaction mixture and incubated at 37 °C for 30 minutes. Following digestion,
834 200 μl (for 3 mm arrays) or 500 μl (for 5.5 mm arrays) of wash buffer (10 mM Tris pH 8.0, 1 mM
835 EDTA and 0.01% Tween-20) was added, and a P200 pipette was used to carefully triturate the
836 beads off the array. The beads were centrifuged at 3000g for 2 minutes, followed by three washes
837 with wash buffer. To remove RNA strands, the beads were incubated in 0.1N NaOH for 5 minutes,
838 followed by a wash with wash buffer and 1x TE buffer, and centrifuged again at 3000g for 2
839 minutes. Second-strand synthesis was performed by mixing the beads with 200 μl (for 3 mm
840 arrays) or 500 μl (for 5.5 mm arrays) of second-strand synthesis mixture (1x Maxima RT buffer,
841 1 mM dNTPs, 10 μM dN-SMRT oligonucleotide and 125U ml^{-1} Klenow enzyme (NEB, M0210L))
842 and incubating at 37 °C for 1 hour. The beads were then washed three times with wash buffer

843 and once with water. cDNA amplification was carried out by resuspending the beads in 200 µl (for
844 3mm arrays) or 1.2 ml (for 5.5 mm arrays) of cDNA amplification mixture (1x Terra Direct PCR
845 mix buffer (Takara Biosciences, 639270), 25U ml^{-1} of Terra polymerase (Takara Biosciences,
846 639270), 2 µM TruSeq PCR handle primer and 2 µM SMART PCR primer). The reaction was
847 divided into 50 µl aliquots and amplified using the following PCR program: 95 °C for 3 min; four
848 cycles of 98 °C for 20 s, 65 °C for 45 s and 72 °C for 3 min; nine cycles of 98 °C for 20 s, 67 °C for
849 20 s and 72 °C for 3 min; 72 °C for 5 min; hold at 4 °C. The cDNA product was purified twice using
850 SPRI beads (Beckman Coulter, B23318) at a 0.8x bead-to-sample ratio, eluting in a final volume
851 of 20 µl (for 3mm arrays) and 60 µl (for 5.5 mm arrays). A total of 1 ng (for 3 mm arrays) or 3x 1ng
852 (for 5.5 mm arrays) of cDNA was used for Illumina sequencing library construction. The Nextera
853 XT kit (Illumina, FC-131-1096) was used for tagmentation, followed by amplification with TruSeq5
854 and N700 series barcoded index primers. Libraries were cleaned with SPRI beads according to
855 the manufacturer's instructions at a 0.6x bead-to-sample ratio and resuspended in 10 µl of water
856 per reaction. Lineage tracing target site libraries were amplified from cDNA and prepared fpr
857 Illumina sequencing using previously described protocols[50].

858 ***For Curio 1 cm arrays*.** The buffers and enzymes used were the same as those described
859 for the 3 mm and 5.5 mm arrays but adjusted for scale. In brief, hybridisation, dipping, washing,
860 RT reaction and tissue digestion were performed using the reservoirs provided by Curio with 500
861 µl volume for each step. After tissue digestion the beads were divided into 2 tubes for wash buffer
862 washes and combined for cDNA amplification. A total of 4.8 ml of cDNA amplification mixture was
863 prepared, and the reaction was divided into 50 µl aliquots for cDNA amplification in 96-well PCR
864 plates, following the same PCR program as outlined previously. cDNA was purified twice using
865 0.8x SPRI beads and eluted in a final volume of 80 µl. 8x 1ng cDNA products were used for
866 Illumina sequencing library preparation through tagmentation with a Nextera XT kit, followed by
867 amplification and cleanup as stated above. Lineage tracing target site libraries were amplified
868 from cDNA and prepared fpr Illumina sequencing using previously described protocols[50].

869

870 **Spatial transcriptomics with Slide-tags**

871 Fresh frozen tissues were cryo-sectioned at 20 µm thickness using a Cryostat set at −17
872 to −18 °C. Precooled 6 mm square custom-made biopsy punches were used to punch and isolate
873 regions of interest from the tissue sections. The isolated tissue regions were carefully transferred
874 onto a precooled array, which was placed on top of a glass slide. A finger was briefly placed
875 underneath the slide to melt the tissue onto the array. Immediately after, the tissue, array, and
876 slide were placed on ice, and approximately 10 µl of dissociation buffer (82 mM Na_2SO_4, 30 mM

877 K_2SO_4, 10 mM glucose, 10 mM HEPES, 5 mM $MgCl_2$) was gently pipetted onto the tissue to
878 ensure it was fully covered. The array was then exposed to an ultraviolet (UV) light source (0.42
879 mW mm^{-2}, Thorlabs, M365LP1-C5, Thorlabs, LEDD1B) for 1 minute to cleave spatial barcode
880 oligonucleotides off the beads. After photo-cleavage, the array was incubated on ice for 7.5
881 minutes before being transferred to a well of a 12-well plate. To release the tissue from the array,
882 1 ml of extraction buffer (dissociation buffer with 1% Kollidon VA64, 0.2% Triton X-100, 1% BSA,
883 666 U ml^{-1} RNase-inhibitor) was gently dispensed onto the array, and the buffer was carefully
884 triturated up and down over the tissue 10–15 times. This process was repeated until the tissue
885 was completely released from the array. The array was then discarded, and mechanical
886 dissociation of the tissue was performed by triturating the supernatant 100–150 times using a 1
887 ml pipette to fully release the nuclei from the tissue. The extraction buffer containing the nuclei
888 was transferred to a 15 ml tube. The well was washed three times with 1 ml of wash buffer
889 (dissociation buffer with 1%BSA and 1: 100 RNase-inhibitor) and the washes were pooled into the
890 same 15 ml tube. The final volume of the wash buffer was adjusted to 10 ml. The nuclei were
891 centrifuged at 600g for 10 minutes at 4 °C. After centrifugation, 9.5 ml of the supernatant was
892 carefully removed. The pellet was resuspended and passed through a precooled 40 μm cell
893 strainer (Corning, 431750) into a 1.5 eppendorf tube. The 15 ml tube and cell strainer were
894 washed with 1 ml of wash buffer, and the nuclei were pelleted again by centrifuging at 600g for
895 10 minutes at 4 °C. After centrifugation, the supernatant was carefully removed, leaving
896 approximately 50 μl of wash buffer for nuclei resuspension. To determine cell count, 2 μl of
897 resuspended nuclei was mixed with 18 μl of 1: 100 diluted DAPI, and the nuclei were manually
898 counted using a C-Chip Fuchs-Rosenthal disposable hemocytometer (INCYTO, DHC-F01-5).
899 Based on the cell count, up to 25,000 nuclei were processed using the Chromium Next GEM
900 Single Cell 3' Reagent Kits v3.1 (with Feature Barcode technology for Cell Surface Protein, 10x
901 Genomics, PN-1000268). Lineage tracing target site libraries were amplified from cDNA and
902 prepared fpr Illumina sequencing using previously described protocols[50].
903
904 **H&E staining**
905 H&E was performed with a Leica ST5010 Autostainer XL and Leica CV5030 Fully
906 Automated Glass Coverslipper. Bright-field images were taken using the Leica Aperio VERSA
907 Brightfield, Fluorescence & FISH Digital Pathology Scanner under a ×10 objective. Tumour grade
908 was analysed in H&E-stained sections using an automated deep neural network developed by
909 Aiforia.
910

Sequencing

Sequencing was performed at using NovaSeq S4. For Slide-seq gene expression libraries: read1: 50bp, read2: 50bp, index1: 8bp was used. For Slide-seq Target Site libraries: read1: 44bp, read2: 260bp, index1: 8bp was used. For Slide-tags gene expression libraries: read1: 28bp, read2: 90bp, index1: 10bp, index2: 10bp was used. For Slide-tags gene expression libraries: read1: 28bp, read2: 260bp, index1: 8bp setting was used.

Immunofluorescence staining & imaging

15 μm-20 μm tissue sections were fixed in 4% PFA at room temperature for 10-15 min. The sections were washed twice in 1x PBS. Antigen retrieval was performed by boiling 1X IHC Antigen Retrieval Solution (ThermoFisher Scientific, 00-4955-58) and incubating tissue sections inside for 30 min until the solution cooled down, followed by washing tissue sections with 1x PBS and incubated in 0.3% PBST (0.3% Triton X-100 in PBS) at room temperature for 10 min. Three times of 1x PBS wash was then performed. Blocking (0.5% BSA and 0.1% Triton X-100 in 1x PBS) was performed at room temperature for 1 hour. Tissue sections were incubated with primary antibodies: VIM (1: 200, Biotechne, AF2105), CD31 (1: 200, Biotechne, AF3628), ARG1 (1: 200; Cell Signaling Technology, 93668), GLUT1 (1: 100; AbCam, ab195020), CD45 (1: 200, Cell Signaling Technology, 70257), and COL3A1 (1: 200, Proteintech, 22734-1-AP) at 4 °C overnight. Tissue sections were washed three times with 1x PBS and further incubated with secondary antibodies (donkey anti-goat 405, 1: 1000, ThermoFisher Scientific, A-48259; donkey anti-mouse 647, 1: 1000, ThermoFisher Scientific, A-31571; donkey anti-rabbit 647, 1: 1000, ThermoFisher Scientific) at room temperature for 2-3 hours. Tissue sections were then washed three times with 1x PBS, mounted and imaged using Dragonfly 201-40 High Speed Confocal Imaging Platform.

Mouse lung tissue dissociation for isolation of mesenchyme and alveolar macrophages

For isolation of mesenchymal cells and alveolar macrophages, mice were culled by cervical dislocation and lungs perfused with 10ml of cold PBS. Mouse lungs were inflated via intratracheal injection with 3ml of dispase solution (Fisher Scientific, 11553550), containing Collagenase I (GIBCO, 17100017) at 350U/ml. Lungs were carefully dissected out of the thoracic cavity, placed in a 50ml falcon and minced into small pieces. Cells were washes down with 3ml of PBS and samples were places in a shaking incubator at 37ºC, 190 rpm, for 45 min. 7.5ul of 1% DNase I (Sigma, D4527) was added to each sample in the final 10 min of incubation. The resulting cell suspensions were filtered through 100 μm and 40 μm cell strainers and washed with 2 ml of 10% fetal bovine serum (FBS) in PBS (PF10). Samples were centrifuged at 800 rpm for 5 min at

945 4ºC and pellets were resuspended in 1 ml of red blood cell lysis buffer (RBC buffer, Merck,
946 11814389001) for 60 seconds at RT. After lysis, 6 ml of Dulbecco's Modified Eagle Medium
947 Nutrient Mixture F-12 820 (DMEM/F-12, Invitrogen, 11330057) was added to neutralize the RBC
948 buffer. 500µL of filtered FBS was added slowly to the bottom of each tube and samples were
949 centrifuged again at 800rpm for 5 min at 4ºC. Cell pellets were resuspended in PF10 and placed
950 into Eppendorf tubes for antibody staining.
951
952 **Primary 3D mouse lung organoid co-cultures**
953 14 weeks post tumor initiation by Ad-SPC-Cre, tumour cells from the *Kras*$^{LSL\text{-}G12D/+}$;
954 *Trp53*$^{fl/fl}$; *R26*$^{LSL\text{-}Cas9\text{-}P2A\text{-}GFP}$ mice were dissociated and isolated (CD45$^-$ CD31$^-$ GFP$^+$) via
955 fluorescence-activated cell sorting (FACS) as previously described[50]. Mesenchymal cells (CD45$^-$
956 CD31$^-$ EpCAM$^-$) and alveolar macrophages (CD45$^+$ CD64$^+$ SiglecF$^+$) were isolated from adult wild
957 type C57BL/6 mice. The following antibodies were used: APC Anti-Mouse CD45 (559864, BD
958 Biosciences); PE/Cyanine7 anti-mouse CD64 (139313, Biolegend); PE anti-mouse CD170
959 (Siglec-F) (155505, Biolegend); APC Anti-Mouse CD31 (551262, BD Biosciences); PE/Cyanine7
960 anti-mouse CD326 (Ep-CAM) (118216, Biolegend).
961 Using sorted cells, tumour organoid co-cultures were stablished according to previous
962 publications78. Briefly, freshly sorted tumour and stromal cells were centrifuged at 300g for 10
963 min at 4ºC and resuspended in 3D basic media composed by DMEM/F12 (GIBCO, 11330-032)
964 supplemented with 10% of FBS and Insulin-Transferrin-Selenium (ITS, Corning, 25-800-CR).
965 Cells were counted and combined to obtain mixtures of 5k tumour cells with 45k mesenchyme
966 and 30k alveolar macrophages per well. Cells were centrifuged at 300g for 10 min at 4ºC,
967 resuspended in 100 µl GFR-Matrigel (Corning, 356231) containing 50% 3D basic medium and
968 platted in a 24-well Transwell insert with 0.4 µm pore (Greiner, 662641). 500 µL of 3D basic
969 medium was added in the lower chamber and cells were cultured at 37ºC with 5% CO2. Cultures
970 containing 5k of tumour cells were also stablished, following the same protocol. 10 µM Rho kinase
971 (ROCK) inhibitor Y-27632 (Cayman Chemical. #10005583) was added to all cultures for the first
972 48h. After the initial 48h, cells were transferred to either 37ºC with standard 20% oxygen (Normal
973 oxygen) or to 37ºC with 5% oxygen (Hypoxia) and were maintained for an additional 9 days, with
974 media changed every other day. At the end of the experiment, cultures were dissociated and
975 GFP+ cells sorted and stored for RNA extraction. Total RNA was isolated from the sorted cancer
976 cells (~20k cells per sample) using PicoPure RNA isolation Kit (ThermoFisher Scientific,
977 KIT0204). cDNA was generated using High-Capacity cDNA Reverse Transcription Kit
978 (ThermoFisher Scientific, 4368814). Quantitative PCR was performed using PowerTrack SYBR

979 Green Master Mix (ThermoFisher Scientific, A46012). All qPCR primers are listed in
980 **Supplementary Table 5**.
981
982 **Human LUAD FFPE sample staining and quantification**
983 Formalin-fixed, paraffin-embedded (FFPE) human lung adenocarcinoma (LUAD) tissue
984 sections were first incubated at 70 °C for 1 hour. Deparaffinization was then performed using a
985 Leica ST5010 Autostainer XL with the following settings: 60 °C incubation for 15 min, followed by
986 3x xylene washes for 3 min each, 2x 100% ethanol washes for 3 min each, 1x 95% ethanol wash
987 for 3 min, and water wash for 5 min. Sections were subsequently subjected to antigen retrieval
988 by de-crosslinking in a vegetable steamer for 30 min using Antigen Retrieval Buffer (pH 6.0,
989 Abcam, ab93684) and were then cooled to room temperature. Permeabilization was performed
990 by incubating the sections in 0.3% PBST (0.3% Triton X-100 in 1x PBS) for 10 min at room
991 temperature, followed by three washes in 1x PBS. Blocking was carried out for 1 hour at room
992 temperature using a blocking buffer containing 0.5% BSA and 0.1% Triton X-100 in 1x PBS.
993 Sections were incubated overnight at 4 °C with primary antibodies. For quantifying GLUT1, SPP1,
994 and CD68 signals, anti-GLUT1-Alexa Fluor 647 (1:100; Abcam, ab195020) and anti-CD68-Alexa
995 Fluor 555 (1:200; CST, 23308) were used; anti-SPP1 (1:200; Merck, HPA027541) was applied to
996 adjacent sections. For quantifying GLUT1 and VIM signals, anti-GLUT1 (1:100; Abcam,
997 ab195020), anti-VIM (1:200; Biotechne, AF2105), and anti-ACTA2 (1:250; Thermo Fisher
998 Scientific, MA1-06110) were used. For unconjugated primary antibodies (e.g., SPP1), sections
999 were washed three times in 1x PBS and incubated for 2–3 hours at room temperature with
1000 appropriate secondary antibodies: donkey anti-rabbit Alexa Fluor 594 (1:1000; Thermo Fisher
1001 Scientific, A-21207), donkey anti-goat Alexa Fluor 405 (1:1000; A48259), donkey anti-rabbit Alexa
1002 Fluor 647 (1:1000; A32795), and donkey anti-mouse Alexa Fluor 488 (1:1000; A32766). Nuclei
1003 were counterstained with DAPI or Propidium Iodide (PI), followed by three 1x PBS washes.
1004 Finally, sections were mounted and imaged using a Dragonfly 201-40 High-Speed Confocal
1005 Imaging Platform.
1006 For quantification, 3-5 randomly selected 2 x 2 tiled scan images at 10x magnification
1007 were captured from annotated tumor regions, as determined by prior H&E staining and pathologist
1008 review. Each 2 x 2 tiled image was divided into four quadrants: top-left, top-right, bottom-left, and
1009 bottom-right. For SPP1 and GLUT1 quantification, these subregions were assessed for GLUT1
1010 and SPP1 signal positivity, and regions were classified into four categories: $GLUT1^{+}SPP1^{+}$,
1011 $GLUT1^{+}SPP1^{-}$, $GLUT1^{-}SPP1^{+}$, and $GLUT1^{-}SPP1^{-}$. For quantifying VIM signal associated with

1012 tumors, only VIM^{+}/ACTA2^{-} regions were considered VIM-positive, while VIM^{+}/ACTA2^{+} regions
1013 were classified as VIM-negative.
1014

1015 **QUANTIFICATION AND STATISTICAL ANALYSIS**

1016 **Slide-seqV2 gene expression quantification and quality-control**

1017 A python implementation of Kallisto-bustools[97] (*kb_python,* version 0.27.3 available at
1018 https://github.com/pachterlab/kb_python) was used for transcript quantification and processing
1019 from raw FASTQs produced with Slide-seq. Specifically, we utilised the *count* procedure
1020 implemented in Kallisto that quantifies the number of UMIs in a Slide-seq library that map to each
1021 transcript sequence in the provided reference (here, *mm10*). To account for the unique read
1022 structure of the Slide-seq library, we invoked the *count* procedure with the flag -x
1023 "0,0,8,0,26,32:0,32,41:1,0,0". To determine a whitelist of barcodes to use during quantification,
1024 we matched barcodes identified with kallisto to the spatial barcodes and their coordinates
1025 observed during *in situ* sequencing of the Slide-seq array during fabrication[56,57]. We then used a
1026 custom script to assign spatial coordinates, identified during *in situ* sequencing of the Slide-seq
1027 array prior to running the assay, to quantifications from the kallisto pipeline and returned an
1028 AnnData structure containing the spatially-resolved transcript abundances for each spot. To
1029 supplement the barcode filtering during the kallisto pipeline, we applied an extra filter requiring at
1030 least 150 UMIs observed in a spot. For most analyses, we utilise log-normalised counts where
1031 each cell's UMI total is scaled to the median library size and a log1p transformation is applied.
1032 When scaled counts are used, we additionally use Scanpy's *scale* function with a max value of
1033 10.
1034

1035 **Slide-tags gene expression quantification and quality-control**

1036 Similar to Slide-seq processing, we utilised the python implementation of Kallisto-
1037 bustools[97] (*kb_python,* version 0.27.3 available at https://github.com/pachterlab/kb_python) to
1038 quantify transcript abundance from FASTQ data. As this data represents reads from sequencing
1039 single-nuclei with the 10X V3 kit, we utilised the *--umi-gene*, *--workflow nucleus*, and *-x 10XV3*
1040 flags. Similar to the Slide-seq analysis, we utilised the mm10 transcriptome reference.

1041 After transcript quantification, we applied several quality-control procedures. First, we
1042 removed background gene expression signal from ambient RNA by applying Cellbender[98]
1043 (version 0.3.0, available at https://github.com/broadinstitute/CellBender) to the unfiltered gene
1044 expression counts. We used default settings for all libraries, except for 10X Library 9 where we
1045 used the following flags: --empty-drop-training-fraction 0.15, --total-droplets-included 20000, --

learning-rate 0.0001, and --epochs 300. After running Cellbender, we applied further cell-filters to remove outliers with high mitochondrial or ribosomal content (between 5-15% for libraries). We further inspected the count distribution in each library and removed nuclei with excessively high UMI content (approximately 20,000 UMIs). All quality-control was performed with Scanpy[99] (version 1.10.0, downloaded via *pip*). For most analyses, we utilise log-normalised counts where each cell's UMI total is scaled to the median library size and a log1p transformation is applied. When scaled counts are used, we additionally use Scanpy's *scale* function with a max value of 10.

Slide-seq lineage tracing target-site data processing

To begin processing target-site data, we trimmed reads from Slide-seq libraries using cutadapt[100] (version 4.1) with the following flags: -m :250 --max-n 0.2 --discard-untrimmed -O 10 --no-indels --match-read-wildcards -e 2 -j 16 --action retain -G AATCCAGCTAGCTGTGCAGC. We then applied Cassiopeia[41] (version 2.0.0, available at https://github.com/YosefLab/Cassiopeia) to trimmed FASTQs using the "slideseq2" chemistry and specific parameters for Slide-seq libraries. First, to account for the possibility of multiple cells observed in a given spot, we allowed allele conflicts (*allow_allele_conflicts* = *True*) and did not enable doublet filtering. While we performed intBC whitelist correction, we did not perform additional error correction to remove intBCs with conflicting alleles (this is similarly motived by the fact more than one cell can be observed in a given spot). We additionally relaxed the UMI/cell threshold to account for reduced capture of Slide-seq assays (*min_umi_per_cell* = *2*). Finally, we utilised the "likelihood" method for UMI collapsing, with *max_hq_mismatches* = 3 and *max_indels* = 2. Other settings remained default. This pipeline produced a cleaned allele table, reporting the set of intBCs and alleles for each observed spot, that was used for tree reconstruction.

Slide-tags lineage tracing target-site data processing

Cassiopeia[41] (version 2.0.0, available at https://github.com/YosefLab/Cassiopeia) was used to process FASTQs containing target-site data. As Slide-tags represents single-nucleus data, we utilised default settings except for a more relaxed UMI/cell cutoff (*min_umi_per_cell = 5)* to reflect the reduced sensitivity of single-nucleus sequencing. As a part of default settings, we corrected cell barcodes to those observed after quality-control filtering, corrected intBCs to a whitelist for the corresponding mESC (E1) with a distance threshold of 1, and performed UMI (with a maximum distance of 2) and intBC error correction (minimum UMI support of 5) to correct for conflicting target sites observed in the same nuclei. Doublets were filtered out using the default

conflicting threshold of 35%. This pipeline produced a cleaned allele table, reporting the set of intBCs and alleles for each observed spot, that was used for tree reconstruction.

Slide-tags spatial barcode processing

Spatial mapping of Slide-tags nuclei was achieved as previously described[58]. Briefly, reads from spatial barcode FASTQ files were filtered for those containing the spatial barcode universal primer constant sequence and cell barcode sequences from a called cell barcode whitelist generated by the gene expression pipeline (see above section entitled “Slide-tags gene expression quantification and quality-control”). Spatial barcode sequences were matched with a whitelist of in situ sequenced spatial barcodes, assigning spatial coordinates to each true spatial barcode. The set of spatial barcodes and the corresponding x,y coordinates for each cell barcode were clustered with DBSCAN[101] (implemented in the R package *dbscan*, version 1.1−11). For cell barcodes with a single cluster of spatial barcodes, spatial barcodes not contained in the cluster were filtered out and a UMI-weighted centroid of the remaining spatial barcodes represented the x,y coordinates of the cell barcode. DBSCAN parameters were determined from a sweep of minPts values (3 to 15) under a constant eps = 50. The chosen minPts positioned the highest proportion of cell barcodes.

Spatial imputation of lineage-tracing data

To recover lineage-tracing data for reconstruction on spatial assays, we performed spatially-informed imputation of target site data. To begin, we first created a character matrix from the allele tables constructed from target-site lineage tracing processing. In this character matrix, denoted as X, each row corresponds to a cell (or spot) and each column corresponds to a particular cut site in an integration barcode (intBC). For clarity of notation, we refer to each cut-site/intBC pair as a character, and thus in our system a character matrix will have (|intBCs| x 3) columns. The entry $\mathrm{X}[i,j]$ denotes the edit (which we refer to as a “state”) observed at the ith cell/spot in the jth character. The missing data rate refers to the proportion of entries in this character matrix that do not have data that pass our quality-control filters.

To perform spatial imputation, we first constructed a spatial nearest-neighbour graph (N) such that each spot was connected to all other spots within 30μm of the spot. For each missing entry in character matrix, i,j we queried the frequency of states at character j in all neighbours of spot i in N. If the concordance of a particular state was higher than 80% in these neighbours, then we replaced the entry $X[i,j]$ with this state. To minimize the effect of nearby stromal cells in a neighbourhood – which should not have active lineage-tracing – we did not allow this state to

be 0, the uncut state. To maximise the alleles were used during spatial imputation, we required each state to be supported by at least 3 UMIs. We reported this procedure for each missing entry in the character matrix for a total of 5 iterations which continued to remove missing data from the character matrices with no apparent reduction in accuracy in simulations or held-out real data (**Extended Data Fig. 1j-n**).

Benchmarks of imputation and reconstruction accuracy

To benchmark the accuracy of spatial imputation and downstream effects on tree reconstruction, we utilised two different strategies:

- Synthetic data: First, we utilised the Cas9-based lineage-tracing simulation framework in Cassiopeia[41] (version 2.0.0, available at https://github.com/YosefLab/Cassiopeia). Specifically, we simulated trees using Cassiopeia's *BirthDeathSimulator* with the following parameters: 5000 extant cells, and utilised a LogNormal birth-waiting distribution parameterised by $\log(f)$ where *f* is a fitness coefficient that accumulates with each cell division (in each cell division, a new coefficient $f \sim N(0, 0.25)$ is drawn and added to the base fitness) and a standard deviation of 0.5. Then, we simulated lineage tracing data onto the tree with Cassiopeia's *Cas9LineageTracingDataSimulator* with desired mutation proportion of 0.7, 100 states, 39 cut sites (representing our system with approximately 13 intBCs, each with 3 cut-sites), and no missing data rates at this point. Then, we simulated spatial coordinates on each tree using the *ClonalSpatialDataSimulator* over a shape of (1,1,1) and sampled a 2D slice from this 3D simulation at random. Finally, we subsampled from this spatial array using the *UniformLeafSubsampler* in Cassiopeia with a rate of 0.4 (resulting in lineages with 2,000 observations) and induced random dropout at various rates: [0.1, 0.25, 0.5, 0.6, 0.7, 0.9]. We simulated 10 trees for each parameter combination. As the spatial array simulated does not exactly match that from Slide-seq, we applied a modified *k-nearest-neighbour* graph construction approach, linking together spots to their closest 10 neighbours and performed spatial imputation (see section titled "Spatial imputation of lineage-tracing data"). We required concordance of 0.8 for the selected state and at least 5 votes. Since this simulated data does not include any normal cells, we do allow the imputation of the state 0. We reported the accuracy of this imputation strategy in **Extended Data Fig. 2e**). Then, we compared the tree reconstructing accuracies using the *triplets_correct* function in Cassiopeia for reconstructions with or without imputation and for different reconstruction strategies: modified Neighbour-Joining, Cassiopeia-Greedy, or a hybrid of these two approaches (see section "Phylogenetic reconstruction").

- Simulated held-out Slide-seq data: In the next experiment, we assessed the accuracy of recovering target-site data that was held-out from real Slide-seq data. To do this, for a given Slide-seq array, we masked out 10% of the observed data (supported by at least 3 UMIs) and performed spatial imputation in neighbourhoods of 30μm using the strategy described previously (see section titled "Spatial imputation of lineage-tracing data). Similarly, we required a concordance of 0.8 and at least 5 votes in support of the imputed allele. We only considered samples where at least 10 states were imputed. Random predictions were obtained by shuffling the node labels in the neighbourhood graph. We reported the average accuracy and total number of imputed values over five replicates in **Extended Data Fig. 2h**.

Simulation benchmarks of lineage-tracing pre-processing

As a feature of the Slide-seq is that multiple cells may be observed in one spot[57], multiple conflicting alleles can be observed for a given target site in a single spot. Typically, this would break the assumption of the Cassiopeia reconstruction pipeline (in single-cell approaches, we assume that only one allele can be tied to a given intBC and perform error correction or filtering otherwise). However, we implemented new reconstruction algorithms that can handle multiple conflicting states in each spot (see section entitled "Phylogenetic reconstruction") and simulated the effects of various pre-processing techniques.

First, we simulated trees on two-dimensional surfaces where various proportions of cells would be grouped together based on their spatial location. To do so, we simulated simple binary trees of 2000 cells and overlaid lineage-tracing data with Cassiopeia's *Cas9LineageTracingDataSimulator* function using the following parameters: 39 characters, a mutation proportion of 0.5, and no missing data. We then merged together cells using Cassiopeia's *SupercellularSampler* method with rates of [0.1, 0.2, 0.3, 0.4, 0.5, 0.6]. We simulated 32 replicates.

For each replicate, we pre-processed character matrices according to three strategies. Here, the entry of the ith cell and j^{th} character (denoted as $\mathrm{X}[i,j]$) would contain a set of states $\mathrm{X}[i,j] = \{s_1, s_2, \dots, s_k\}$, each state occurring at some frequency $\mathrm{f}(s_i) = f_i$. In the first strategy ("collapse duplicates") we take the unique set of states so that $\mathrm{X}[i,j] = \{s_1, s_2, \dots, s_{k'}\}\ s.\mathrm{t.}\ f_i = 1\ \forall\ \mathrm{i} \in k'$; in the second strategy ("most common") we take the most common state, such that $\mathrm{X}[i,j] = argmax_{f(s')\ \forall s \in k} s'$; and the third strategy ("all states") we do not perform any filtering. In **Extended Data Fig. 2a** we report the tree reconstruction error (measured with normalised Robinson-Foulds distance) for trees reconstructed with Neighbour-Joining[63].

Phylogenetic reconstruction on Slide-seq data

To enable phylogenetic reconstruction on Slide-seq data in which multiple cells can be contained in a single spot and thus conflicting alleles are present, we implemented a Hybrid Cassiopeia-Greedy & Neighbour-Joining algorithm that could utilise conflicting allele states.

For Cassiopeia-Greedy, we modified the splitting decision rule to account for all states observed in a spot. Cassiopeia-Greedy is a simple, heuristic-based algorithm for reconstructing phylogenies that iteratively finds the most common state in a given population and splits samples into groups based on the presence or absence of the state. It is based on a perfect-phylogeny reconstruction algorithm[102] and has an efficient runtime of *O(mn)* for a population of *n* samples and *m* characters. Here, we changed the procedure to find the state with the highest frequency by allowing each sample to carry multiple states in a character. The runtime of this algorithm is still polynomial in the size of the sample population – *O(n(ms))* where in the worst case scenario every single state is observed in every single character; given the size of the spatial array, this is exceedingly uncommon and typically 1-3 cells are captured per spot[57].

For Neighbour-Joining, we utilised the standard algorithm[63] but with a modified distance map that accounts for multiple states per spot. Specifically, we implemented a new dissimilarity metric that takes in two sets of states S_1 and S_2 and computes all the pairwise allelic dissimilarities and reports a linkage similar to hierarchical clustering. Here, we use the modified allelic dissimilarity for two states s_i, s_j to compute distances between pairs of states, previously described[41,47,50]:

$$h'^{(s_i,s_j)} = \begin{cases} 2 \;\; if\; s_i \neq s_j \neq 0 \\ 1 \;\; if\; s_i \neq s_j \;\; and\; (s_i = 0\; or\; s_j = 0) \\ 0 \;\; otherwise \end{cases}$$

In the case where weights are passed in, then the dissimilarity function is computed as follows:

$$h'^{(s_i,s_j)} = \begin{cases} \mathrm{w_i} w_j \;\; if\; s_i \neq s_j \neq 0 \\ w_i \;\; if\; s_i \neq s_j \;\; and\; s_j = 0 \\ w_j \; if\; s_i \neq s_j \; and\; s_i = 0 \\ 0 \;\; otherwise \end{cases}$$

Then, we utilised a single linkage function such that only the smallest modified allelic dissimilarity across all pairs of states in S_1 and S_2 was used. This is to maintain such that if the same state is observed in two spots, the dissimilarity returned is 0.

For the hybrid reconstruction, we utilised the modified Cassiopeia-Greedy algorithm described above until subpopulations of size 1000 cells were found, at which point Neighbour-Joining with the modified dissimilarity metric was used to resolve phylogenetic relationships. We utilised state probabilities inferred from all Slide-seq and Slide-tags datasets and used the weight $-\log(p_i)$ for state s_i during tree reconstruction.

Phylogenetic reconstruction on Slide-tags data

We utilised the standard Cassiopeia-Hybrid[41] algorithm for reconstructing Slide-tags phylogenies. Briefly, this approach applies the heuristic-based Cassiopeia-Greedy algorithm to reconstruct relationships between the major subclones and then applies the maximum-parsimony-based Cassiopeia-ILP algorithm to solve fine-grained phylogenetic structure in smaller populations. As previously described in detail[41], Cassiopeia-ILP proceeds by building a potential graph of all possible ancestral states (constrained in size by a user-defined parameter) and solves for the maximum-parsimony phylogeny by reconstructing a Steiner Tree on this data structure. The Steiner Tree problem is solved via an Integer Linear Program (ILP) allowed a certain time to converge. Here, the transition between Cassiopeia-Greedy and -ILP algorithms is determined by the distance to the latest common ancestor (LCA) of a subpopulation.

We applied the Cassiopeia-Hybrid algorithm with state priors inferred from all samples[41,47,50], determined the switch between Greedy and ILP algorithms using an LCA cutoff of 20, devised a potential graph of 10000 nodes with a maximum distance of 15 across nodes (maximum_potential_graph_lca_distance=15), and allowed the ILP 12600s to converge.

CNV detection and analysis

inferCNV (https://github.com/broadinstitute/infercnv, version 1.18.1) was used to detect CNVs from Slide-tags or Slide-seq expression data. For Slide-tags data, inferCNV was used in "subcluster" mode with leiden resolution of 0.0005 and the following parameters: HMM=TRUE, BayesMaxPNormal=0.2, min_cells_per_gene = 1, cutoff = 0.1. Otherwise, default parameters were retained.

For Slide-seq data, owing to the sparsity in transcript capture, we performed inferCNV analysis on pooled gene expression data. Specifically, we combined the gene expression data for the adjacent spots into bins of size 50μm (akin to 10X Visium data). Then, inferCNV was used in "subcluster" mode with leiden resolution of 0.0005 with the following parameters: window_length = 201, HMM=TRUE, BayesMaxPNormal=0.5, min_cells_per_gene = 1, and cutoff=0.2. Otherwise, default parameters were retained.

1245 For counting the number of CNVs for the benchmarking analysis in **Extended Data Fig.**
1246 **3a**, we used the HMM CNV predictions (*Pnorm_0.2.pred_cnv_regions.dat). To assess the
1247 Nearest Neighbour Purity between inferCNV data and lineage-tracing trees, we computed the
1248 fraction of leaves whose nearest neighbor shared the same inferCNV grouping (as reported in
1249 infercnv.observation_groupings.txt of the inferCNV pipeline). We removed inferCNV groupings
1250 with fewer than 20 cells. This purity score was compared to an empirical background in which
1251 inferCNV cluster labels were shuffled 1000 times.
1252
1253
1254 **Slide-tags cell type annotation**
1255 After performing quality-control on Slide-tags gene expression data, we assigned cell
1256 types first by integrating Slide-tags data with an annotated single-cell gene expression reference
1257 dataset of KP-Tracer tumours[50] with scANVI[103]. To do so, first identified 4,750 variable genes
1258 using Scanpy's[99] *highly_variable_genes* function using the *flavor="seurat_v3"* and raw counts.
1259 We then trained an scVI model[104,105] on the joint dataset and these variable genes using 3 layers
1260 and 70 latent dimensions over 1000 epochs. Then, we transferred labels from the single-cell
1261 reference dataset to the Slide-tags nuclei with scANVI utilizing 200 samples per label and 100
1262 epochs. Through this, we used the *gene_likelihood="nb"* setting in training models and used the
1263 technology – Slide-tags or single-cell – variable to signify batch.
1264 After training this model, subset to the scANVI embeddings to the Slide-tags data only and
1265 re-clustered the data with Scanpy[99] using the Leiden algorithm[106] and resolution 1.2. We then split
1266 clusters into those that appeared to derive from tumour/epithelial cells or those that derived from
1267 the stroma. To call tumour or epithelial clusters, we evaluated if a cluster had an abundance of
1268 tumour nuclei (defined as nuclei with target site data and at least 20% of their sites containing
1269 indels) or expressed the epithelial-lineage marker *Nxk2-1*. Immune cell clusters were identified
1270 based on the marker *Cd45 (Ptprc)* and other stromal cells were identified by expression of *Pdgfra,*
1271 *Col1a1,* or *Col5a1* (fibroblasts) or *Pecam1* (endothelial cells). For each subsetted dataset
1272 (tumour/epithelia or stromal), we reclustered the data and annotated cell types based on
1273 annotations predicted with scANVI and differentially expressed genes identified with Scanpy's
1274 *rank_genes_group* function (using the Wilcoxon test).
1275
1276 **Assessment of Slide-tags tumour cell type signatures in previous KP-Tracer data**
1277 To test the portability and accuracy of the tumour clusters identified in Slide-tags, we
1278 assessed the activity of gene signatures in the previous KP-Tracer data[50]. Specifically, we for

1279 each cell-type identified in Slide-tags, we computed the top 100 differentially-expressed genes
1280 using the Wilcoxon test in Scanpy[99] and further filtered genes to have a log-fold change > 1 and
1281 an FDR-corrected p-value <= 0.01, and an AUROC of at least 0.6. We then used these genes to
1282 define a transcriptional signature for each Slide-tags cell type. each of these signatures, we
1283 scored the activity in cell types identified in Slide-tags data and the previous KP-Tracer dataset
1284 using the *score_genes* function using *n_bins=30* and *ctrl_size* equal to the number of genes in
1285 the gene set. Signatures were computed on scaled, log-normalised counts. The result of this
1286 analysis is presented in **Extended Data Fig. 4b**.
1287
1288 **Slide-seq spatial community detection and scoring**
1289 To identify spatial communities in Slide-seq data, first applied the Hotspot[107] algorithm for
1290 detecting spatially autocorrelated gene sets on each sample. In the spatial mode, this algorithm
1291 constructs a nearest neighbour graph based on spatial coordinates, computes an autocorrelation
1292 statistic for each gene, and then identifies modules of genes that have significant pairwise
1293 autocorrelation values. Here, we applied Hotspot with 20 neighbours, and FDR threshold of 0.01
1294 to identify spatially autocorrelated genes, and a minimum module size of 50 genes.
1295 Then, to identify robust modules of genes that appear across tumours, we assessed the
1296 Jaccard overlap between all pairs of modules across all tumours and filtered out modules that did
1297 not have a Jaccard overlap of at least 0.2 with at most one other module. We then performed Z-
1298 normalization on these Jaccard statistics and clustered these using hierarchical clustering (using
1299 the “ward” method on Euclidean distances) and identified 11 clusters, representing robust spatial
1300 modules.
1301 As these robust modules are collections of modules across all samples we analysed, we
1302 distilled these down to a set of genes – representing what we call a “spatial community” in this
1303 study – by taking genes that appear in at least 25% of the modules in the robust module. Using
1304 these genes in the spatial community, we compute the activity of these communities for each spot
1305 (termed “community scores”) using the *score_genes* function in Scanpy[99] with *ctrl_size=100* and
1306 *n_bins=30.* We computed these scores on scaled, log-normalised gene expression counts. To
1307 obtain community assignments for each spot, we took the community with the highest score.
1308
1309 **Tumour segmentation**
1310 To segment tumours, we utilised the SpatialData[108] package and the napari-spatialdata
1311 viewer for interactive annotation. To identify tumour areas on a sample, we overlaid phylogenetic
1312 subclones and the number of target-site UMIs detected and manually segmented areas that

appeared to be (a) phylogenetically related and (b) had elevated target-site UMIs indicative of tumour regions. We saved these annotations and used the segmentations to perform downstream analysis on a tumour-by-tumour basis.

Fitness signature calculation

To quantify fitness signature scores, we utilised a gene set that was found to be associated with changes in fitness from our previous single-cell KP-Tracer study[50]. Using this gene set, we quantified the transcriptional activity for each spot in Slide-seq data by applying the *score_genes* function in Scanpy[99] with *ctrl_size=100* and *n_bins=30.* We computed these scores on scaled, log-normalised gene expression counts.

Phylogenetic fitness inference

We quantified fitness on Slide-seq and Slide-tags phylogenies by utilizing the *LBIFitness* fitness estimator in Cassiopeia[41]. This function wraps a fitness estimator based on the "local branching index" as previously described[109]. This procedure has been previously used in our system[50]. Primed by the true single-cell resolution of Slide-tags trees, we estimated branch lengths using the *IIDExponentialMLE* branch length estimator in Cassiopeia. This function implements a function that provides maximum-likelihood branch lengths on a tree topology given the pattern of edits observed in the leaves and an assumptions about the irreversibility of Cas9 editing[110]. Using the branch lengths determined by this maximum-likelihood procedure, we estimated single-cell fitness on Slide-tags trees.

Due to the increased missingness on Slide-seq trees and the fact that MLE-based branch length approaches have not been benchmarked on Slide-seq data, we performed a more conservative branch length estimation, as done previously[50]. Here, branches had a length of 1 if they had any mutations along them, otherwise they had a branch length of 0. Using these branch lengths, we estimated single-cell fitness on Slide-seq trees.

Single-cell clonal plasticity quantification

To estimate single-cell clonal plasticity on phylogenies, we applied approaches described in our previous studies[50,68]. Specifically, on Slide-tags data where we have true single-cell data and associated cell type identities, we applied the *score_small_parsimony* procedure to all nodes in a tree using *meta_item="cell_type"* and normalised by the number of leaves in the subtree induced by the node. Then, we computed plasticity for each cell by averaging together all the normalised parsimonies.

Since we do not have true single-cell resolution for Slide-seq data, we employed the L2 plasticity score described in our previous study[50], using community scores. Specifically, let C_i be the vector of community scores associated with spot i. For this spot i we found its closest phylogenetic neighbours (denoted by set *N*) and then computed the L2-Plasticity ($L2_p(i)$) for this spot by the average Euclidean distance to the vector of community scores for these neighbours:

$$L2_P(i) = \frac{1}{|N|}\sum_{k\in N}\left|\left|C_i - C_k\right|\right|_2$$

All scores were unit scaled.

Differential expression and abundance in neighbourhoods of high-fitness cells

To identify changes in gene expression and spatial communities associated with fitness, we first stratified cells into high- and low-fitness groups. In Slide-seq data, we computed single-cell fitness scores (see section above entitled "Phylogenetic fitness inference") and identified a threshold separating two modes using *scipy.signal.argrelmin* in the merged fitness distributions and split spots into high-fitness groups and low-fitness groups based on this threshold. Only tumours with at least 200 observations with lineage-tracing data were used. As each fitness distribution is normalised within individual tumours to be unit-scaled, this approach finds a global pattern in high- and low-fitness cells. Then, we constructed a neighbourhood graph connecting each spot to all other spots within 30μm. The community scores for all communities were computed in these neighbourhoods and the distributions in neighbourhoods of high- and low-fitness cell were reported in **Extended Data Fig. 7d.**

In Slide-tags data, high and low-fitness cells were similarly determined from the distribution of all fitnesses using *scipy.signal.argmin*. As Slide-tags is sparser than Slide-seq, we constructed neighbourhoods using the closest 20 cells (an example is shown in **Extended Data Fig. 7a**). We then identified the differentially-expressed genes in neighbourhoods of high- and low-fitness cells of all Macrophage and Fibroblast subsets using the t-test as implemented in Scanpy's[99] *rank_genes_groups* function. For the Macrophage analysis, we evaluated the Alveolar Macrophages, *Arg1*+ TAMs, *Pecam1*+ TAMs, and *Vegfa*+ TAMs; for the Fibroblast analysis we evaluated the *Wt1*+ fibroblast, iCAF-like and myCAF-like populations. Genes expressed in fewer than 50 cells were filtered out, and the differential expression statistics for the top 10,000 genes were computed. Genes with an absolute log2-fold-change > 1 and an FDR-corrected p-value < 0.01 were marked as significantly differentially expressed. To compute enrichments in these

neighbourhoods, we computed the frequency of cell types in neighbourhoods of high- and low-fitness cells and divided by the expected fraction of these cell types given the overall distribution and size of the Slide-tags array.

GO Term analysis of differentially-expressed genes was performed using gseapy[111] (version 1.1.3) with the following gene sets: “WikiPathways_2019_Mouse”, “Reactome_2022”, “GO_Biological_Process_2023”, “GO_Molecular_Function_2023”, and “KEGG_2019_Mouse”. Significant terms are reported in **Supplementary Table 3**.

Differential expression in neighbourhoods of high-plasticity cells in Slide-seq

Similar to the fitness-based analysis (see section entitled “Differential expression in neighbourhoods of high-fitness cells”), we stratified cells into high- and low-plasticity groups. After quantifying the L2-clonal plasticity score in Slide-seq data, we determined a threshold separating high- and low-plasticity regions if a cell had greater plasticity than the 60th percentile or less than the 40th percentile, respectively. Then, we constructed a neighbourhood graph connecting each spot to all other spots within 30μm. The community scores for all communities were computed in these neighbourhoods and the distributions in neighbourhoods of high- and low-plasticity cells were reported in **Extended Data Fig. 7e.**

Cell-cell communication analysis of Slide-tags data

Ligand–receptor (LR) and cell type level interaction analysis was performed with Ligand And Receptor In Spatial Transcriptomics (*LARIS*) on the Slide-tags dataset. LARIS is a computational tool for spatial LR activity inference implemented in Python, capable of producing single cell, cell-type, or tissue region-level predictions in seconds. LARIS is based on the *in silico* spatial diffusion of ligands and receptors to simulate intercellular communication. Each single cell (or bead) with a known spatial location is assigned an LR score based on the expression of ligands and receptors in the nearest neighbours. This integrated LR score can be used for easier visualization of interactions in space. To capture spatial interaction patterns that show unique localization, cosine similarity is employed on the observed LR activity patterns against shuffled cell locations. This yields a ranked list of LR interactions that have localized spatial expression patterns, helping identify potentially interesting interactions cell type (or other) label-free. The cell type level prediction scores are calculated by combining the average of the LR integration scores with the specificity of ligands and receptors for each cell-type combination, resulting in a ranked list of cell type to cell type communication based on interaction strength and specificity. To identify region-specific interactions independently of cell type, regional labels (e.g., cancer clones) can be

assigned to cells, and statistical tests or other approaches can be applied to the LR scores to identify differentially expressed ligand and receptor pairs.

Raw counts were first log-normalized using the Scanpy implementation of *normalize_total (target_sum=10000)* and *log1p* functions. The latest mouse *CellChatDB*[112], formatted for *LARIS*, served as the reference for known LR pairs.

To calculate integrated LR scores, which quantify the predicted interaction strength based on receptor and ligand gene expression in spatially proximate cells, we applied the *calculateLigandReceptorIntegrationScore* function from *LARIS* (*number_nearest_neighbors=20*). Interactions exhibiting spatial specificity and variability compared to randomly shuffled locations were identified using the *runZoneTalk* function (*number_nearest_neighbors=20, mu=0.2, sigma=100*). To infer and rank interactions between each cell type combination, we employed the *calculateZoneTalkScoreByCellType* function (*mu=100, expressed_pct=0.05, mask_threshold=1e-8*), which considers the abundance, specificity, and spatial localization of each interaction. Visualisations of the -log10(interaction scores) of the top cell-type-specific interactions are displayed in **Extended Data Figure 8** and reported in **Supplementary Table 4**.

To detect differentially expressed LR pairs between expanding and non-expanding clones, each cell was labeled by both cell type and clonality. The COSG tool[113], a cosine similarity–based marker gene identification method (*mu=1000, expressed_pct=0.15*), was applied to LR scores at both regional clonality and cell type levels. Visualization of the resulting LR scores was performed using Scanpy.

Coarse-grained alignment of Slide-seq data

To track the three-dimensional structure of clones across sampled layers in **Fig. 4**, we utilised the non-imputed processed target-site data (see section entitled “Slide-seq lineage tracing target-site data processing”). To maximise fidelity of slide registration, we enforced hard quality-control cutoffs, requiring each spot be supported by at least 7 UMIs and then subsequently each intBC-allele to be supported by at least 5 UMIs. We filtered out spots that had less than 20% of their sites reporting indels, or more than 70% missing data. We then computed modified allelic distances (see section above entitled “Phylogenetic reconstruction on Slide-seq data”) between all pairs of spots across layers. Modified allelic distances here are normalised by the number characters shared between two spots (thus are normalised to values between 0-2). For computational reasons, we did not allow ambiguous alleles (taking only the most frequent allele per intBC in a spot) as the distance calculation is memory- and time-intensive. Using this distance matrix, we computed allelic evolutionary couplings using *compute_evolutionary_coupling* function

in Cassiopeia with the following parameters: *minimum_proportion = 0.0002, number_of_shuffles = 100*. We then normalised the evolutionary coupling as previously described[50], as so:

$$\tilde{E}(i,j) = e^{\frac{-E(i,j)}{\max(E[i',j'])}}$$

Where *E(i,j)* denotes the allelic evolutionary coupling between spot *i* and *j* and *max(E[i', j'])* indicates the maximum value across all evolutionary couplings. Clusters identified via hierarchical clustering of the normalised allelic evolutionary coupling matrix were used as registered Tumour IDs in **Fig. 4b**.

Detection of metastasis-initiating subclones

To detect metastasis-initiating subclones in primary tumours, we created a shared character matrix between all lung sections profiled with 1cm x 1cm Curio arrays and Slide-seq samples of metastases. We filtered out spots that did not have at least 2 UMIs intBC-alleles that were not supported by at least 2 UMIs. We further filtered out spots that had fewer than 20% of their target-sites cut and more than 70% missingness. For computational reasons, we did not allow ambiguous alleles (taking only the most frequent allele per intBC in a spot) as the distance calculation is memory- and time-intensive. We then computed a shared metastatic parental allele state by taking states that were shared amongst 60% of spots in metastases profiled with Slide-seq. From this parental state, we computed the modified allelic distance (normalised by the number of shared characters) to all spots in the lung sample. We performed a similar analysis in paired Slide-tags data, computing the normalised modified allelic distances from all nuclei to the metastatic parental allele state.

Differential expression across metastatic cascade

We identified gene expression changes across niches associated with the metastatic cascade by employing the distances computed in the section above entitled “Detection of metastasis-initiating subclones”. We identified the metastasis-originating subclone as localizing to T2, so T1, T3 and T4 were determined to be Primary tumours without any relationship to the metastases. Focusing on T2, we further segmented it into a metastasis-initiating subclone (T2-Met) and other subclones (T2-NonMet). Specifically, we assigned cells to a metastatic subclone if their normalised modified allelic distance was less than 0.8. Then, using these assignments, we performed watershed segmentation with a custom procedure. Specifically, we binned signal into

1480 bins of 100 adjacent spots, applied a Gaussian filter with a sigma of 1.5 (with the Python package
1481 *skimage*) and then applied an Otsu threshold and dilation. We then applied an exact distance
1482 transform with *scipy.ndimage.distance_transform_edt* and computed a Watershed mask over
1483 peaks identified with *skimage.feature.peak_local_max* with a goal of identifying one tumour. This
1484 segmented subclone was labeled as T2-Met, and the remainder of the tumour was called T2-
1485 NonMet. We then performed differential expression across the library-size-normalised, logged
1486 counts of four groups (Primary tumours without metastatic relationship; T2-Met; T2-NonMet; and
1487 metastases) using a t-test implemented in Scanpy's[99] *rank_genes_groups* and reported the log2-
1488 fold-change in **Fig. 4g.**

1489 Signature scores for TGF β signalling were computed using MSigDB's
1490 "HALLMARK_TGF_BETA_SIGNALING" signature[114]. Signature scores for collagen were
1491 computed for a custom gene set consisting of *Acta2, Col1a1, Col2a1, Col3a1, Col5a1,* and
1492 *Col12a1*. Significance was computed using a one-sided *t*-test assessing if signature scores were
1493 higher in the metastatic tumour as compared to the primary tumour.

1494

1495 **Differential cell type abundance in metastatic neighbourhoods**

1496 Similar to analyses stratifying Slide-tags cells into neighbourhoods of high- and low-fitness
1497 cells, we stratified cells into neighbourhoods of cells closely related to metastases. As with
1498 determining cells related to metastases in Slide-seq data, we computed the distance to the
1499 parental metastatic allele and assigned cells with distances smaller than 0.8 as related to
1500 metastases. Then, we reconstructed spatial neighbourhoods of the closest 20 cells and quantified
1501 cell type enrichments based on the frequencies of cell types in these neighbourhoods and the
1502 overall frequency in a Slide-tags array.

1503

1504 **Analysis of transcriptional signatures in metastatic tumours**

1505 To assess the transcriptional signatures of metastasis, we explored three additional
1506 datasets: (1) scRNA-seq from metastatic families (i.e., primary seeding tumour and related
1507 metastases) from our previous KP-Tracer study[50]; (2) bulk RNA-seq from several KP tumours at
1508 different stages, including early stage, non-seeding primary tumours, seeding primary tumours,
1509 and metastatic tumors[65]; and (3) single-cell RNA-seq from primary lung adenocarcinoma (LUAD)
1510 tumours and metastatic brain tumours from the Pan-cancer human Brain Metastases Atlas
1511 (PBMA)[83].

1512 In the re-analysis of KP-Tracer metastasis families[50], we focused on the two families from
1513 the sgNT genotype (3724_NT_T1 and 3513_NT_T1). 3724_NT_T1 had 4 related metastases: 3

from the liver and 1 in soft tissue; 3513_NT_T1 had two related metastases: one in the kidney and one in lymph tissue. Data was pre-processed with Scanpy and we performed analysis on count-normalized (1M), logged, and scaled data. Signature gene sets were obtained from the Hallmark set in MSigDB[114].

In the bulk analysis of KP tumors[65], we obtained gene expression data from the original publication in Supplementary Table 1 and present gene expression for a selection of genes in **Extended Data Figure 10a**.

For the analysis of the PBMA study, we subset the data for an analysis of treatment-naïve LUAD tumours (n=22) and brain metastases (n=36; a total of 54 tumours). Data was pre-processed with Scanpy and we performed analysis on count-normalized (1M), logged, and scaled data. Signature scores for TGFb signalling and Hypoxia were computed using MSigDB's Hallmark gene signature set[114]. Signature scores for collagen were computed for a custom gene set consisting of *ACTA2, COL1A1, COL1A2, COL3A1, COL5A1, COL12A1.*

REFERENCES

1. Nowell, P. C. The clonal evolution of tumor cell populations. *Science* **194**, 23–28 (1976).
2. Vogelstein, B. *et al.* Cancer genome landscapes. *Science* **339**, 1546–1558 (2013).
3. Binnewies, M. *et al.* Understanding the tumor immune microenvironment (TIME) for effective therapy. *Nat. Med.* **24**, 541–550 (2018).
4. de Visser, K. E. & Joyce, J. A. The evolving tumor microenvironment: From cancer initiation to metastatic outgrowth. *Cancer Cell* **41**, 374–403 (2023).
5. Northey, J. J., Przybyla, L. & Weaver, V. M. Tissue force programs cell fate and tumor aggression. *Cancer Discov.* **7**, 1224–1237 (2017).
6. Noble, R. *et al.* Spatial structure governs the mode of tumour evolution. *Nat. Ecol. Evol.* **6**, 207–217 (2021).
7. Derynck, R., Turley, S. J. & Akhurst, R. J. TGFβ biology in cancer progression and immunotherapy. *Nat. Rev. Clin. Oncol.* **18**, 9–34 (2021).
8. Fang, J. S., Gillies, R. D. & Gatenby, R. A. Adaptation to hypoxia and acidosis in carcinogenesis and tumor progression. *Semin. Cancer Biol.* **18**, 330–337 (2008).
9. Carmona-Fontaine, C. *et al.* Emergence of spatial structure in the tumor microenvironment due to the Warburg effect. *Proc. Natl. Acad. Sci. U. S. A.* **110**, 19402–19407 (2013).
10. Houlahan, K. E. *et al.* Germline-mediated immunoediting sculpts breast cancer subtypes and metastatic proclivity. *Science* **384**, (2024).

1547 11. McAllister, S. S. & Weinberg, R. A. The tumour-induced systemic environment as a critical
1548 regulator of cancer progression and metastasis. *Nat. Cell Biol.* **16**, 717–727 (2014).
1549 12. Schwartz, R. & Schäffer, A. A. The evolution of tumour phylogenetics: principles and practice.
1550 *Nat. Rev. Genet.* **18**, 213–229 (2017).
1551 13. Jones, M. G., Yang, D. & Weissman, J. S. New tools for lineage tracing in cancer in vivo.
1552 *Annu. Rev. Cancer Biol.* **7**, (2023).
1553 14. McGranahan, N. & Swanton, C. Clonal Heterogeneity and Tumor Evolution: Past, Present,
1554 and the Future. *Cell* **168**, 613–628 (2017).
1555 15. Davis, A., Gao, R. & Navin, N. Tumor evolution: Linear, branching, neutral or punctuated?
1556 *Biochim. Biophys. Acta Rev. Cancer* **1867**, 151–161 (2017).
1557 16. Hu, Z. & Curtis, C. Inferring tumor phylogenies from multi-region sequencing. *Cell Syst.* **3**,
1558 12–14 (2016).
1559 17. Jones, S. *et al.* Comparative lesion sequencing provides insights into tumor evolution. *Proc.*
1560 *Natl. Acad. Sci. U. S. A.* **105**, 4283–4288 (2008).
1561 18. Gerlinger, M. *et al.* Intratumor heterogeneity and branched evolution revealed by multiregion
1562 sequencing. *N. Engl. J. Med.* **366**, 883–892 (2012).
1563 19. Jamal-Hanjani, M. *et al.* Tracking the evolution of non–small-cell lung cancer. *N. Engl. J. Med.*
1564 **376**, 2109–2121 (2017).
1565 20. Schwarz, R. F. *et al.* Spatial and temporal heterogeneity in high-grade serous ovarian cancer:
1566 A phylogenetic analysis. *PLoS Med.* **12**, e1001789 (2015).
1567 21. Sottoriva, A. *et al.* A Big Bang model of human colorectal tumor growth. *Nat. Genet.* **47**, 209–
1568 216 (2015).
1569 22. Zhao, Y. *et al.* Selection of metastasis competent subclones in the tumour interior. *Nat. Ecol.*
1570 *Evol.* **5**, 1033–1045 (2021).
1571 23. Turajlic, S. *et al.* Tracking cancer evolution reveals constrained routes to metastases:
1572 TRACERx renal. *Cell* **173**, 581-594.e12 (2018).
1573 24. Navin, N. *et al.* Tumour evolution inferred by single-cell sequencing. *Nature* **472**, 90–94
1574 (2011).
1575 25. Zhao, T. *et al.* Spatial genomics enables multi-modal study of clonal heterogeneity in tissues.
1576 *Nature* **601**, 85–91 (2022).
1577 26. Erickson, A. *et al.* Spatially resolved clonal copy number alterations in benign and malignant
1578 tissue. *Nature* **608**, 360–367 (2022).
1579 27. Lomakin, A. *et al.* Spatial genomics maps the structure, nature and evolution of cancer
1580 clones. *Nature* **611**, 594–602 (2022).

1581 28. Household, J. *et al.* Phenotypic plasticity and genetic control in colorectal cancer evolution.
1582 *Nature* **611**, 744–753 (2022).
1583 29. Heiser, C. N. *et al.* Molecular cartography uncovers evolutionary and microenvironmental
1584 dynamics in sporadic colorectal tumors. *Cell* **186**, 5620-5637.e16 (2023).
1585 30. Frieda, K. L. *et al.* Synthetic recording and in situ readout of lineage information in single
1586 cells. *Nature* **541**, 107–111 (2017).
1587 31. Chow, K.-H. K. *et al.* Imaging cell lineage with a synthetic digital recording system. *Science*
1588 **372**, (2021).
1589 32. Chan, M. M. *et al.* Molecular recording of mammalian embryogenesis. *Nature* **570**, 77–82
1590 (2019).
1591 33. McKenna, A. *et al.* Whole-organism lineage tracing by combinatorial and cumulative genome
1592 editing. *Science* **353**, aaf7907 (2016).
1593 34. Spanjaard, B. *et al.* Simultaneous lineage tracing and cell-type identification using CRISPR–
1594 Cas9-induced genetic scars. *Nat. Biotechnol.* **36**, 469–473 (2018).
1595 35. He, Z. *et al.* Lineage recording in human cerebral organoids. *Nat. Methods* **19**, 90–99 (2022).
1596 36. Choi, J. *et al.* A time-resolved, multi-symbol molecular recorder via sequential genome
1597 editing. *Nature* **608**, 98–107 (2022).
1598 37. Hwang, B. *et al.* Lineage tracing using a Cas9-deaminase barcoding system targeting
1599 endogenous L1 elements. *Nat. Commun.* **10**, 1–9 (2019).
1600 38. Alemany, A., Florescu, M., Baron, C. S., Peterson-Maduro, J. & van Oudenaarden, A. Whole-
1601 organism clone tracing using single-cell sequencing. *Nature* **556**, 108–112 (2018).
1602 39. Kalhor, R., Mali, P. & Church, G. M. Rapidly evolving homing CRISPR barcodes. *Nat.*
1603 *Methods* **14**, 195–200 (2017).
1604 40. Li, L. *et al.* A mouse model with high clonal barcode diversity for joint lineage, transcriptomic,
1605 and epigenomic profiling in single cells. *Cell* **186**, 5183-5199.e22 (2023).
1606 41. Jones, M. G. *et al.* Inference of single-cell phylogenies from lineage tracing data using
1607 Cassiopeia. *Genome Biol.* **21**, 92 (2020).
1608 42. Sashittal, P., Schmidt, H., Chan, M. & Raphael, B. J. Startle: A star homoplasy approach for
1609 CRISPR-Cas9 lineage tracing. *Cell Syst.* **14**, 1113-1121.e9 (2023).
1610 43. Fang, W. *et al.* Quantitative fate mapping: A general framework for analyzing progenitor state
1611 dynamics via retrospective lineage barcoding. *Cell* **185**, 4604-4620.e32 (2022).
1612 44. Gong, W. *et al.* Benchmarked approaches for reconstruction of in vitro cell lineages and in
1613 silico models of C. elegans and M. musculus developmental trees. *Cell Syst* **12**, 810-826.e4
1614 (2021).

1615 45. Pan, X., Li, H., Putta, P. & Zhang, X. LinRace: cell division history reconstruction of single
1616 cells using paired lineage barcode and gene expression data. *Nat. Commun.* **14**, 1–15 (2023).
1617 46. Schiffman, J. S. *et al.* Defining heritability, plasticity, and transition dynamics of cellular
1618 phenotypes in somatic evolution. *Nat. Genet.* 1–11 (2024).
1619 47. Quinn, J. J. *et al.* Single-cell lineages reveal the rates, routes, and drivers of metastasis in
1620 cancer xenografts. *Science* **371**, (2021).
1621 48. Simeonov, K. P. *et al.* Single-cell lineage tracing of metastatic cancer reveals selection of
1622 hybrid EMT states. *Cancer Cell* (2021) doi:10.1016/j.ccell.2021.05.005.
1623 49. Zhang, W. *et al.* The bone microenvironment invigorates metastatic seeds for further
1624 dissemination. *Cell* **184**, 2471-2486.e20 (2021).
1625 50. Yang, D. *et al.* Lineage tracing reveals the phylodynamics, plasticity, and paths of tumor
1626 evolution. *Cell* (2022) doi:10.1016/j.cell.2022.04.015.
1627 51. Jackson, E. L. *et al.* Analysis of lung tumor initiation and progression using conditional
1628 expression of oncogenic K-ras. *Genes Dev.* **15**, 3243–3248 (2001).
1629 52. Jackson, E. L. *et al.* The differential effects of mutant p53 alleles on advanced murine lung
1630 cancer. *Cancer Res.* **65**, 10280–10288 (2005).
1631 53. Winslow, M. M. *et al.* Suppression of lung adenocarcinoma progression by Nkx2-1. *Nature*
1632 **473**, 101–104 (2011).
1633 54. LaFave, L. M. *et al.* Epigenomic State Transitions Characterize Tumor Progression in Mouse
1634 Lung Adenocarcinoma. *Cancer Cell* **38**, 212-228.e13 (2020).
1635 55. Marjanovic, N. D. *et al.* Emergence of a High-Plasticity Cell State during Lung Cancer
1636 Evolution. *Cancer Cell* **38**, 229-246.e13 (2020).
1637 56. Stickels, R. R. *et al.* Highly sensitive spatial transcriptomics at near-cellular resolution with
1638 Slide-seqV2. *Nat. Biotechnol.* **39**, 313–319 (2021).
1639 57. Rodriques, S. G. *et al.* Slide-seq: A scalable technology for measuring genome-wide
1640 expression at high spatial resolution. *Science* **363**, 1463–1467 (2019).
1641 58. Russell, A. J. C. *et al.* Slide-tags enables single-nucleus barcoding for multimodal spatial
1642 genomics. *Nature* **625**, 101–109 (2024).
1643 59. Ståhl, P. L. *et al.* Visualization and analysis of gene expression in tissue sections by spatial
1644 transcriptomics. *Science* **353**, 78–82 (2016).
1645 60. Liu, Y. *et al.* High-spatial-resolution multi-omics sequencing via deterministic barcoding in
1646 tissue. *Cell* **183**, 1665-1681.e18 (2020).
1647 61. Sutherland, K. D. *et al.* Multiple cells-of-origin of mutant K-Ras-induced mouse lung
1648 adenocarcinoma. *Proc. Natl. Acad. Sci. U. S. A.* **111**, 4952–4957 (2014).

1649 62. Arlauckas, S. P. *et al.* Arg1 expression defines immunosuppressive subsets of tumor-
1650 associated macrophages. *Theranostics* **8**, 5842–5854 (2018).
1651 63. Saitou, N. & Nei, M. The neighbor-joining method: a new method for reconstructing
1652 phylogenetic trees. *Mol. Biol. Evol.* **4**, 406–425 (1987).
1653 64. You, Y. *et al.* Systematic comparison of sequencing-based spatial transcriptomic methods.
1654 *Nat. Methods* (2024) doi:10.1038/s41592-024-02325-3.
1655 65. Chuang, C.-H. *et al.* Molecular definition of a metastatic lung cancer state reveals a targetable
1656 CD109-Janus kinase-Stat axis. *Nat. Med.* **23**, 291–300 (2017).
1657 66. Lee, J. Y. *et al.* Senescent fibroblasts in the tumor stroma rewire lung cancer metabolism and
1658 plasticity. *bioRxivorg* (2024) doi:10.1101/2024.07.29.605645.
1659 67. Bill, R. *et al.* CXCL9:SPP1 macrophage polarity identifies a network of cellular programs that
1660 control human cancers. *Science* **381**, 515–524 (2023).
1661 68. Jones, M. G., Rosen, Y. & Yosef, N. Interactive, integrated analysis of single-cell
1662 transcriptomic and phylogenetic data with PhyloVision. *Cell Rep Methods* **2**, 100200 (2022).
1663 69. Lewinsohn, M. A., Bedford, T., Müller, N. F. & Feder, A. F. State-dependent evolutionary
1664 models reveal modes of solid tumour growth. *Nat. Ecol. Evol.* **7**, 581–596 (2023).
1665 70. Moran, P. A. P. Notes on continuous stochastic phenomena. *Biometrika* **37**, 17–23 (1950).
1666 71. Hayashi, M. *et al.* Induction of glucose transporter 1 expression through hypoxia-inducible
1667 factor 1alpha under hypoxic conditions in trophoblast-derived cells. *J. Endocrinol.* **183**, 145–154
1668 (2004).
1669 72. Zhang, J. Z., Behrooz, A. & Ismail-Beigi, F. Regulation of glucose transport by hypoxia. *Am.*
1670 *J. Kidney Dis.* **34**, 189–202 (1999).
1671 73. McEarchern, J. A. *et al.* Invasion and metastasis of a mammary tumor involves TGF-beta
1672 signaling. *Int. J. Cancer* **91**, 76–82 (2001).
1673 74. Kakani, P. *et al.* Hypoxia-induced CTCF promotes EMT in breast cancer. *Cell Rep.* **43**,
1674 114367 (2024).
1675 75. Zhang, L. *et al.* Hypoxia induces epithelial-mesenchymal transition via activation of SNAI1
1676 by hypoxia-inducible factor -1α in hepatocellular carcinoma. *BMC Cancer* **13**, 108 (2013).
1677 76. Rankin, E. B. & Giaccia, A. J. Hypoxic control of metastasis. *Science* **352**, 175–180 (2016).
1678 77. Choi, J. *et al.* Inflammatory signals induce AT2 cell-derived damage-associated transient
1679 progenitors that mediate alveolar regeneration. *Cell Stem Cell* **27**, 366-382.e7 (2020).
1680 78. Quail, D. F. & Joyce, J. A. Microenvironmental regulation of tumor progression and
1681 metastasis. *Nat. Med.* **19**, 1423–1437 (2013).

1682 79. Lee, J. H. *et al.* TGF-β and RAS jointly unmask primed enhancers to drive metastasis. *Cell*
1683 (2024) doi:10.1016/j.cell.2024.08.014.
1684 80. McGinnis, C. S. *et al.* The temporal progression of lung immune remodeling during breast
1685 cancer metastasis. *Cancer Cell* **42**, 1018-1031.e6 (2024).
1686 81. Gong, Z. *et al.* Lung fibroblasts facilitate pre-metastatic niche formation by remodeling the
1687 local immune microenvironment. *Immunity* **55**, 1483-1500.e9 (2022).
1688 82. Kaczanowska, S. *et al.* Genetically engineered myeloid cells rebalance the core immune
1689 suppression program in metastasis. *Cell* **184**, 2033-2052.e21 (2021).
1690 83. Xing, X. *et al.* Pan-cancer human brain metastases atlas at single-cell resolution. *Cancer Cell*
1691 **43**, 1242-1260.e9 (2025).
1692 84. Murdoch, C., Muthana, M. & Lewis, C. E. Hypoxia regulates macrophage functions in
1693 inflammation. *J. Immunol.* **175**, 6257–6263 (2005).
1694 85. Kugeratski, F. G. *et al.* Hypoxic cancer-associated fibroblasts increase NCBP2-AS2/HIAR to
1695 promote endothelial sprouting through enhanced VEGF signaling. *Sci. Signal.* **12**, eaan8247
1696 (2019).
1697 86. Corzo, C. A. *et al.* HIF-1α regulates function and differentiation of myeloid-derived suppressor
1698 cells in the tumor microenvironment. *J. Exp. Med.* **207**, 2439–2453 (2010).
1699 87. Korbecki, J. *et al.* Hypoxia alters the expression of CC chemokines and CC chemokine
1700 receptors in a tumor-A literature review. *Int. J. Mol. Sci.* **21**, 5647 (2020).
1701 88. Chaturvedi, P., Gilkes, D. M., Takano, N. & Semenza, G. L. Hypoxia-inducible factor-
1702 dependent signaling between triple-negative breast cancer cells and mesenchymal stem cells
1703 promotes macrophage recruitment. *Proc. Natl. Acad. Sci. U. S. A.* **111**, E2120-9 (2014).
1704 89. Enfield, K. S. S. *et al.* Spatial architecture of myeloid and T cells orchestrates immune evasion
1705 and clinical outcome in lung cancer. *Cancer Discov.* **14**, 1018–1047 (2024).
1706 90. Greenwald, A. C. *et al.* Integrative spatial analysis reveals a multi-layered organization of
1707 glioblastoma. *Cell* **187**, 2485-2501.e26 (2024).
1708 91. Zhao, W. *et al.* A cellular and spatial atlas of TP53 -associated tissue remodeling in lung
1709 adenocarcinoma. *bioRxivorg* (2024) doi:10.1101/2023.06.28.546977.
1710 92. Burdziak, C. *et al.* Epigenetic plasticity cooperates with cell-cell interactions to direct
1711 pancreatic tumorigenesis. *Science* **380**, eadd5327 (2023).
1712 93. Adrover, J. M. *et al.* Neutrophils drive vascular occlusion, tumour necrosis and metastasis.
1713 *Nature* (2025) doi:10.1038/s41586-025-09278-3.
1714 94. França, G. S. *et al.* Cellular adaptation to cancer therapy along a resistance continuum.
1715 *Nature* **631**, 876–883 (2024).

95. Chen, W. *et al.* Symbolic recording of signalling and cis-regulatory element activity to DNA. *Nature* **632**, 1073–1081 (2024).
96. Kempton, H. R., Love, K. S., Guo, L. Y. & Qi, L. S. Scalable biological signal recording in mammalian cells using Cas12a base editors. *Nat. Chem. Biol.* **18**, 742–750 (2022).
97. Melsted, P. *et al.* Modular, efficient and constant-memory single-cell RNA-seq preprocessing. *Nat. Biotechnol.* **39**, 813–818 (2021).
98. Fleming, S. J. *et al.* Unsupervised removal of systematic background noise from droplet-based single-cell experiments using CellBender. *Nat. Methods* **20**, 1323–1335 (2023).
99. Wolf, F. A., Angerer, P. & Theis, F. J. SCANPY: large-scale single-cell gene expression data analysis. *Genome Biol.* **19**, 15 (2018).
100. Martin, M. Cutadapt removes adapter sequences from high-throughput sequencing reads. *EMBnet J.* **17**, 10 (2011).
101. *Density-Based Algorithm for Discovering Clusters in Large Spatial Databases with Noise*.
102. Gusfield, D. Efficient algorithms for inferring evolutionary trees. *Networks (N. Y.)* **21**, 19–28 (1991).
103. Xu, C. *et al.* Probabilistic harmonization and annotation of single-cell transcriptomics data with deep generative models. *Mol. Syst. Biol.* **17**, e9620 (2021).
104. Lopez, R., Regier, J., Cole, M. B., Jordan, M. I. & Yosef, N. Deep generative modeling for single-cell transcriptomics. *Nat. Methods* **15**, 1053–1058 (2018).
105. Gayoso, A. *et al.* scvi-tools: a library for deep probabilistic analysis of single-cell omics data. *bioRxiv* 2021.04.28.441833 (2021) doi:10.1101/2021.04.28.441833.
106. Traag, V. A., Waltman, L. & van Eck, N. J. From Louvain to Leiden: guaranteeing well-connected communities. *Sci. Rep.* **9**, 5233 (2019).
107. DeTomaso, D. & Yosef, N. Hotspot identifies informative gene modules across modalities of single-cell genomics. *Cell Syst* **12**, 446-456.e9 (2021).
108. Marconato, L. *et al.* SpatialData: an open and universal data framework for spatial omics. *Nat. Methods* 1–5 (2024).
109. Neher, R. A., Russell, C. A. & Shraiman, B. I. Predicting evolution from the shape of genealogical trees. *Elife* **3**, (2014).
110. Prillo, S., Ravoor, A., Yosef, N. & Song, Y. S. ConvexML: Scalable and accurate inference of single-cell chronograms from CRISPR/Cas9 lineage tracing data. *bioRxivorg* (2023) doi:10.1101/2023.12.03.569785.
111. Fang, Z., Liu, X. & Peltz, G. GSEApy: a comprehensive package for performing gene set enrichment analysis in Python. *Bioinformatics* **39**, btac757 (2023).

1750 112. Jin, S., Plikus, M. V. & Nie, Q. CellChat for systematic analysis of cell-cell communication
1751 from single-cell transcriptomics. *Nat. Protoc.* **20**, 180–219 (2025).
1752 113. Dai, M., Pei, X. & Wang, X.-J. Accurate and fast cell marker gene identification with COSG.
1753 *Brief. Bioinform.* **23**, (2022).
1754 114. Subramanian, A. *et al.* Gene set enrichment analysis: a knowledge-based approach for
1755 interpreting genome-wide expression profiles. *Proc. Natl. Acad. Sci. U. S. A.* **102**, 15545–15550
1756 (2005).

MAIN FIGURES

Jones*, Sun* *et al.* **Figure 1**

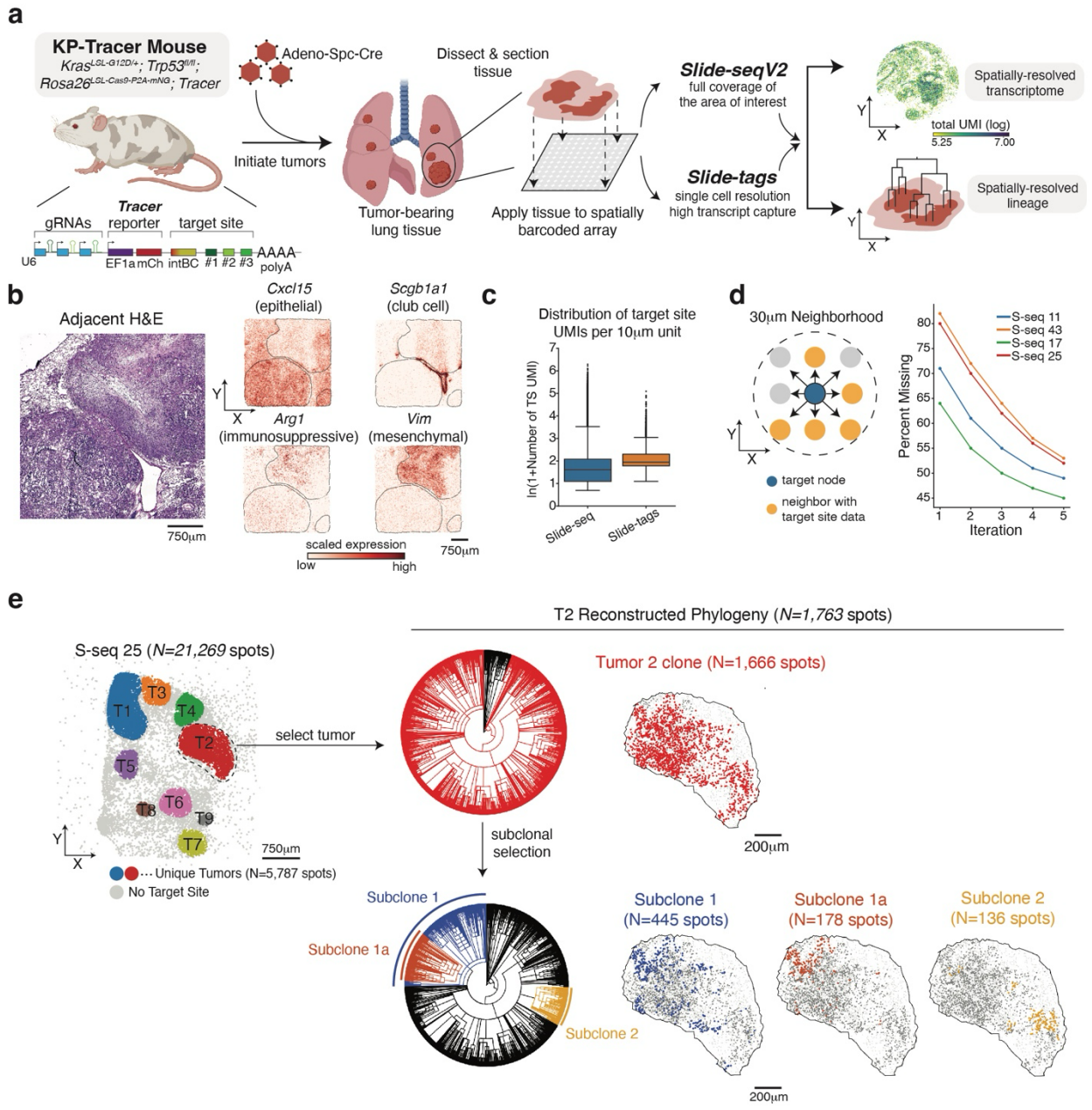

Figure 1. An integrated lineage and spatial platform enables high-resolution analysis of tumour evolution *in vivo*.

(a) Schematic of experimental workflow for integrated, spatially resolved lineage and cell state analysis. In KP-tracer mice, oncogenic *Kras*$^{G12D/+}$;*Trp53*$^{-/-}$ mutations and Cas9-based lineage tracing were simultaneously activated upon administration of adenovirus carrying SPC promoter-driven Cre recombinase. After 12-16 weeks, mice were sacrificed, and cryopreserved tumour-bearing lungs were sectioned for spatial profiling with Slide-seq and Slide-tags technologies. Libraries were prepared and sequenced to study spatially resolved lineages and transcriptional patterns. S-seq 30 is used as a representative example for total UMI capture in a spatial array. Biorender was used to create parts of this schematic.

(b) Representative H&E staining and spatially resolved gene expression data for a lung section carrying three tumours (black line). Log-normalised, scaled counts for epithelial-like (*Cxcl15* and *Scgb1a1*), immunosuppressive myeloid (*Arg1*), and mesenchymal cells (*Vim*) are shown.

(c) Distribution of the number of target-site UMIs for Slide-seq and Slide-tags data. Ln(1+x) counts are shown. Boxplots show the quartiles of the distribution, and whiskers extend to 1.5x the interquartile range.

(d) Schematic of spatial imputation of lineage-tracing data in 30μm neighbourhoods (left) and representative examples of missingness left after each of 5 iterations of spatial imputation.

(e) Representative spatially resolved lineages in spatial array S-seq 25 profiling a lung section carrying 9 distinct tumours. Reconstructed lineages are displayed for a representative tumour, T2. Successive nested subclones displaying both shared and distinct lineage states in unique colors are indicated on the phylogenetic tree and mapped spatially. Lineages marked in black spots not included in the designated subclone. Overall, spots that are more related in lineage tend to be spatially coherent.

Jones*, Sun* *et al.* **Figure 2**

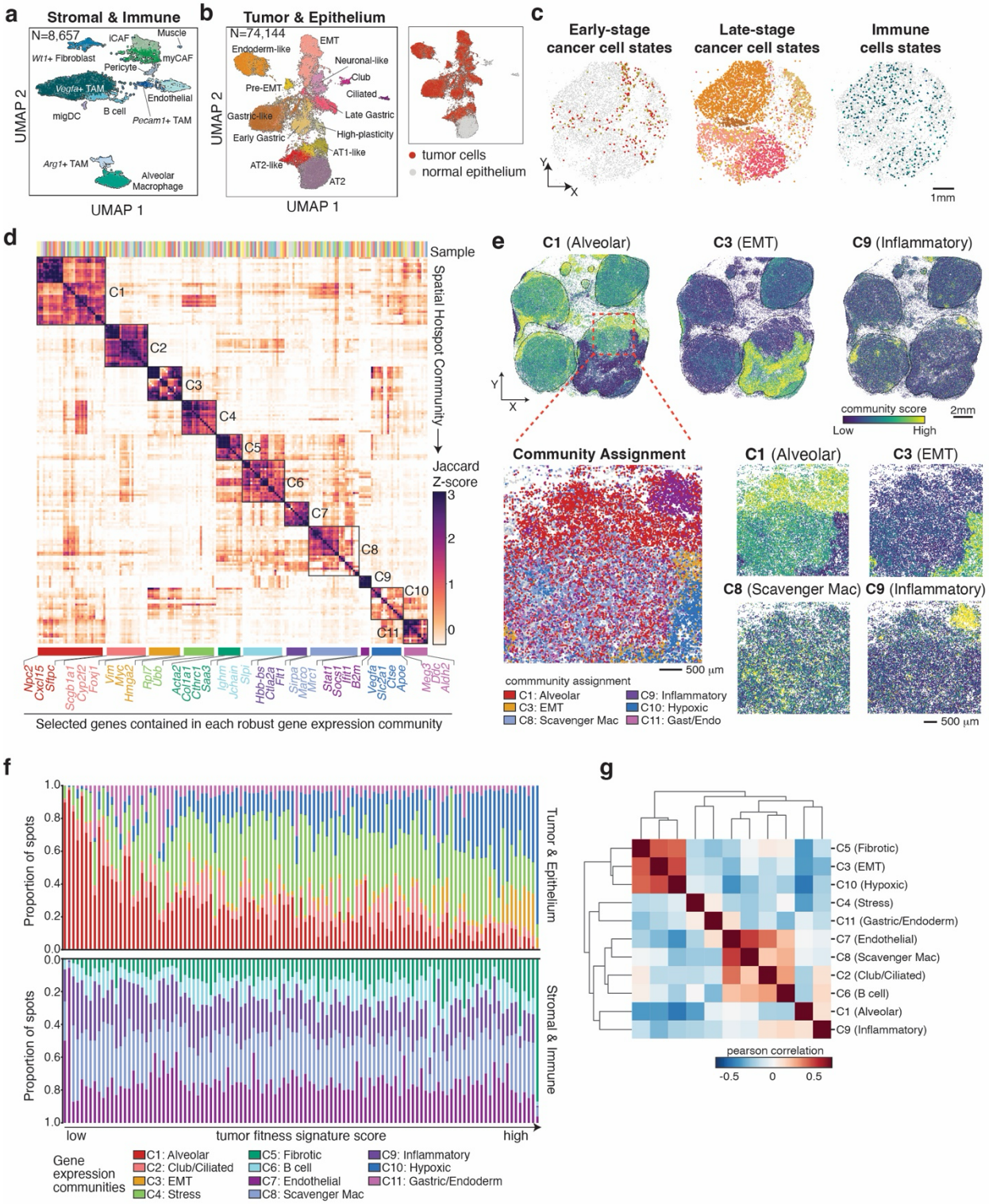

Figure 2. Diverse spatial gene expression communities emerge during KP-tracer tumour progression.

(a-b) UMAP projections of Slide-tags data on tumour bearing lungs from KP-Tracer mice, annotated by cell type. **(a)** Slide-tags data corresponding to all stromal and immune cell types: *Cd45*+ immune cells and other non-epithelial stromal cells. **(b)** Slide-tags data corresponding to all cancer and normal epithelial cells. Inset indicates where cancer cells are found in this projection.

(c) Representative spatial projections of early-stage and late-stage cancer cell states, and immune cell types from Slide-tags analysis of KP-Tracer tumour bearing lung (shown on S-tags 3). Colors correspond to those in UMAP projections in **(a-b)**.

(d) Heatmap of Z-scored Jaccard overlap between genes contained in spatial gene expression communities. Each row or column is a community, defined as a set of spatially autocorrelated genes identified with Hotspot, and robust spatial gene expression communities are determined by hierarchical clustering and indicated by annotated blocks. The Slide-seq sample from which a community is identified is indicated by unique colors on the top of the heatmap. Representative genes specific to each spatial community are highlighted at the bottom of the heatmap.

(e) Community scores of selected spatial communities projected onto a representative Slide-seq dataset of a tumour bearing lung with 4 major tumours (S-seq 43). Tumour boundaries are indicated with black lines (top). Zoom in of region showing community assignments and scores for a selection of communities (bottom).

(f) Proportion of gene expression community assignments across all KP lung tumours in the Slide-seq dataset, ordered by increasing fitness signature scores. Each bar indicates a single segmented tumour in the Slide-seq dataset. Top: communities that are more related to tumour or epithelial programs. Bottom: communities that are related to stromal and immune programs.

(g) Heatmap reporting Pearson correlation of community abundances across all tumours in the Slide-seq data.

Jones*, Sun* *et al.* **Figure 3**

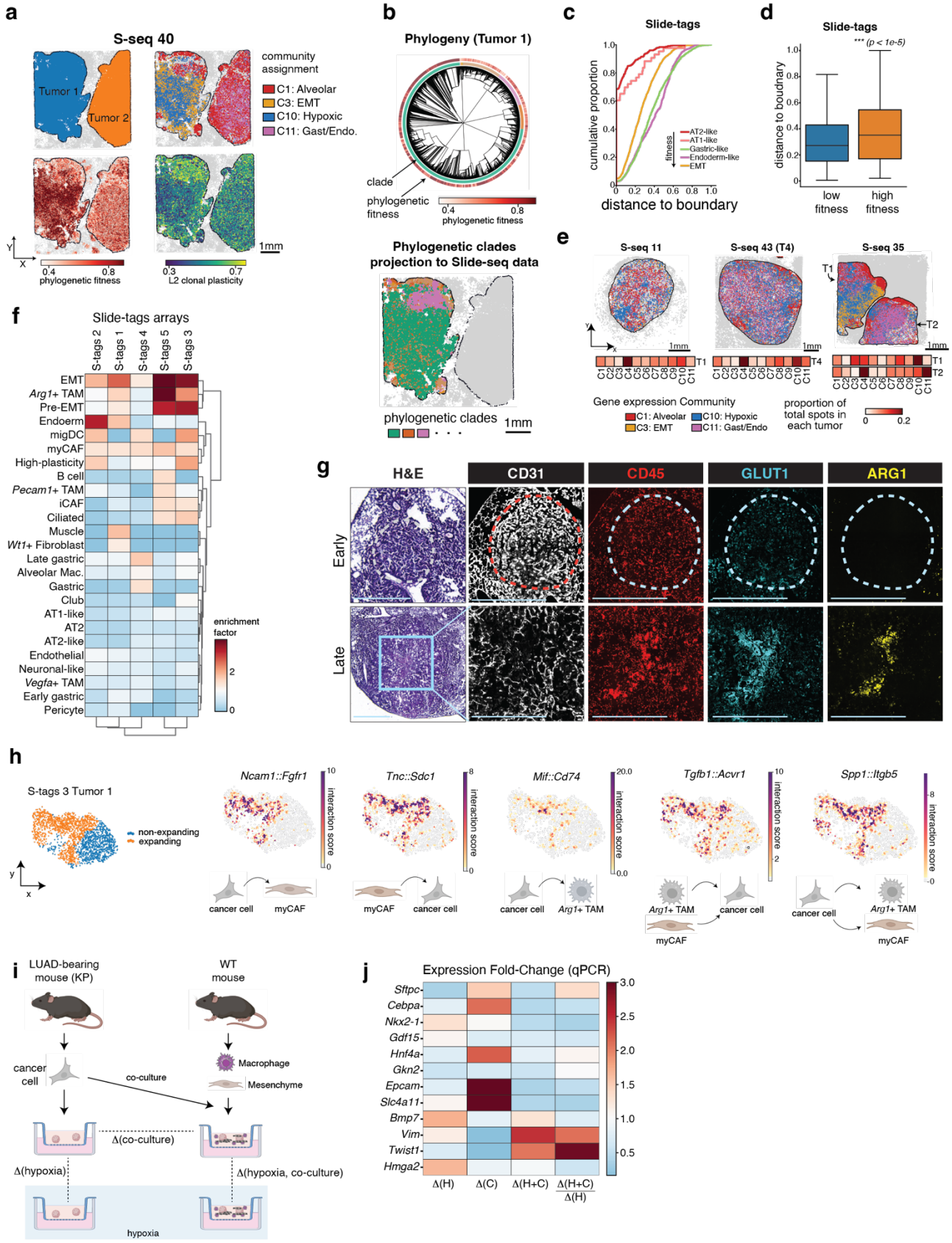

Figure 3. Subclonal expansions associate with microenvironmental remodelling towards a hypoxic, fibrotic, and immunosuppressive state.

(a) A representative Slide-seq array containing two tumours (S-seq 40) is shown with spatial projections of tumour annotations, selected gene expression community assignments, phylogenetic fitness, and L2 clonal plasticity.

(b) Reconstructed phylogeny and spatial localization of phylogenetic subclades for Tumour 1 from the representative Slide-seq dataset (S-seq 40) example shown in **(a)**. The phylogeny is annotated by subclonal clade assignment (inner colour track) and phylogenetic fitness (outer colour track).

(c) Cumulative density distributions for normalised Euclidean distance to nearest non-tumour cell (i.e., tumour boundary) for five selected major cancer cell states across all Slide-tags arrays. Cancer cells in high-fitness-associated cell states (e.g. EMT, Endoderm-like, Gastric-like) locate further away from the tumour boundary than those in low-fitness-associated states (AT2-like, AT1-like). Distance is normalised to unit scale (0-1).

(d) Distribution of normalised Euclidean distances to nearest non-tumour cell (i.e., tumour boundary) for high-fitness and low-fitness cells (defined here as having phylogenetic fitness greater than the 90th or less than the 10th percentiles, respectively). High-fitness cells are significantly further away from the tumour boundary ($p<1e-5$, wilcoxon rank-sums test). Boxplots show the quartiles of the distribution, and whiskers extend to 1.5x the interquartile range.

(e) Representative Slide-seq examples showing the evolution of the spatial gene expression communities following tumour progression (left to right). Selected community assignments are displayed, and full proportion of assignments are reported in 1D heatmaps under each spatial dataset.

(f) Clustered heatmap of enrichments of cell type abundances in spatial neighbourhoods of high- and low-fitness cells in 5 Slide-tags arrays. Values > 1 indicate that a cell type is more abundant (i.e., enriched) in neighbourhoods of cells with high fitness. Cell type names are identical to those reported in **Fig. 2a-b**.

(g) H&E and paired immunofluorescence staining of endothelial-cell marker CD31, immune cell marker CD45, hypoxia-reporter GLUT1, and immunosuppressive myeloid marker ARG1 in representative KP tumours. The interior of large, late-stage tumours is marked with a decrease of endothelial cells (CD31) and increases of hypoxia (GLUT1) and immunosuppressive myeloid cells (ARG1, CD45). Scale bars = 1mm.

(h) Representative examples of expansion-specific ligand-receptor interaction pairs. Interaction pair is indicated by (ligand::receptor) and cell types and directionality of interaction are indicated below by arrows and cell types. Values are interaction scores based on the expression of the ligand-receptor pair in the indicated spot.

(i-j) Co-culture of KP tumour organoids, alveolar macrophages, and lung mesenchyme in hypoxic conditions induce a stronger EMT response in cancer cells than hypoxia alone. (i) Experimental setup: cancer cells were sorted from KP tumours and alveolar macrophages and lung mesenchymal cells were sorted from normal mice. The 3D primary organoids were derived from cancer cells and were cultured individually or in co-culture in normal and hypoxic conditions. (j) Gene expression fold-changes across conditions, measured by qPCR. (H: Hypoxia; C: Co-culture)

Jones*, Sun* *et al.* **Figure 4**

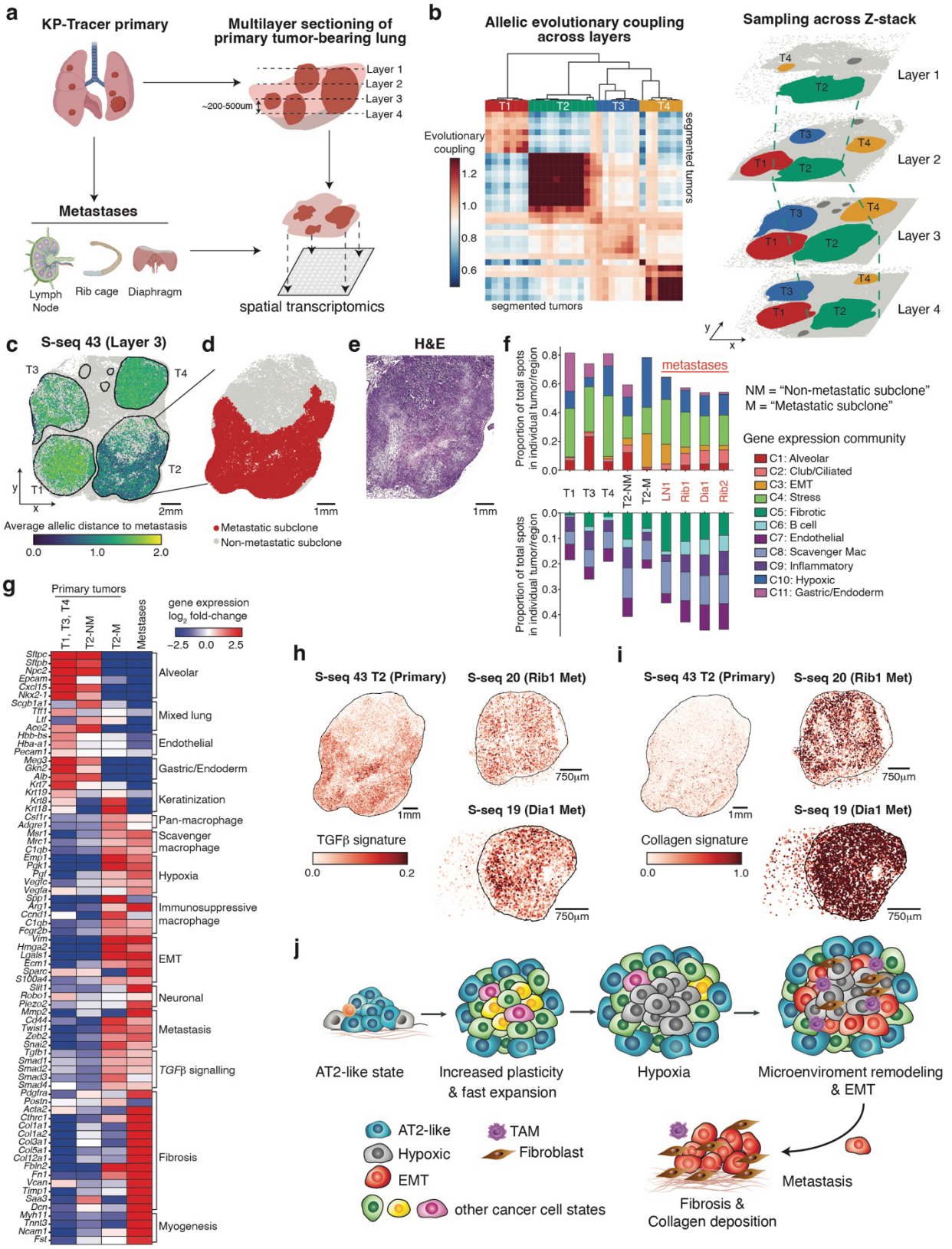

Figure 4. Tracing the evolution of subclonal niches across the metastatic cascade.

(a) Schematic of spatial transcriptomics workflow from a KP-Tracer mouse with large primary lung tumours and paired metastases from the lymph node, rib cage, and diaphragm. Multiple lung sections with four large primary tumours were harvested and subjected to both Slide-seq and Slide-tags assays. Biorender was used to create parts of this schematic.

(b) Coarse-grained alignment of Slide-seq spatial transcriptomics data (based on lineage-tracing edits) from four representative layers (Layer 1 – Layer 4) of a KP tumour bearing lung at approximately 200-500μm intervals from different z position. (Left) A clustered heatmap of allelic evolutionary coupling scores across all Slide-seq datasets from the tumour-bearing lung identifies the four major tumours. Each row or column is a single tumour from one Slide-seq dataset. (Right) 3D reconstruction of aligned datasets, annotated by one of four major tumours. Individual tumours are labelled in different colours.

(c) Representative spatial projection (S-seq 43) of allelic distances – summarizing how different lineage-tracing edits are between cells – for each spot with lineage-tracing data. Distance was computed to a consensus metastatic parental allele and normalised between 0 and 2.

(d-e) The metastasis-initiating subclone in T2 was segmented from cells with high relatedness to metastatic tumours and labelled in red. **(e)** H&E staining of T2.

(f) Proportion of gene expression community across representative stages of the metastatic cascade, including primary lung tumours (T1,3,4) without relatedness to metastases, the metastasis-initiating (M) and non-metastatic-initiating (NM) subclones in the primary tumour (T2) that gave rise to metastases, and four metastases. Top: communities that are more related to tumour or epithelial programs. Bottom: communities that are related to stromal/immune programs.

(g) Heatmap of gene expression log2-fold-changes between environmental niche (primary tumours without metastatic relationship, non-metastasis-initiating (NM) and metastasis-initiating (M) subclones within T2, and metastases). Genes are manually organized into ontologies.

(h-j) Spatial projection of gene expression scores of the Hallmark TGFβ and custom Collagen gene signatures on the metastasis-initiating primary tumour and selected metastases. Tumour 2 on S-seq 43 is used as the representative layer.

(j) A schematic model of KP tumour evolution and microenvironmental remodelling.

EXTENDED DATA FIGURES

Jones*, Sun* et al. **Extended Data Figure 1**

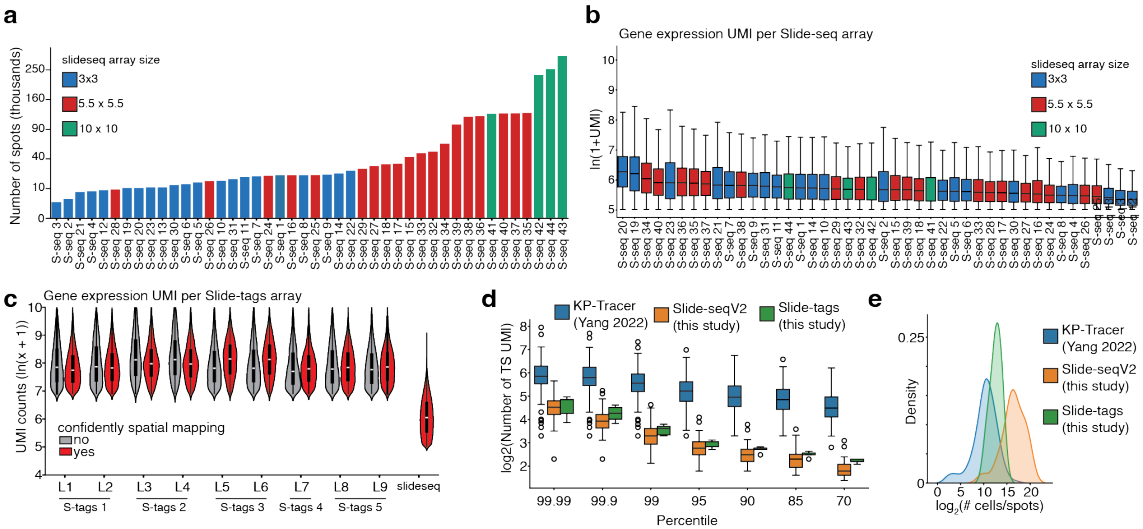

Extended Data Figure 1. Characterization of spatial-lineage platform.

(a) Number of spots that pass quality-control for all Slide-seq array. 3mm, 5mm, and 1cm arrays are uniquely coloured.

(b) Number of gene expression UMIs for each Slide-seq array. Ln(1+UMI) is reported for each dataset. 3mm, 5mm, and 1cm arrays are uniquely coloured. Boxplots show the quartiles of the distribution, and whiskers extend to 1.5x the interquartile range.

(c) Number of gene expression UMIs for each Slide-tags array, and one representative Slide-seq array. Each array is sequenced across multiple 10X libraries; assignment of 10X library to array is annotated. Distributions are split between cells that are confidently mapped and those that are not. Ln(1+UMI) is reported.

(d) Distribution of number of target-site UMIs marking the top *X* percentile for whole-cell (KP-Tracer), Slide-seq, or Slide-tags datasets. Ln(1+UMI) is reported. Boxplots show the quartiles of the distribution, and whiskers extend to 1.5x the interquartile range.

(e) Distribution of number of observations (cells or spots) that pass target-site quality-control in whole-cell (KP-Tracer), Slide-seq, or Slide-tags datasets. Log_2 of the number of observations is reported.

Jones*, Sun* et al. **Extended Data Figure 2**

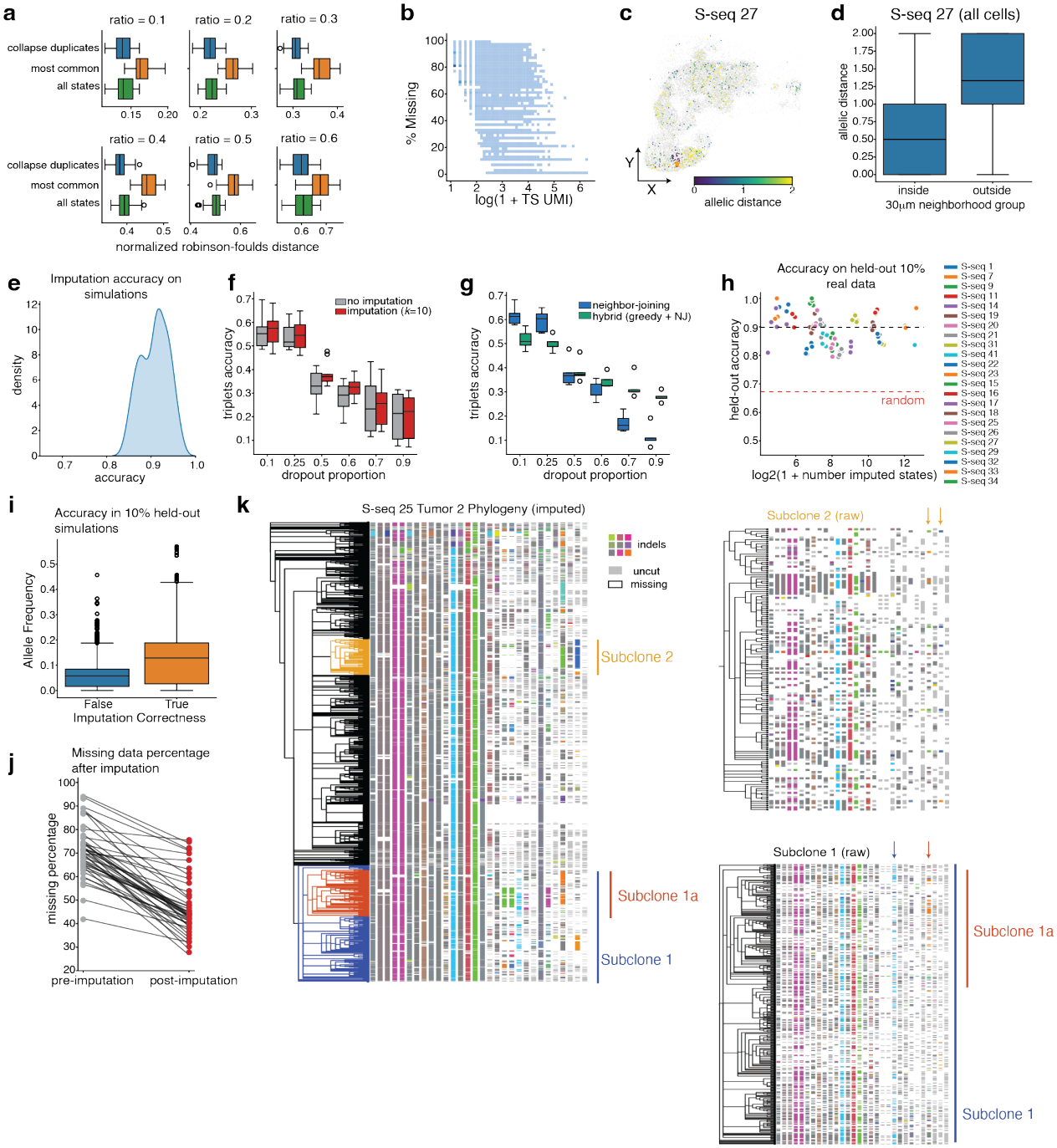

Extended Data Figure 2. **Benchmarking of computational approaches for spatial-lineage data.**

(a) Normalised Robinson-Foulds reconstruction error for simulated trees with increasing ratios of pooled cells and different pre-processing techniques. A ratio of *p* indicates that

simulated lineage-tracing data of *p*% of cells are combined into a single observation to simulate multiple-cell capture in spatial transcriptomics (**Methods**).

(b) Relationship between percentage of missing lineage-tracing data in a cell or spot and the log-number of UMIs (ln(1+x)) for Slide-seq and Slide-tags data.

(c) Representative example of spatial coherence of lineage-tracing data on S-seq 27. For a selected spot (shown as a star), normalised allelic distance is reported for all spots with confident lineage-tracing data. Allelic distance is normalised between 0 and 2.

(d) Distribution of allelic distances to spots within a 30μm neighbourhood of a spot versus outside this neighbourhood. Distribution over all spots in S-seq 27 is reported.

(e) Distribution of spatial imputation accuracy in lineage-tracing data simulated on a two-dimensional array.

(f) Triplets-correct accuracy of reconstructed phylogenies simulated on a spatial array for various amounts of missing data rates, with and without spatial imputation. Boxplots show the quartiles of the distribution, and whiskers extend to 1.5x the interquartile range.

(g) Triplets-correct accuracy of reconstructions with modified Neighbour-Joining and hybrid Cassiopeia-Greedy / Neighbour Joining algorithms for data simulated on a spatial array with various amounts of missing data, after spatial imputation.

(h) Accuracy of spatial imputation and number of imputed states after holding-out 10% of all lineage-tracing data in Slide-seq datasets. Datasets where at least 10 imputations are made are shown. Median accuracy of random predictions is reported in a red dashed line.

(i) Allele frequency of held-out data in a given tumour binned by imputation correctness. Boxplots show the quartiles of the distribution, and whiskers extend to 1.5x the interquartile range.

(j) Overview of missing data reduction across all Slide-seq datasets after five rounds of spatial-imputation.

(k) Phylogeny and lineage tracing heatmap of tree reconstructed in **Fig. 1e**. Subclones of interest are annotated in the same colours as in **Fig. 1e**. On the right, individual subclone heatmaps are presented with raw allelic data. Colour-coded arrows mark subclone-defining alleles. Unique colours of the heatmap indicate unique insertions or deletions (“indels”), white indicates missing data, and gray colours indicates no indel detected.

Jones*, Sun* et al. **Extended Data Figure 3**

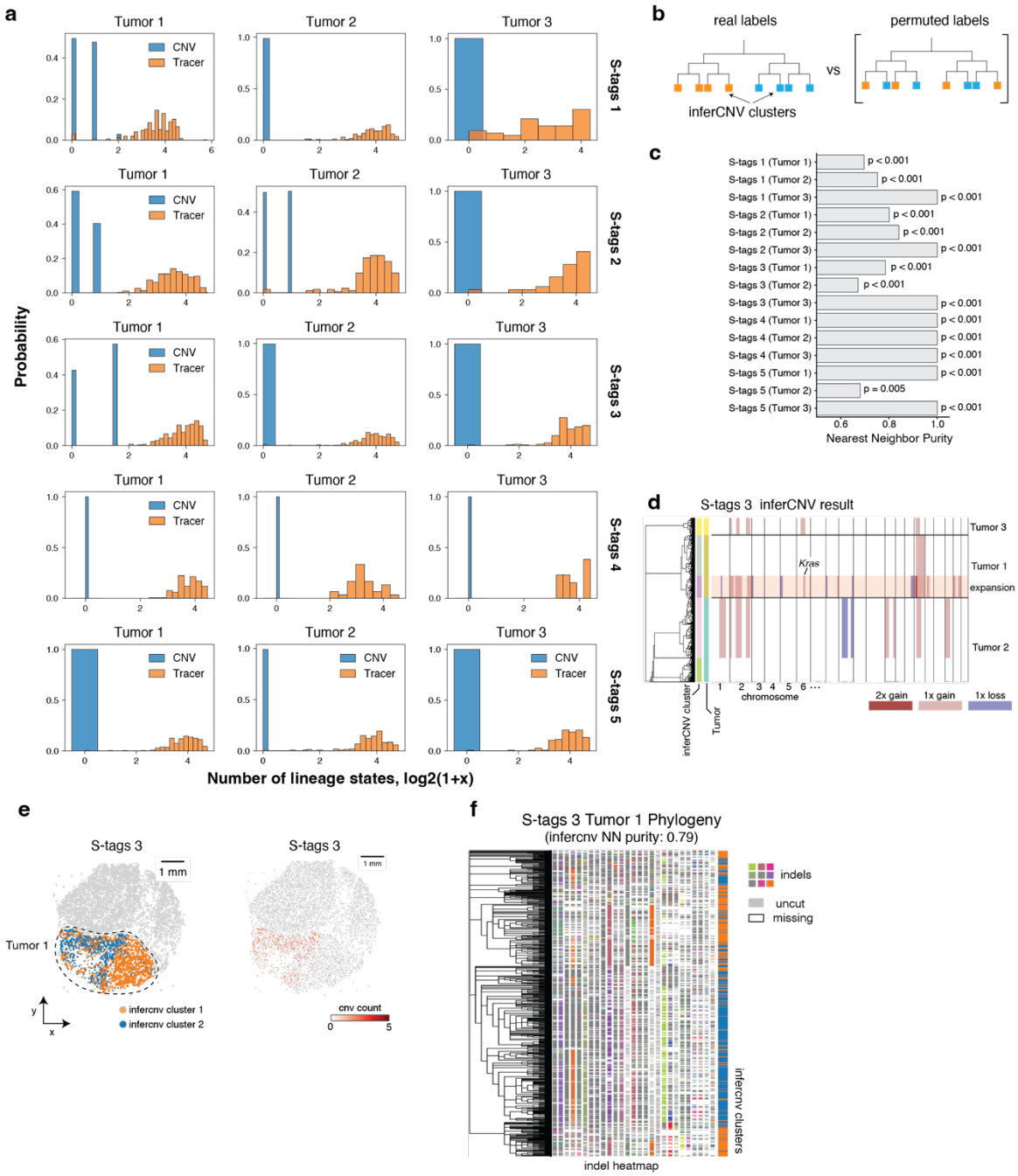

Extended Data Figure 3. Characterization of copy-number variation in Slide-tags data.

(a) Distribution of inferred CNV counts vs lineage-tracing states for each tumour in Slide-tags arrays. Tracer data consistently contains greater numbers of editable states; some tumours carry no inferred CNVs.

(b-c) CNVs corroborate phylogenetic structure inferred from tracer data. (b) Schematic of nearest-neighbour test. Neighbours of each leaf in a phylogeny are tested for consistency in inferCNV cluster, and compared to a permutation null distribution. (c) Average nearest neighbour purity for each tumour, with empirical p-values computed against 1000 random permutations

(d-f) inferCNV results for an example tumour. (d) inferCNV heatmap for a given Slide-tags dataset, S-tags 3. (e) CNV clusters and number of inferred CNVs per cell projected onto Tumour 1 in S-tags 3. (f) Tumour 1 phylogeny from S-tags 3, heatmap, and inferCNV cluster annotations.

Jones*, Sun* et al. **Extended Data Figure 4**

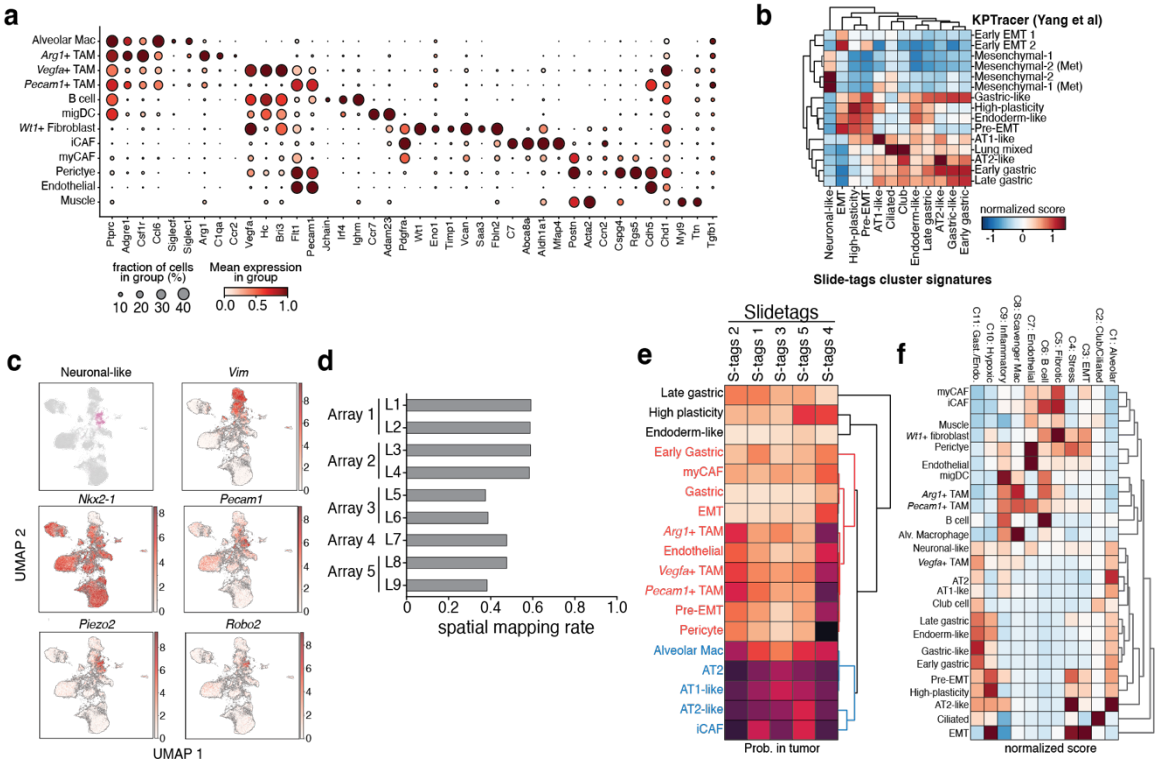

Extended Data Figure 4. Analysis of Slide-tags data and cell-type annotation.

(a) Summary of gene markers for each stromal cell population identified in Slide-tags. Each row corresponds to a stromal or immune cell-type cluster and each column corresponds to a marker gene. Dot size indicates the proportion of cells expression that gene, and colour indicates the average gene expression value (unit scaled between 0 and 1).

(b) Clustered heatmap of transcriptional score of marker genes identified from Slide-tags data of tumour and epithelial cell types applied to previous KP-Tracer data. Scores are Z-normalised.

(c) Annotation of Slide-tags tumour and epithelial UMAP projection with the Neuronal-like cell-type, and log-normalised gene expression patterns of selected genes: *Vim*, *Nkx2-1, Pecam1, Piezo2,* and *Robo2.*

(d) Proportion of cells that are confidently mapped in each Slide-tags array.

(e) Proportion of cells for each cell type that are found within the tumour boundary across Slide-tags arrays.

(f) Clustered heatmap of transcriptional scores for each spatial community, identified from Hotspot analysis of Slide-seq data, for each Slide-tags cell type cluster. Scores are Z-normalised.

Jones*, Sun* et al. **Extended Data Figure 5**

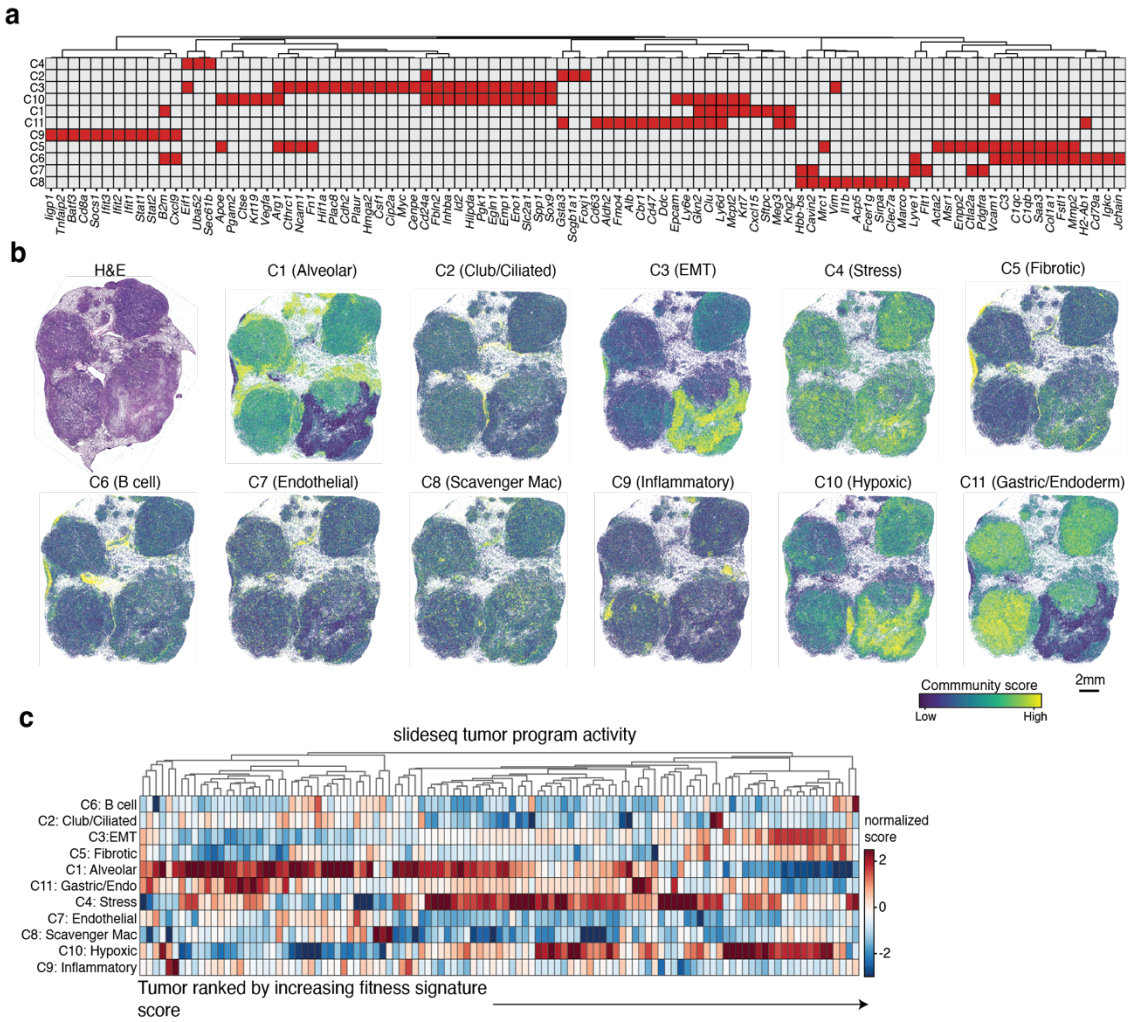

Extended Data Figure 5. Analysis of spatial communities identified from Slide-seq data.

(a) Clustered heatmap showing selected genes for each spatial community. Red colours indicate that a gene is found within that module.

(b) Community scores for each spatial community and paired H&E for a representative Slide-seq community.

(c) Clustered heatmap of community scores for each tumour in the Slide-seq dataset ordered by increasing fitness signature scores. Scores are Z-normalised.

Jones*, Sun* *et al.* **Extended Data Figure 6**

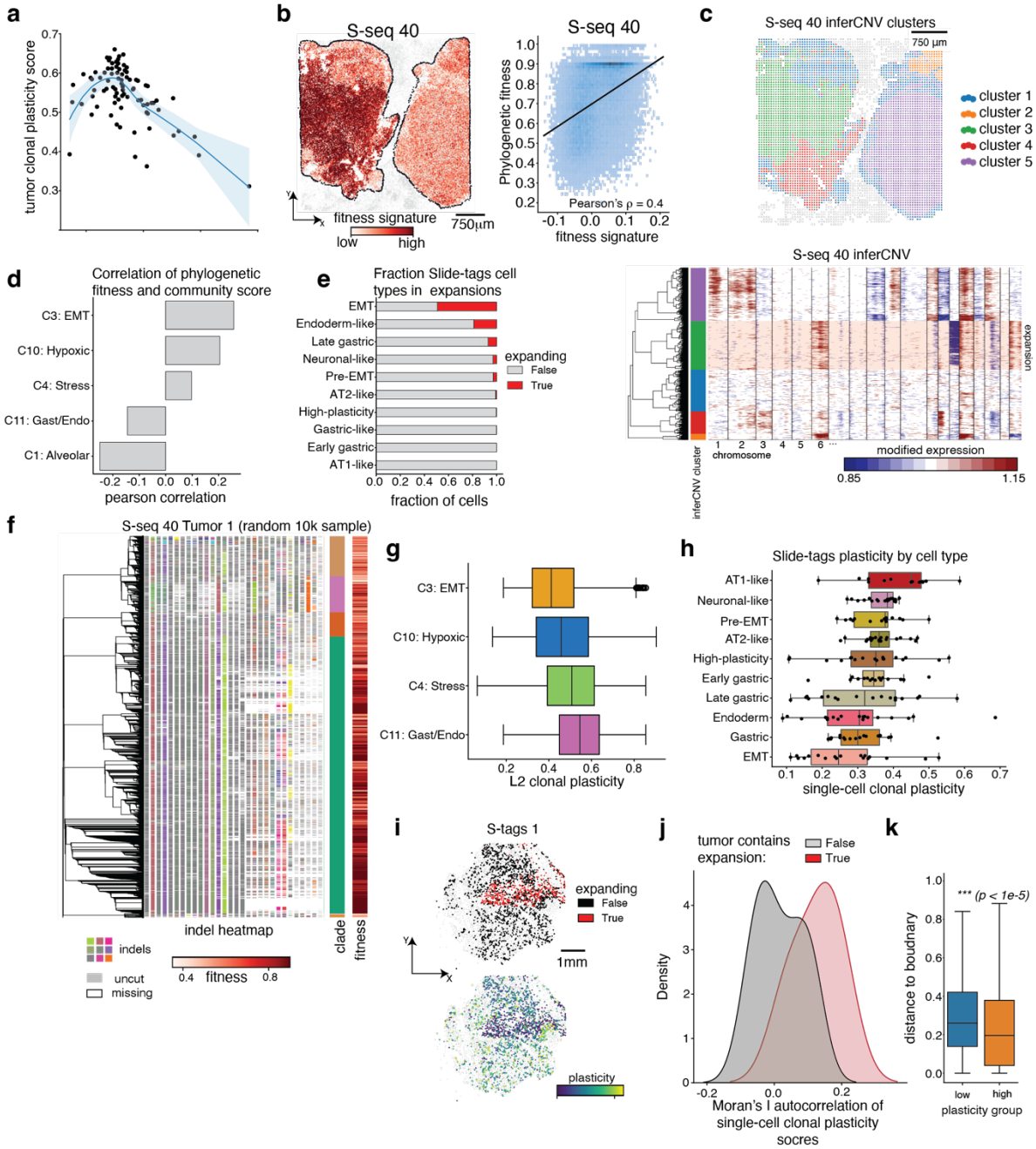

Extended Data Figure 6. Characterization of subclonal tumour and microenvironmental dynamics.

(a) Joint distribution of mean tumour clonal plasticity and fitness signatures across Slide-seq datasets.

(b) Relationship between phylogenetic fitness, estimated from inferred trees, and transcriptional fitness signature score (Pearson's correlation = 0.4)

(c) Analysis of CNVs in example Slide-seq data, S-seq 40, shows a co-localization of a CNV clone with the hypoxic region of Tumour 1 shown in Figure 3a. The expanding CNV clone includes an amplification of a region on chr6 carrying *Kras*.

(d) Correlation of phylogenetic fitness, estimated from inferred trees, and community scores for cancer-associated communities (C1: Alveolar; C3: EMT; C4: Stress; C10: Hypoxic; and C11: Gastric/Endoderm). Correlations are ordered in decreasing order.

(e) Fraction of cells found in expanding regions of Slide-tags phylogenies, summarized for each cancer cell-type.

(f) Reconstructed phylogeny and lineage tracing heatmap of representative tumour presented in **Fig. 3a-b**. Unique colours of the heatmap indicate unique insertions or deletions ("indels"), white indicates missing data, and gray colours indicates no indel detected. Colour bars indicate the subclonal clade and fitness, identical to those reported in **Fig. 3a-b**.

(g) Distribution of L2 clonal plasticity (**Methods**) quantified in Slide-seq phylogenies summarized across spots annotated by cancer-dominated communities.

(h) Distribution of single-cell clonal plasticity scores computed in Slide-tags phylogenies, stratified by cancer cell-types, and reported across tumour-array combinations. Boxplots show the quartiles of the distribution, and whiskers extend to 1.5x the interquartile range.

(i) Representative spatial localization of phylogenetic expansion (top) and single-cell clonal plasticity scores (bottom) in a single Slide-tags array (S-tags 3). Scale bar indicates 1mm.

(j) Distribution of autocorrelation values, computed by Moran's I, of single-cell clonal plasticity scores for tumours with or without expansions. Higher autocorrelation values indicate that values have higher spatial coherence. Autocorrelations are reported across all Slide-tags datasets.

(k) Distance to nearest non-tumour cell (i.e., tumour boundary) for high- and low-plasticity cells across all Slide-tags arrays. Cells with high-plasticity are closer to the tumour boundary ($p < 1e\text{-}5$, wilcoxon rank-sums test).

Jones*, Sun* *et al.* **Extended Data Figure 7**

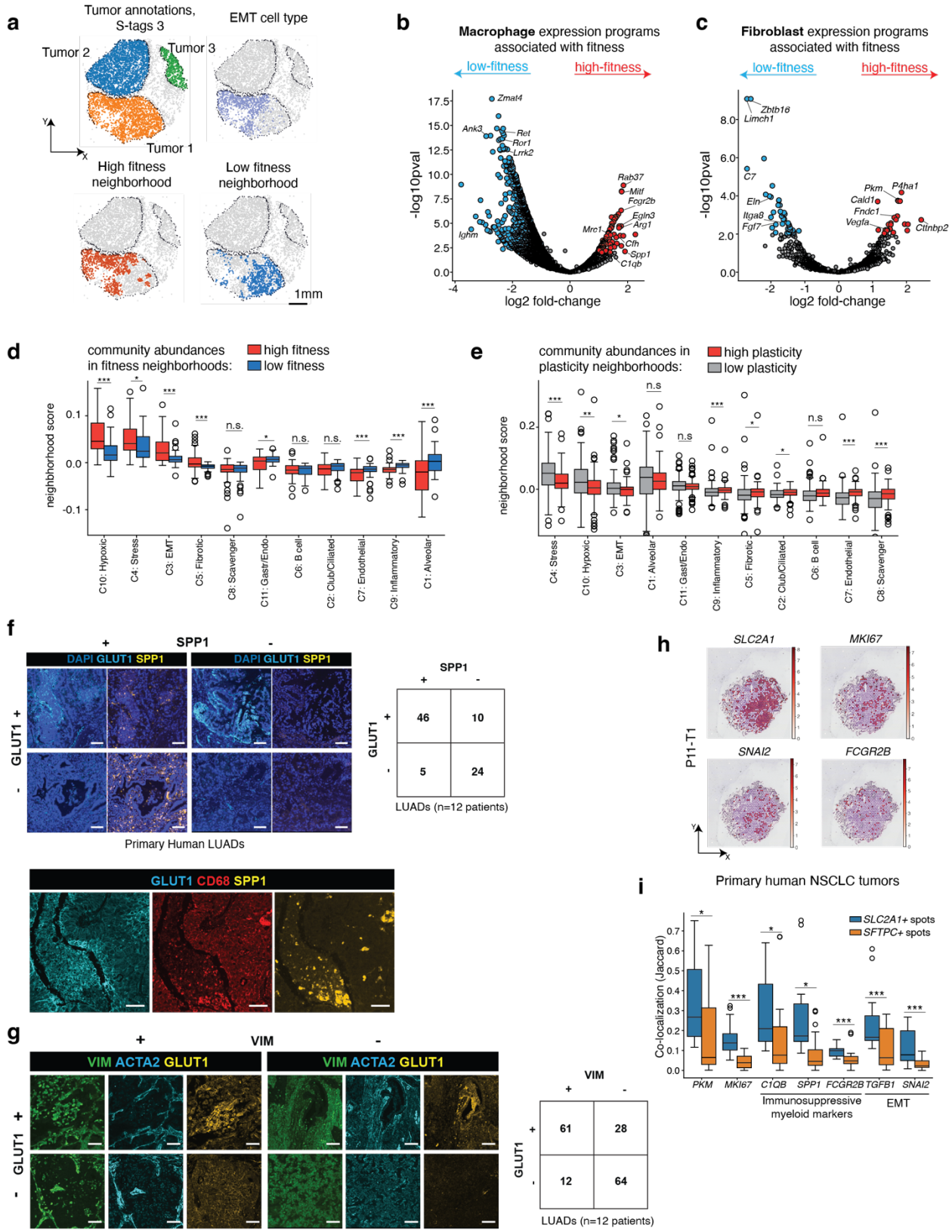

Extended Data Figure 7. Analysis of cell-type-specific changes in the expanding tumor niche.

(a) Representative example demonstrating the stratification of neighbourhoods of high- and low-fitness cells in Slide-tags data, and comparison to spatial localization of the EMT state. Scale bar indicates 1mm.

(b) Differential expression analysis of macrophage polarisation states in neighbourhoods of high- and low-fitness cells from Slide-tags arrays. Each dot is a gene, and significant hits (log2|FC| >= 1 and false-discovery-rate adjusted p-value < 0.05) are reported in red and blue. Red genes are up-regulated in neighbourhoods of high-fitness cells, and blue genes are down-regulated. Significant GO terms are reported in **Supplementary Table 3**.

(c) Differential expression analysis of fibroblast polarisation states in neighbourhoods of high- and low-fitness cells from Slide-tags arrays, as in **(b)**.

(d) Distribution of average community scores in 30μm neighbourhoods of high- or low-fitness spots in Slide-seq data. Each observation corresponds to a tumour. Significance is indicated above each comparison (*n.s.* = not significant; * = *p<0.1*; ** = *p<0.05;* *** = *p < 0.01*). Boxplots show the quartiles of the distribution, and whiskers extend to 1.5x the interquantile range.

(e) Distribution of average community scores in 30μm neighbourhoods of high- or low-plasticity spots in Slide-seq data. Each observation corresponds to a tumour. Significance is indicated above each comparison (*n.s.* = not significant; * = *p<0.1*; ** = *p<0.05;* *** = *p < 0.01*). Boxplots show the quartiles of the distribution, and whiskers extend to 1.5x the interquantile range.

(f) Immunofluorescence analysis of large lung adenocarcinoma surgical resections stained for SPP1, GLUT1, and CD68. Top: Representative images are shown (left) for a systematic quantification of co-localization between SPP1+ and GLUT1+ regions (right). GLUT1 & SPP1 are significantly co-localized (p<1e-5, Fisher's Exact Test). Bottom: a representative image of CD68, GLUT1, and SPP1 co-localization. Scale bars are 100um.

(g) Immunofluorescence analysis of large lung adenocarcinoma surgical resections stained for VIM, ACTA2, and GLUT. Representative images are shown (left) for a systematic quantification of co-localization between VIM+, ACTA2+, and GLUT1+ regions (right). VIM & GLUT1 are significantly co-localized (p<1e-5, Fisher's Exact Test). Scale bars are 100um.

(h) Representative example of spatial log-normalized gene expression values for selected genes in a human non-small-cell lung cancers (NSCLC) spatial transcriptomics dataset (see **Methods**).

(i) Overall distribution of log-normalized gene expression values of selected genes co-expressed in hypoxic (*SLC2A1*+) or epithelial-like (SFTPC+) tumor spots across all NSCLC samples in dataset shown in (h). Ontologies are indicated underneath genes. Hypoxia+ spots (*SLC2A1*+) have higher expression of proliferation (*MKI67*), immunosuppressive myeloid (*FCGR2B*, *SPP1*, *C1QB*) and EMT (*SNAI2* and *TGFB1*) markers. Statistical significance between gene expression distributions is shown for each comparison (n.s. = not significant; * = $p<0.1$; ** = $p<0.05$; *** = $p < 0.01$; wilcoxon rank-sums test). Boxplots show the quartiles of the distribution, and whiskers extend to 1.5x the interquantile range.

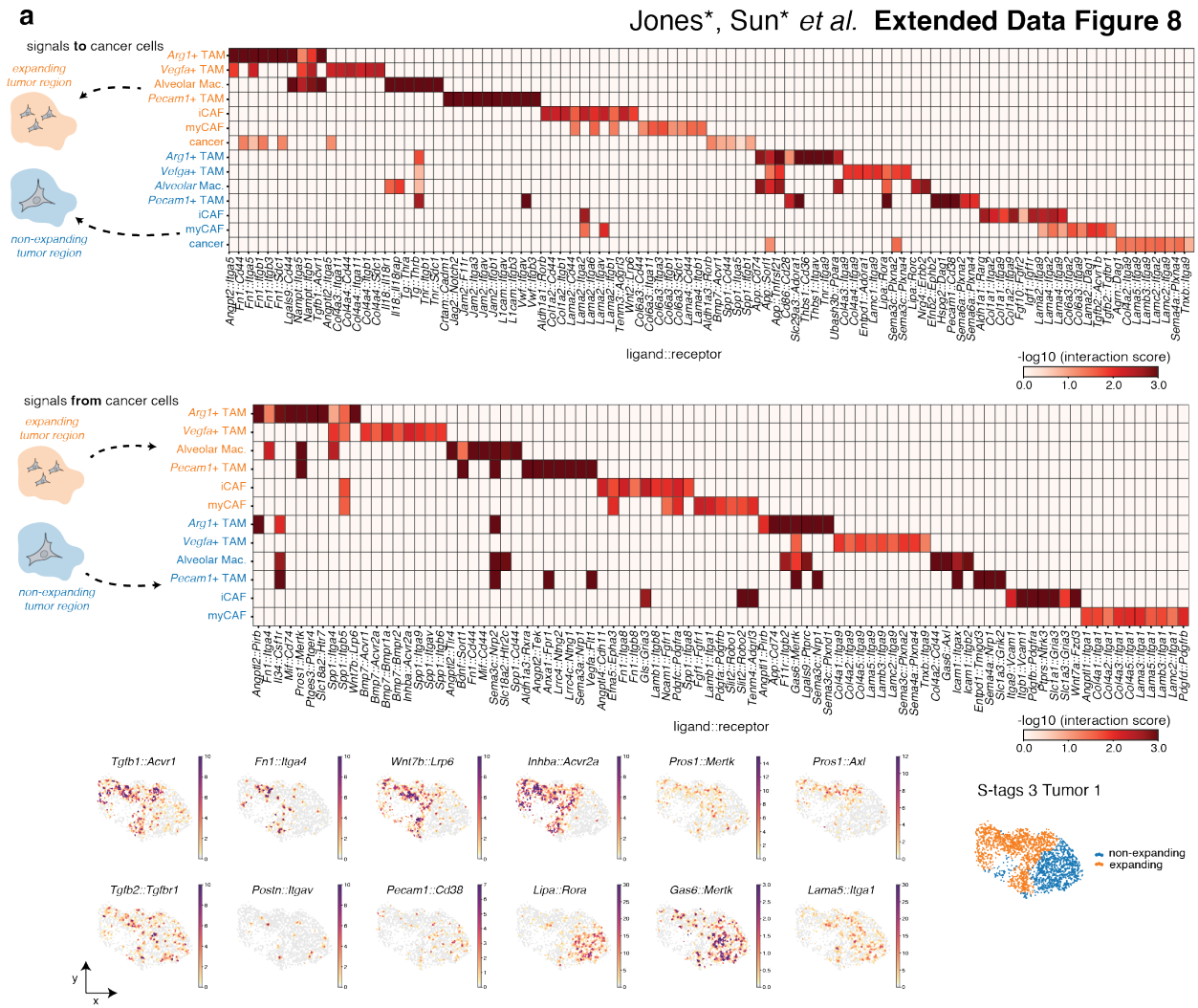
a
Jones*, Sun* et al. Extended Data Figure 8
signals to cancer cells
expanding tumor region
non-expanding tumor region
Arg1+ TAM
Vegfa+ TAM
Alveolar Mac.
Pecam1+ TAM
iCAF
myCAF
cancer
ligand::receptor
-log10 (interaction score)
signals from cancer cells
Tgfb1::Acvr1
Fn1::Itga4
Wnt7b::Lrp6
Inhba::Acvr2a
Pros1::Mertk
Pros1::Axl
Tgfb2::Tgfbr1
Postn::Itgav
Pecam1::Cd38
Lipa::Rora
Gas6::Mertk
Lama5::Itga1
S-tags 3 Tumor 1
non-expanding
expanding

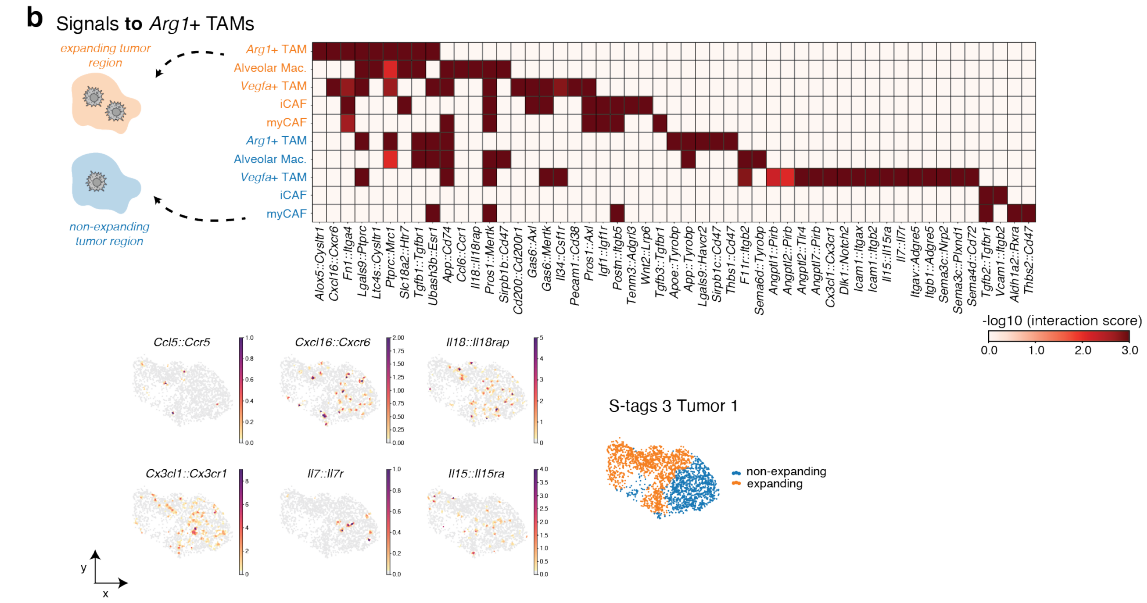
b
Signals to Arg1+ TAMs
expanding tumor region
non-expanding tumor region
Arg1+ TAM
Alveolar Mac.
Vegfa+ TAM
iCAF
myCAF
-log10 (interaction score)
Ccl5::Ccr5
Cxcl16::Cxcr6
Il18::Il18rap
Cx3cl1::Cx3cr1
Il7::Il7r
Il15::Il15ra
S-tags 3 Tumor 1
non-expanding
expanding

Extended Data Figure 8. Spatially-aware, cell-type-specific ligand-receptor analysis in expanding niches.

(a) Top ligand-receptor pairs are reported for cancer cells. Heatmaps indicate the average negative log10(interaction score) across 5 Slide-tags datasets, as computed with LARIS (see **Methods**). Representative spatial scatter plots are presented for specific ligand-receptor examples on S-tags 3 Tumour 1.

(b) Top ligands for *Arg1*+ TAMs in the expanding and non-expanding niches; heatmap and scatter plots are as above in **(a)**.

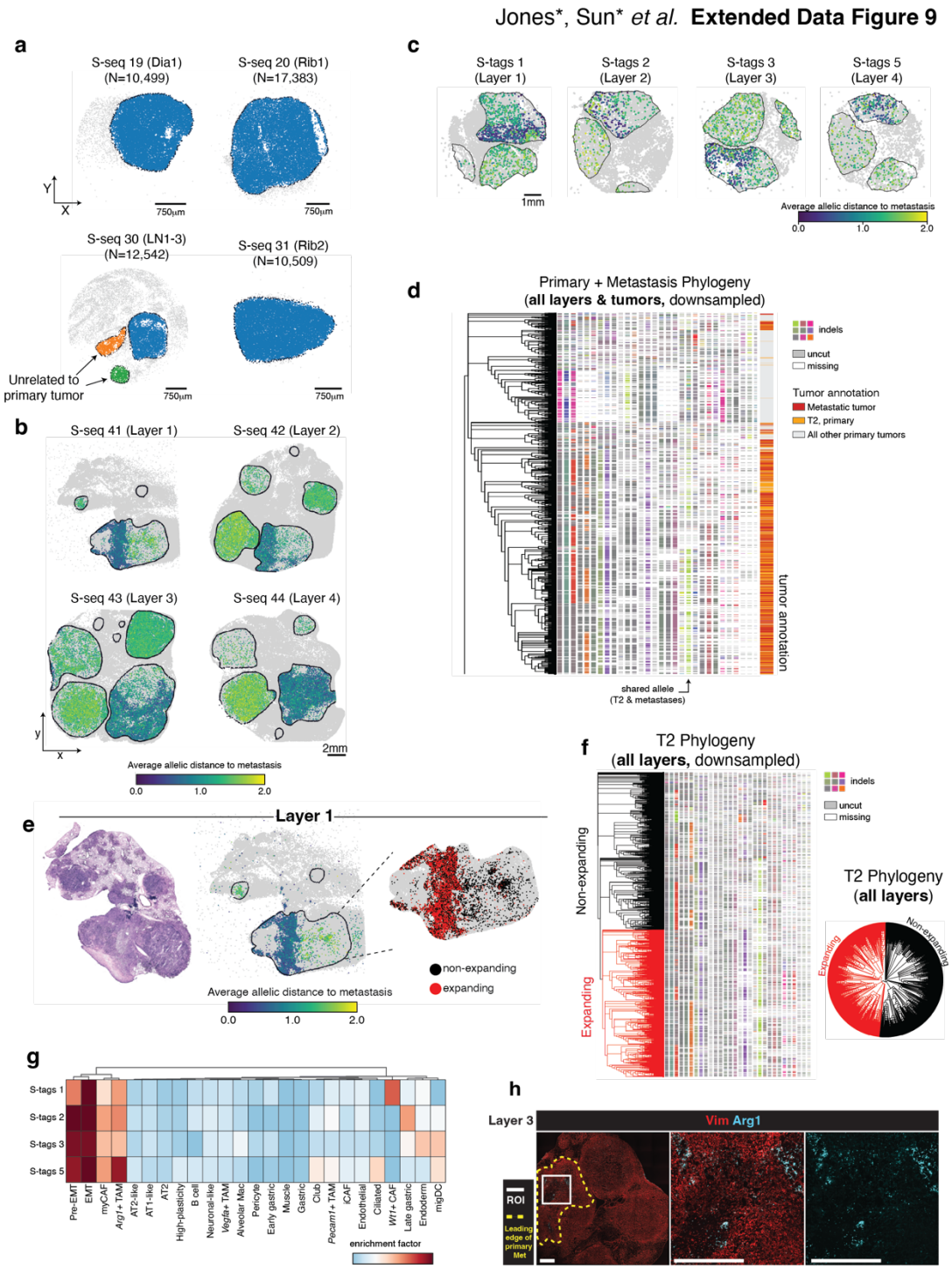

Extended Data Figure 9. Profiling of step-wise transcriptional changes in the primary tumour during metastatic initiation.

(a) Summary of metastases identified in Slide-seq spatial transcriptomics dataset. Each sample is annotated the metastatic site (LN: lymph node; Dia: Diaphragm). Two

metastases in the lymph node (S-seq 30) were not found to be related to the primary tumour studies in **Fig. 4** and thus removed from comparative analysis.

(b) Spatial projection of allelic distances for each spot with lineage-tracing data to consensus metastatic parental allele across all four layers profiled in Slide-seq. Allelic distances are normalised between 0 and 2.

(c) Spatial projection of allelic distances for each cell with lineage-tracing data to consensus metastatic parental allele across paired Slide-tags arrays. Allelic distances are normalised between 0 and 2.

(d) Phylogeny and lineage tracing heatmap of lineage-tracing data from all tumours and metastases in analysis presented in Figure 4. To improve readability, each group is down sampled to at most 600 cells per group. Cells are annotated by group: metastatic tumours, T2 (primary tumour giving rise to metastases) or all other primary tumours in Slide-seq data.

(e) H&E staining, spatial mapping of allelic distances to consensus metastatic parental allele state, and spatial localization of phylogenetic expansion for T2 in representative dataset. Allelic distances are normalised between 0 and 2.

(f) Reconstructed phylogeny and lineage tracing heatmap of T2 from all layers. Unique colours of the heatmap indicate unique insertions or deletions (“indels”), white indicates missing data, and gray colours indicates no indel detected. Full circular phylogram is shown on the right. Clades participating in expansion shown in **(e)** are shown in red.

(g) Clustered heatmap of enrichments of cell type abundances in spatial neighbourhoods of cells related to metastases in Slide-tags arrays.

(h) Immunofluorescence imaging of ARG1 and VIM in a section of the tumour-bearing lung close to Layer 3. Leading edge of the metastasis-initiating subclone is indicated with yellow dashed line. Scale bar indicates 1mm.

Jones*, Sun* *et al.* **Extended Data Figure 10**

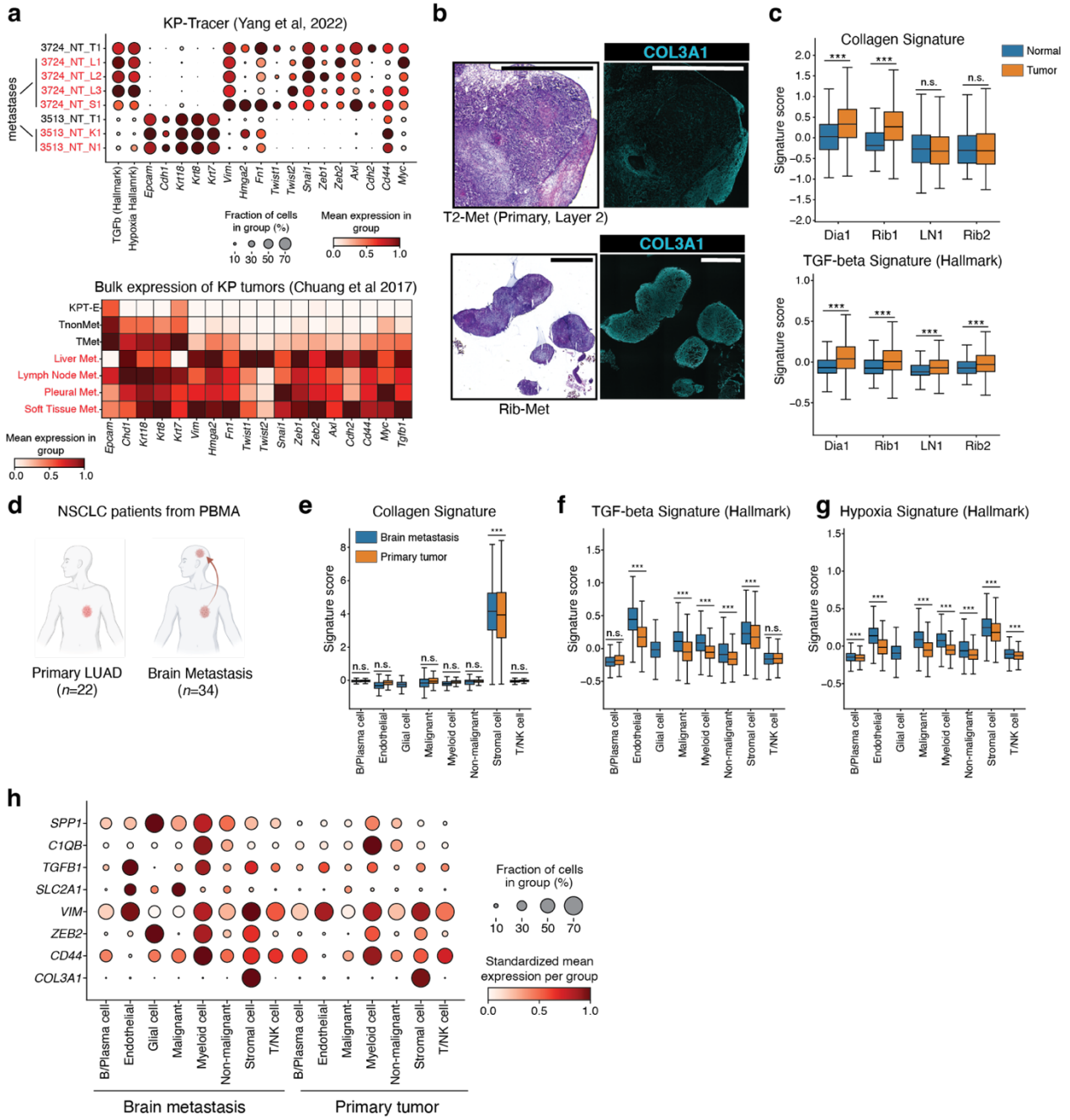

Extended Data Figure 10. Analysis of microenvironmental changes associated with metastatic colonization.

(a) Comparative analysis of metastasis-related gene expression between primary and metastatic tumours from KP tumours from the KP-Tracer study (top, *n*=6 metastases from 2 mice) and Chuang et al (bottom, *n*=24 metastases from 12 mice). Gene dots are sized by fraction of cell expressing a gene and values are standardized across genes (top).

Metastases are indicated in red text. T: primary tumour, L: liver metastasis, S: soft tissue metastases, K: kidney metastasis, N: lymph-node metastasis; KPT-E: early stage KPT tumours; Tnonmet: primary tumors that do not seed metastases; Tmet: primary tumours that do seed metastases.

(b) H&E and immunofluorescence imaging of COL3A1 in a section of the metastasis-initiating primary tumour (Layer 2) and related metastasis. Scale bar indicates 2.5mm.

(c) Expression of collagen deposition and *TGFβ* signalling pathways in Slide-seq data, segmented by tumour region. Significant increases in tumour region are indicated (***: $p<0.01$; n.s.: not significant).

(d) Analysis of 56 human lung adenocarcinoma tumours from the PBMA cohort, including 34 brain metastases and 22 primary LUAD tumours from the PBMA LUAD cohort.

(e-g) Cell-type specific transcriptional signatures of collagen deposition, *TGFβ* signalling, and hypoxia across compartments (brain metastasis or primary tumour). Significant increases in brain metastases are indicated (***: $p<1e-3$; n.s.: not significant).

(h) Expression of specific marker genes across cell types and compartments. Dots are sized by fraction of cells expressing the gene, and expression values are standardized across genes.